Microstructure and Fracture Mechanics Properties of 13% Cr-4% Ni Martensitic Stainless Steels

by

Fayaz FOROOZMEHR

ARTICLE-BASED THESIS PRESENTED TO ÉCOLE DE TECHNOLOGIE
SUPÉRIEURE IN PARTIAL FULFILLMENT OF THE REQUIREMENTS
FOR THE DEGREE OF PHILOSOPHY
PH.D.

MONTREAL, JULY 12, 2021

ÉCOLE DE TECHNOLOGIE SUPÉRIEURE
UNIVERSITÉ DU QUÉBEC

BOARD OF EXAMINERS

THIS THESIS HAS BEEN EVALUATED

BY THE FOLLOWING BOARD OF EXAMINERS

Mr. Philippe Bocher, Thesis Supervisor
Mechanical Engineering Department at École de technologie supérieure

Mrs. Ruxandra Botez, President of the Board of Examiners
Systems Engineering Department at École de technologie supérieure

Mr. Ricardo Zednik, Member of the jury
Mechanical Engineering Department at École de technologie supérieure

Mr. Jean-Michel Bergheau, External Evaluator
Université de Lyon, École National d'Ingénieurs de Saint-Étienne (ENISE), France

THIS THESIS WAS PRENSENTED AND DEFENDED

IN THE PRESENCE OF A BOARD OF EXAMINERS AND PUBLIC

IN JUNE 30 2021

AT ÉCOLE DE TECHNOLOGIE SUPÉRIEURE

FOREWORD

A mes parents Mohammad et Farzaneh.

ACKNOWLEDGMENT

Au début, je dois déclarer que je suis très fier d'avoir l'honneur d'être étudiant de Professeur Philippe Bocher et de profiter ces connaissances et pratiques scientifiques. Donc, en premier lieu, je tiens à remercier tout particulièrement Professeur Philippe Bocher qui m'a ouvert une nouvelle fenêtre sur le monde de la science en me donnant la chance de travailler et évoluer mes capacités scientifiques et pratiques au sien de son groupe de recherche. Sans ses conseils et rigueurs scientifiques durant la révision critique de mes documents, je n'aurais jamais l'occasion de publier de bons articles scientifiques dans des journaux scientifiques réputés. J'avoue que je lui dois mon doctorat, et que je suis très fier d'avoir son nom à côté du mien dans ma thèse ainsi que dans les articles scientifiques que nous avions publiés ensemble.

Je tiens à remercier les membres de jury pour le temps qu'ils ont consacré à lire et à évaluer cette thèse.

J'exprime ma plus profonde reconnaissance envers ma famille pour leur soutien inconditionnel pendant mes études doctorales.

Microstructure et propriétés de mécanique de rupture des aciers inoxydables martensitiques 13% Cr-4% Ni

Fayaz FOROOZMEHR

RÉSUMÉ

Les aciers inoxydables martensitiques 13% Cr-4% Ni sont utilisés pour la fabrication des roues hydroélectriques dû à leurs haute résistance et ténacité, ainsi que leurs bonnes résistances contre corrosion et érosion par cavitation. Puisque les roues des turbines hydrauliques sont sujet à des contraintes cycliques, la fissuration par fatigue est la source principale d'endommagement durant leur vie utile, et donc des inspections régulières sont réalisées en vue de vérifier la gravité des dommages et conduire des réparations requises.

Le but principal de cette étude est de caractériser les comportements à rupture des matériaux des roues hydroélectriques i.e. les versions coulée (CA6NM), corroyée (415), et métaux d'apport (410NiMo). La possibilité d'établir les relations entre comportement à rupture, caractéristiques inclusionnaires et teneurs en austénite a motivé l'étude. Les taux de triaxialité des contraintes S_T ont été mesurés dans la région de striction à partir des échantillons cassés suite à des essais de traction, et la micromécanique de rupture a été caractérisée en utilisant le modèle modifié de Rice et Tracey qui décrit la rupture ductile en termes de relation entre la croissance d'une vide et S_T. La Mécanique Linéaire-Élastique de la Rupture (MLER) n'est pas applicable pour les petits échantillons des matériaux ductiles, tels que les aciers inoxydables martensitiques 13% Cr-4% Ni, parce qu'une plastification généralisée survient lors de l'essai K_{Ic}. L'approche de Mécanique Élasto-Plastique de la Rupture (MEPR) est donc nécessaire pour mesurer le taux de libération de l'énergie de déformation (J) de cette catégorie des aciers inoxydables. Le comportement de la propagation stable de la fissure dans le substrat (CA6NM), les matériaux d'apport, et la Zone Affectée Thermiquement (ZAT) a été caractérisé lors de l'essai J_{Ic}. Le substrat a été examiné à l'état traité thermiquement, alors que le matériau d'apport et la ZAT ont été examinés dans les deux conditions de brut de soudage et de traité thermiquement. Les faciès de ruptures ont été examinés à l'aide d'un microscope électronique à balayage (MEB) couplé à un spectromètre à rayons X à dispersion d'énergie.

Il a été montré que la déformation subie après la striction peut être estimée par la taille et l'espacement inclusionnaire quand la croissance des vides est importante avant la rupture finale; cependant, dans le cas où la croissance des vides est négligeable dû à un espacement inclusionnaire très petit, le modèle proposé ne convient pas. La teneur en austénite et les propriétés mécaniques de la matrice devraient également être considérées. Le traitement thermique a considérablement amélioré la ténacité J_{Ic} de la soudure et la ZAT par des facteurs de 2 et 2.7, respectivement. Cependant, des propagations instables ont été surviennent dans la soudure lors de tous les essais J_{Ic} effectués dans la ZAT. Ceci est dû à l'effet néfaste de très petit espacement inclusionnaire qui résulte en une coalescence immédiate des micro-vides.

Mots-clés : ténacité J_{Ic}, propagation stable de la fissure, propagation instable, inclusion

Microstructure and fracture mechanics properties of 13% Cr-4% Ni martensitic stainless steels

Fayaz FOROOZMEHR

ABSTRACT

13% Cr-4% Ni martensitic stainless steels are used to manufacture the hydroelectric runners due to their high strength and toughness, as well as their good resistance against corrosion and cavitation erosion. As hydraulic turbine runners are subjected to cyclic loadings, fatigue cracking is the main source of damage during their useful lifetime, and regular inspections are performed to verify the severity of the damage, and carrying out the required reparations.

The main purpose of this study is characterizing the fracture behaviors of the hydroelectric runner component materials i.e. the cast (CA6NM), the wrought (415), the matching weld metals (410NiMo). The possibility of establishing relationships among fracture behavior, inclusion characteristics and austenite contents has motivated the study. The stress triaxiality S_T ratios were measured on the necked region from the tension broken samples, and fracture micromechanics were characterized using the modified Rice and Tracey model describing ductile rupture in terms of void growth-S_T ratio relationship. Linear-Elastic Fracture Mechanics (LEFM) is not applicable for small laboratory specimens of ductile materials, such as 13% Cr-4% Ni martensitic stainless steels, as large-scale yielding occurs during K_{Ic} testing. Elastic-Plastic Fracture Mechanics (EPFM) approach is therefore necessary to measure the strain energy release rate (J) for this category of stainless steels. The stable crack growth behavior of the substrate steel (CA6NM), the weld metals, and the Heat-Affected Zone (HAZ) was characterized during J_{Ic}-testing. The substrate steel was tested in heat-treated condition, whereas the weld metal and the HAZ were examined in both as-welded and heat-treated conditions. Fracture surfaces were examined using a Scanning Electron Microscope (SEM) coupled with an Energy Dispersive X-ray (EDX) spectrometer to reveal the nature of the second phase particles.

It was shown that fracture strain after necking can be estimated using size and spacing of inclusions when considerable void growth occurs before final rupture; however, in the cases in which negligible void growth occurs due to a very small inclusion spacing, the proposed model is not appropriate. The austenite content and the mechanical properties of the matrix should also be considered. The heat-treatment significantly improved the fracture toughness J_{Ic} of the weld metal and the HAZ by factors of 2 and 2.7, respectively. However, unstable propagations were occurred into the weld metal in the case of all the J_{Ic} tests performed on the HAZ. This is due to the detrimental effect of the very small inclusion spacing in the microstructure of the weld metal, resulting in an immediate coalescence of the nucleated micro-voids.

Keywords: fracture toughness J_{Ic}, stable crack growth, unstable propagation; inclusion

TABLE OF CONTENTS

Page

LIST OF TABLES

LIST OF FIGURES

LIST OF ABREVIATIONS

AWS	American Welding Society
CT	Compact Tension specimen
EDX	Energy Dispersive X-ray
EPFM	Elastic-Plastic Fracture Mechanics
FCAW	Flux-Cored Arc Welding process
HAZ	Heat-Affected Zone
LEFM	Linear-Elastic Fracture Mechanics
LPD	Load-Point Displacement
LWSS	Locally Weighted Scatterplot Smoothing
MVC	Micro-Void Coalescence
RD	Rolling Direction
SEM	Scanning Electron Microscopy
TD	Transverse Direction
TRIP	Transformation-Induced Plasticity
XRD	X-Ray Diffraction

LIST OF SYMBOLS

a	crack length
a_0	initial crack length
A_{pl}	crack propagation area under force-displacement curve
b_0	initial ligament ($W-a_0$)
B	whole thickness of the CT sample
B_N	net thickness (distance between the roots of the side grooves)
D	inclusion diameter
e	engineering strain
E	Young's modulus
e_f	elongation at fracture
e_u	uniform elongation at necking
f	a function of the sample geometry (a and W)
F	load
$H(D)$	harmonic mean value of inclusion diameters
J	J-integral value for a given crack growth
J-R curve	J-Resistance curve
J_{el}	elastic component of J
J_{Ic}	initiation J value under plane strain condition
J_{pl}	plastic component of J
J_Q	fracture toughness J_{Ic} candidate value
K	stress intensity factor
K_{Ic}	plane strain stress intensity factor
n	strain hardening coefficient
N_A	surface density of inclusions
n_i	instantaneous strain hardening coefficient
P	engineering stress
R	void radius
$\mathbb{R}$	radius of curvature of necking at the moment of final rupture
r_0	radius of the necked region at the moment of final rupture

R_0	average value of initial inclusion radius
R_{0L}	average value of the inclusions larger than the $R_{0median}$
$R_{0median}$	median radius of inclusions
R_{0S}	average value of the inclusions smaller or equal to the $R_{0median}$
R_0'	inclusion radius measured after rupture (on fracture surfaces)
R_i	initial void radius
R_f	final void radius
S	inclusion spacing
S_T	stress Triaxiality ratio
T	tearing modulus
V_v	volume fraction of inclusions
W	sample width
Δa	crack extension
Δa_p	physical crack extension
ΔK	stress intensity factor amplitude
γ_0	austenite content
ε	true strain
ε_{bn}	true strain before necking
ε_n	fracture strain after necking
ε_n'	calculated fracture strain after necking
ε_p	equivalent plastic strain
ε_r	true fracture strain
ε_{vs}	deformation resulting from void sheeting
ν	Poisson ratio
σ	true stress
σ_{eq}	von Mises equivalent stress
σ_m	mean stress
0.2% σ_y	0.2% offset yield strength
σ_y	yield strength
σ_{UTS}	tensile strength

INTRODUCTION

In the late fifties, the disadvantages of chromium martensitic stainless steels such as low weldability and susceptibility to cold cracking, as well as low toughness, led to the fabrication of a new generation of these alloys. The carbon content was decreased to obtain a soft martensitic microstructure having a much higher weldability, and some percentages of nickel were added to decrease the amounts of delta ferrite, increasing toughness. These grades of martensitic stainless steels are called "supermartensitic stainless steels" due to their high mechanical properties [1]. The carbon content of these grades does not exceed 0.05 wt% [2].

Among different grades of these alloys, 13% Cr-4% Ni steel is used to fabricate hydraulic turbine runners because of its good corrosion resistance, good resistance to cavitation erosion, excellent weldability, and good castability [3-5]. Both processes of assembling and repairing of the turbine runners are usually made by Flux-Cored Arc Welding (FCAW) process [6]. This is a high-quality welding process; however, the existence of defects such as inclusions and very small cracks in a welded structure is inevitable. A hydroelectric runner is subjected to cyclic loadings, then propagation during service is highly probable.

In the traditional design of a hydroelectric runner, no crack is considered to be found in the microstructure, and material selection is performed based on the material's strength, considering a safety factor [7]. However, microscopic and macroscopic defects such as inclusions, and cracks resulting from fabrication process exist in an operational component. Since these defects magnify the stress locally, inspections should be performed at small time intervals to repair the damage resulting from fatigue crack propagation before they get too big. As these inspections should be performed in large numbers, it is desirable to extend maintenance time intervals as much as possible saving high amounts of time and money.

Fracture Mechanics provides a new design approach whose the most important advantage is taking into account the crack size [7]. In this approach, the applied stress and crack size are related to a parameter called "stress intensity factor K" characterizing the stress and strain conditions at the crack tip. According to the Fracture Mechanics approach, crack propagation occurs when K reaches a critical value K_c. In the case of a thick enough component, i.e. under plane strain conditions, the K_c is considered as a material property and is called "fracture toughness K_{Ic}" [7, 8] . In fact, the most interesting aspect of this design approach is that inspections can be performed at much longer time intervals as the maximum allowable crack size can be calculated using K_{Ic} and applied stress.

Fracture toughness K_{Ic} is defined as the resistance of material against unstable crack propagation where the size of the crack tip plastic zone is small compared to sample dimensions (small-scale yielding condition). However, K_{Ic} testing of ductile materials using a small laboratory sample leads to large deformations. Then, the critical value of energy release rate J_c at the onset of stable crack propagation is measured as fracture criterion in this case. This fracture criterion is considered as a material property under plane strain conditions, called fracture toughness J_{Ic}. [7, 8].

The fracture behavior of a material is directly related to its microstructure. Therefore, the microstructure-mechanical property relationships should be investigated to help the manufacturers to modify the fabrication process in order to improve the fracture toughness, and/or using alloys with desirable microstructural features to target superior mechanical properties.

The whole turbine runner undergoes a tempering heat treatment after final assembly [9], resulting in a ductile material. It was shown that fatigue crack growth rate of the tempered weld metal is one tenth of that of the as-welded one [10]. However, after reparation process, a hydroelectric runner is usually operational directly without having undergone any heat treatment. Therefore, in the case of microstructural and mechanical characterizations, both as-welded and heat-treated conditions should be considered. For a hydroelectric runner, in addition to the base and weld metals, the Heat-Affected Zone (HAZ) should be also characterized in terms of fracture toughness properties as it is considered as a source of weakness. Exposed to various thermal cycles during welding, the HAZ present microstructural inhomogeneities in the presence of residual stresses, and the problem of cold cracking is also a matter of concern in this region [6, 11]. Accordingly, a total breakdown of the hydraulic turbine runner is most likely to take place in the HAZ undergoing unstable crack propagation.

During tempering at around 600 °C, some reversed transformation of martensite to austenite happens and "reformed austenite" is formed between martensite laths, as well as on the prior austenite grain boundaries [5, 12, 13]. In this condition, the reformed austenite is stable after cooling, even at cryogenic temperatures (until -196 °C) [12], but will transform into martensite under loading. It was found that this Transformation-Induced Plasticity (TRIP) increases the ductility and toughness of these alloys [14, 15]. Tempering at higher temperatures forms austenite that may retransform into fresh martensite during cooling. Accordingly, the content and origin of austenite should be carefully considered in the microstructural characterization of 13% Cr-4% Ni martensitic stainless steels.

Inclusion behavior during deformation should be studied in detail to characterize fracture micromechanics. Second phase particles play the major role in fracture as they act as stress raisers in the microstructure [16-20]. Higher inclusion density leads to more numerous micro-void nucleation sites with smaller spacing, resulting in a lower toughness and on the other hand, larger inclusions will facilitate the early micro-void nucleation at lower stresses and strains.

This article-based thesis includes five chapters: A review of the most recent literature on the Flux-Cored Arc Welding (FCAW) process, the microstructure of these alloys, a summary on the Linear-Elastic and Elastic-Plastic Fracture Mechanics, and a critical review on ductile rupture micromechanics are provided in the first chapter. The second chapter presents the first article characterizing fracture micromechanical processes involved during tension tests using a model-based approach. The third and fourth chapters present the second and the third articles, respectively. In the second paper, the effect of low temperature intercritical heat treatment on fracture behavior of the weld metal of this category of stainless steels was examined performing tension and fracture toughness J_{Ic} tests. The fracture toughness of the HAZ in the welded joints of these materials, addressed in the third paper, was presented in the fourth chapter. It was shown that the weakest region in the welded joints of these materials is the weld metal itself, rather than the HAZ. The fifth chapter addresses the logic behind all experimental works and the ductile fracture model used in this study, providing a discussion on all obtained results. In the end, the final part of this thesis summarizes the main achievements of this study in the “conclusions” section.

CHAPTER 1

LITERATURE REVIEW

The principal goal of this chapter is to review the most important microstructural features of 13% Cr-4% Ni martensitic stainless steels, and their effects on fracture behavior of these alloys. A review on FCAW process is provided at first, and then the microstructure of the base and weld metals, as well as that of the HAZ is studied. The basics of the Linear-Elastic and Elastic-Plastic Fracture Mechanics are reviewed and one-parameter fracture criterions were introduced in each case (K in LEFM and J in EPFM). Finally, cleavage and ductile fracture micromechanics are studied.

1.1 Manufacturing process

The manufacture of hydroelectric runners, including joining of cast/hot rolled parts, is usually made by Flux-Cored Arc Welding (FCAW) process. The process is schematically shown in Figure 1-1. The weld pool is protected from the ambient by self-shielding gases, as well as by the slag generating from the flux material. Alloying elements, deposition rate enhancers, and arc stabilizers are the other components added to the flux material to improve the quality of the weld metal and welding process. As nitrogen forms sharp needle shape Fe_4N components reducing the ductility and impact toughness by initiating cracks under loading [21], the flux material usually contains Zr, Ti, Si, and Al to reduce the nitrogen of the weld by forming nitrides. These nitrides will be removed from the weld pool, as these enter into the slag. FCAW is used for in-situ welding as flux material provides a very good protection separating the weld pool from the air [22]. However, additional shielding gases can also be used in order to have a better protection of the weld pool if necessary. This welding process has a high deposition rate, and the resulting weld metal has a smooth surface and a high quality [23, 24]. The slag removal is easy, and this welding process can be carried out automatically [24, 25].

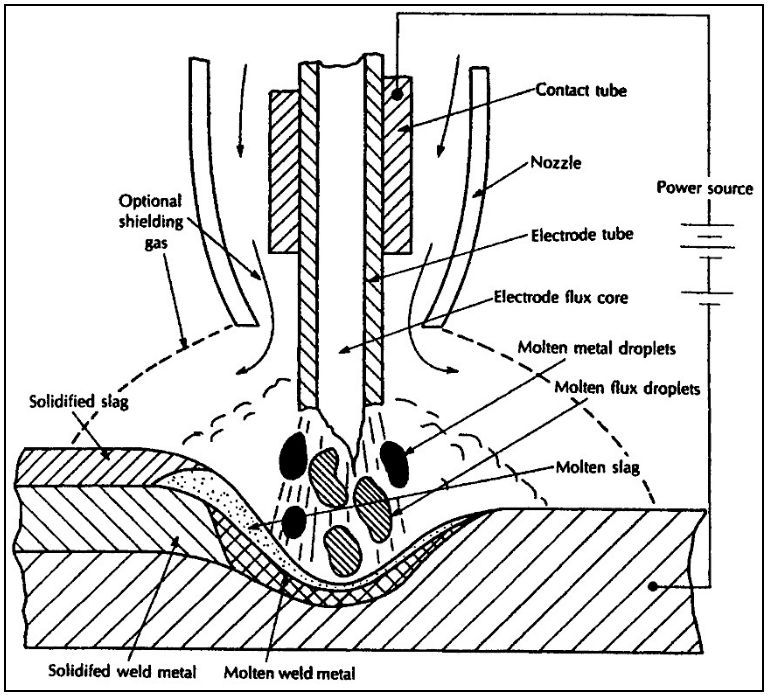

Figure 1-1 Flux-cored arc welding (FCAW) process. Even without using the optional shielding gas, the molten flux droplets separate the weld pool from ambient, producing a good protection. The use of optional shielding gas produces a very strong protection of the weld pool, resulting in a good weld metal quality. Taken from Messler Jr (1999, p.67 [26])

1.2 Microstructure of supermartensitic stainless steels

1.2.1 Base and weld metals

Figure 1-2 shows the phase diagram of supermartensitic stainless steels. A minimum amount of 10.5 wt% of chromium is necessary in order for the formation of chromium oxide protective layer, making the steel as stainless [27]. In equilibrium state, the liquid solidifies as delta ferrite, then it transforms into austenite as the temperature decreased. Except furnace cooling, these alloys transform into martensite under most cooling conditions. Because of the very low carbon content in these alloys, the as-quenched microstructure consists of soft martensite. In addition, due to the concentration of some ferrite promoting elements in the final stage of solidification, some amounts of supercooled delta ferrite will remain at the prior austenite grain boundaries. As a result of adding Ni, the amounts of the delta ferrite are highly decreased in

13% Cr-4% Ni alloys; however, some delta ferrite traces can be found in the microstructure, especially in the cast version and the weld metal. On the other hand, some amounts of austenite can be also stabilized at room temperature after the intercritical tempering between Ac_1 and Ac_3 temperatures as Ni is an austenite promoting element [2, 27].

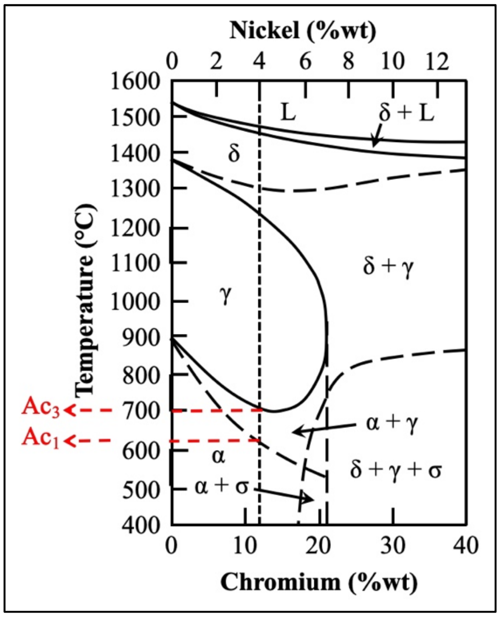

Figure 1-2 Supermartensitic stainless steels phase diagram. The gamma loop is extended to about 21 wt.% Cr; the temperature at which martensite starts to transform into austenite during heating (Ac_1) decreased to about 620 °C, and the one at which this transformation ends (Ac_3) decreased to about 700 °C due to adding 4 wt.% Ni.
Adapted from Folkhard (1988, p.10 [2])

Heat treatment is most often applied to 13% Cr-4% Ni martensitic stainless steels to increase the ductility of the as-quenched microstructure [9]. During heat treatment, the solid solution carbon atoms form carbides which mainly are of the types $M_{23}C_6$ and M_7C_6, where M majorly consists of Cr with some portions of Fe and Mo [28]. These $M_{23}C_6$ carbides precipitate on prior austenite grain boundaries, reduce the local Cr content, making the Cr_2O_3 passive film weak, and cause intergranular corrosion [29, 30]. Due to the reverse transformation of martensite into austenite during tempering, the austenite is also reformed between martensite laths, as well as on the prior austenite grain boundaries [5, 12, 13]. In the case of low tempering temperatures, the reformed austenite is stable until cryogenic temperatures, whereas austenite formed at higher tempering temperatures will retransform into fresh martensite during cooling [2, 12]. Figure 1-3 shows very fine islets of the reformed austenite located between martensite laths in a cast 13% Cr-4% Ni supermartensitic stainless steel.

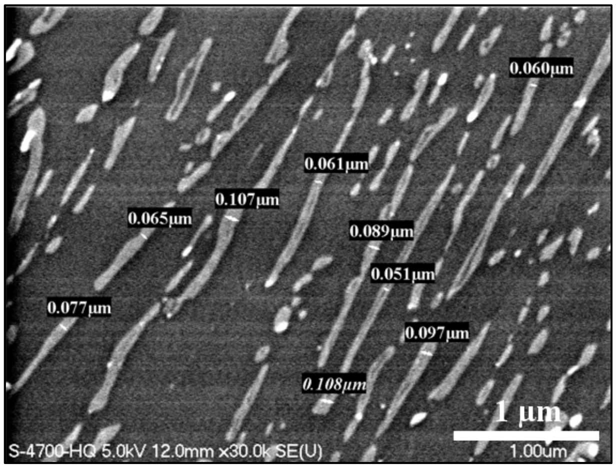

Figure 1-3 Very fine austenite formed after heat treatment in the microstructure of a cast version of 13% Cr-4% Ni supermartensitic stainless steel.
Taken from Thibault et al. (2011 [5])

1.2.2 Heat-Affected Zone (HAZ)

During welding, a part of the base metal located in the vicinity of the fusion line is subjected to very high temperatures called HAZ. Significant microstructural heterogeneities and tensile residual stresses can be produced in the HAZ [11, 31-33]. As a result, this region is considered as a source of weakness in a welded joint [34-36], specifically in terms of unstable crack growth. The microstructure of the HAZ is more complex than that of the base metal, consisting of several regions. The microstructure of each region depends on the corresponding thermal cycle applied during welding. The microstructure of the HAZ can be divided into five major regions according to the phase diagram of 13% Cr-4% Ni supermartensitic stainless steels (Figure 1-2). In the first region, the base metal is partially melted in a narrow region right next to the fusion line (L + δ region). The high temperatures associated to the second region (δ region) promote δ-ferrite grain growth. The third region is where ferrite and austenite coexist in equilibrium state (δ + γ region), and austenite partially transforms into martensite. A full austenitic microstructure is obtained in the fourth region (γ region). A partial transformation of martensite into austenite takes place in the fifth region (α + γ region) [1, 11].

1.3 Resistance against stable/unstable crack propagation in supermartensitic stainless steels

In 1920, Griffith revolutionized the concept of fracture describing crack growth as an energy balance between potential and surface energies: On one hand, the potential energy of the cracked body decreases when crack grows further. On the other hand, the surface energy increases as two new surfaces are created. According to the Griffith's theory, crack growth occurs when the net decrease of the potential energy is greater than the required additional crack surface energy [37]. Griffith's relationship was obtained for fragile materials, and only surface energy γ_s can be considered as the energy required for the crack growth. However, in the case of ductile materials, plastic deformation occurs ahead the crack during crack growth, and hence a plastic work will also take place [38]. In other words, when plastic strains are present, not only the surface energy should be considered, but also the plastic energy associated with crack growth γ_p should be added as proposed by Irwin [7]. Therefore, for an infinitely wide cracked plate exposed to remote tension loading shown in Figure 1-4:

$$\sigma_f = \sqrt{\frac{2E\left(\gamma_s + \gamma_p\right)}{\pi a}} \tag{1.1}$$

where σ_f is fracture stress, E is the Young's modulus, and a is half the internal crack length. The net decrease in the potential energy during crack growth is interpreted as the "energy release rate $\mathcal{G}$", and is equal to $2(\gamma_s+\gamma_p)$ as defined in equation (1.1).

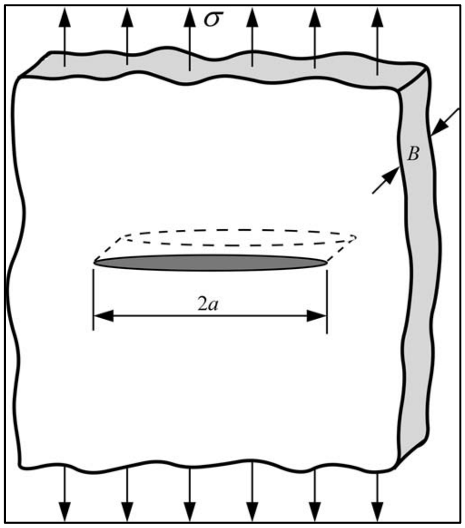

Figure 1-4 Cracked plate under remote tension loading considered by Griffith. Taken from Anderson (2005, p. 30 [7])

Apart from the fracture energy criterion described by Griffith, the stress conditions of a material behaving in a linear elastic manner, i.e. in accordance with Hook's law, can be described by a parameter called "stress intensity factor K". The approach describing stress conditions in a linear elastic body referred as Linear-Elastic Fracture Mechanics (LEFM). Considering the coordinate axis defined in Figure 1-5, the stress at the crack tip of a linear elastic body is described by:

$$\sigma_{ij} = \left(\frac{K}{\sqrt{2\pi r}} \right) f_{ij}(\theta) + \sum_{m=0}^{\infty} A_m r^{(m/2)} g_{ij}^{m}(\theta) \tag{1.2}$$

where, f_{ij} is a function of θ for the first term, and A_m and g_{ij} are a constant and a function of θ for the mth term, respectively. For any cracked body configuration, equation (1.2) is asymptotic to the first term for distances near the crack tip (r → 0):

$$\lim_{r \to 0} \sigma_{ij} = \left(\frac{K}{\sqrt{2\pi r}} \right) f_{ij}(\theta) \tag{1.3}$$

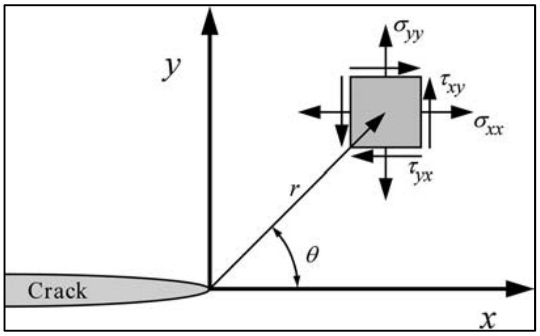

Figure 1-5 Coordinate axis at the crack tip used to define the stress field ahead of the crack. The z-axis is normal to the xy plane. Taken from Anderson (2005, p.43 [7])

A simple analytic solution for K exists for the configuration shown in Figure 1-4 (a through-thickness crack in an infinite plate):

$$K_I = \sigma\sqrt{\pi a} \tag{1.4}$$

where, K_I is the stress intensity factor in mode I (opening mode), σ is the remote stress, and a is half of the crack size. Therefore, it can be said that the amplitude of the K-dominated zone for this configuration is only related to the remote stress and half the crack size.

Equation (1.3) shows that the stress field near the crack tip is dominated uniquely by stress intensity factor K (elastic singularity or K-dominated zone). In the K-dominated zone where the stress field varies with the inverse square root of r, the stress tends theoretically towards infinity (equation (1.3)). This is not the case of real materials as the material deforms plastically when the yield stress is attained. Accordingly, a plastic zone is formed at the crack tip before crack grows further. Despite the fact that the elastic singularity does not exist within the plastic zone, but it can be surrounded by the K-dominated zone as long as the crack tip plastic zone remains small enough compared to the cracked body dimensions (i.e. small-scale yielding).

Irwin found that the energy release rate $\mathcal{G}$ can be related to the stress intensity factor K in LEFM in mode I:

$$\mathcal{G} = \frac{K_I^2}{E'} \tag{1.5}$$

where, K_I is the stress intensity factor in mode I, E' is equal to E and E/(1-ν^2) in plane stress and plane strain conditions, respectively, and ν is the Poisson ratio.

The elastic singularity defines a K-controlled fracture (a single-parameter fracture controlled uniquely by the stress intensity factor) as unstable crack initiation/propagation occurs when K reaches a critical value K_c. The K_c can be considered as a size-independent material property under small scale yielding and plane strain conditions, defined as "fracture toughness K_{Ic}". However, in the case of elastic-plastic materials (such as supermartensitic stainless steels), small-scale yielding requires very large samples and hence high loading capacity machines. LEFM is no longer valid when using small laboratory samples due to large-scale yielding conditions.

Another single-parameter fracture criterion is used to describe crack tip conditions in the case of elastic-plastic behavior: the J-integral proposed by Rice [39] in 1968. Rice idealized elastic-plastic behavior as non-linear elastic in which proportional loading occurs. Figure 1-6 compares non-linear elastic and elastic-plastic behaviors during loading and unloading. As can be seen in this figure, both behaviors have the same mechanical response during loading, while their unloading path is different: The unloading path is the same as that of loading for non-liner elastic behavior, whereas a linear unloading occurs for elastic-plastic behavior whose the slope is equal to the Young's modulus of the material. This shows that considering elastic-plastic behavior as non-linear elastic is a good approximation as long as no unloading occurs.

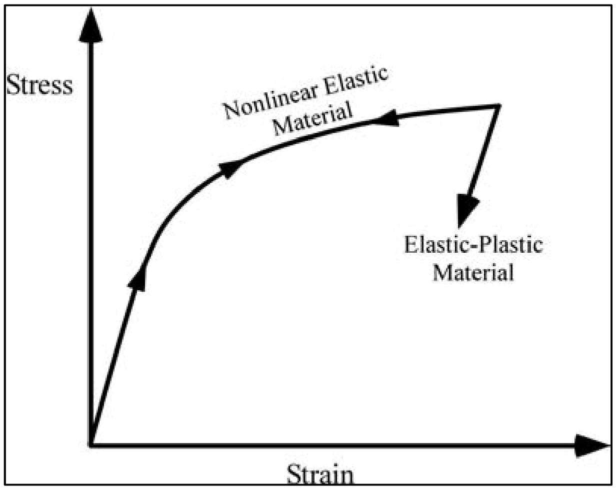

Figure 1-6 Schematic representation of stress-strain curve during loading/unloading for non-linear elastic and elastic-plastic behaviors. Taken from Anderson (2005, p. 108 [7])

J is the energy release rate in elastic-plastic behavior, and it remains valid even within the plastic zone where LEFM loses its validity. Similar to K in LEFM, the stress field at the crack tip is characterized by J in Elastic-Plastic Fracture Mechanics (EPFM) [40, 41]:

$$\sigma_{ij} = A\left(\frac{J}{r}\right)^{\frac{1}{N+1}} \tag{1.6}$$

where, r is the distance from the crack tip (Figure 1-5), A is a constant and N is an exponent measured experimentally using the Ramberg-Osgood stress-strain model to describe plasticity in a uniaxial tension test:

$$\frac{\varepsilon}{\varepsilon_0} = \frac{\sigma}{\sigma_0} + \beta\left(\frac{\sigma}{\sigma_0}\right)^N \tag{1.7}$$

where, ε and σ are true strain and true stress respectively, σ_0 is the yield stress, and β is a constant. Equation (1.7) defines a singularity equal to $1/\sqrt{r}$ in the case of a linear elastic material which is coherent with $N = 1$. This is consistent with equation (1.3) proposed for linear elastic behaviors.

Equation (1.6) defines a so-called "J-dominated zone" in which the stress is varied uniquely by 1/r (1/r singularity). The 1/r singularity is also referred as the HRR zone taken from the first letter of Hutchinson [40], and Rice and Rosengren [41] whose proposed it for the first time in 1968. The stress conditions are controlled by J in the J-dominated/HRR zone, and the crack growth is J-controlled. This J-controlled crack growth is schematically shown in Figure 1-7. As can be seen in this figure, the material behind the crack tip unloads elastically and, in addition, a "large strain region" in which non-proportional loading occurs does exist in front of it. It means that the elastic-plastic and non-linear elastic behaviors can no longer be assumed to be the same (as shown in Figure 1-6). However, the crack growth is still J-controlled since both unloading and large strain regions are embedded into the J-dominated zone [7]. In this case, the J value at the onset of crack growth under plane strain conditions is defined as the fracture toughness J_{Ic} which is considered as a material property.

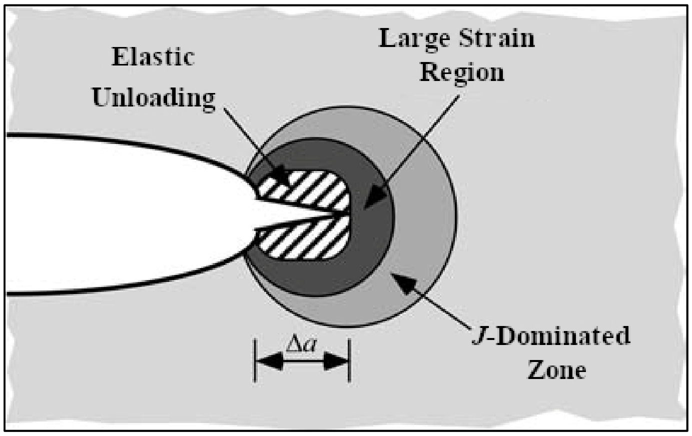

Figure 1-7 Crack growth in J-controlled stress field
Adapted from Anderson (2005, p.131 [7])

Furthermore, J in EPFM is analogous to $\mathcal{G}$ in LEFM, but relating J to $\mathcal{G}$ is not straightforward as the major part of the energy release rate J is stored in the material, leading to the formation of a plastic zone at the crack tip. However, Begley and Landes [42] demonstrated that equation (1.5) can be used at crack initiation under plane strain conditions i.e. only in the case of J_{Ic} value:

$$J_{Ic} = (1-\nu^2)\frac{K_{Ic}^2}{E} \tag{1.8}$$

They showed that the equivalent K_{Ic} calculated by this equation using measured J_{Ic} is numerically equal to the K_{Ic} value measured directly using very large samples under LEFM.

Unlike K_{Ic} which is defined as the resistance of material against unstable crack initiation, fracture toughness J_{Ic} is measured at the onset of stable crack growth. Therefore, the energy release rate J can be plotted against the corresponding crack growth (Δa), and a so-called J-Resistance curve (J-R curve) is traced, describing the whole resistance of material against stable crack growth.

There are two approaches for developing the J-R curve: the basic procedure (multiple specimen test method) and the resistance curve procedure (single specimen test method). In the case of basic procedure, testing each J_{Ic} sample results in a single measure of J (single-point fracture toughness), and hence multiple specimens are required to develop a J-R curve. However, in the case of resistance curve procedure, the same specimen is loaded several times resulting in multiple J values associated to each load/unload sequence. Therefore, the J-R curve can be developed by testing a single specimen using this procedure. In this study, the single specimen test method was used to develop the J-R curves of 13% Cr-4% Ni martensitic stainless steels resulting in a significant saving in money, material and time associated with sample machining and J_{Ic} testing. The detailed information on J_{Ic} test method is provided in ASTM E1820-18ae 1 [43].

Similar to K_{Ic} testing, the J_{Ic} sample is pre-cracked by fatigue cycling in order to create the sharpest possible notch. A typical force-displacement curve is shown in Figure 1-8. The partial unloadings are performed to measure the elastic compliance during crack growth i.e. the inverse slope of the lines no. 1 to 8 in Figure 1-8 (their slopes represent the stiffness of the specimen) [44]. These compliances are used to calculate the actual crack length. Then, to develop the corresponding J-R curve, J values are calculated and traced against Δa, as shown in Figure 1-9. The stress concentration at the crack tip leads to crack blunting before crack growth, resulting in an apparent crack growth [8]. The “blunting line” is then drawn to take into account this apparent crack growth [7]:

$$J = 2\sigma_I \Delta a \tag{1.9}$$

where,

$$\sigma_I = \frac{\sigma_y + \sigma_{UTS}}{2} \tag{1.10}$$

and σ_y and σ_{UTS} are yield and ultimate strengths, respectively. In order to collect the J values located in the J-dominated zone, two exclusion lines are drawn parallel to the blunting line at 0.15 mm and 1.5 mm. To generate the J-R curve, J values intercepted between these two exclusion lines are fitted to a power law relationship:

$$J = C_1 \Delta a^{C_2} \tag{1.11}$$

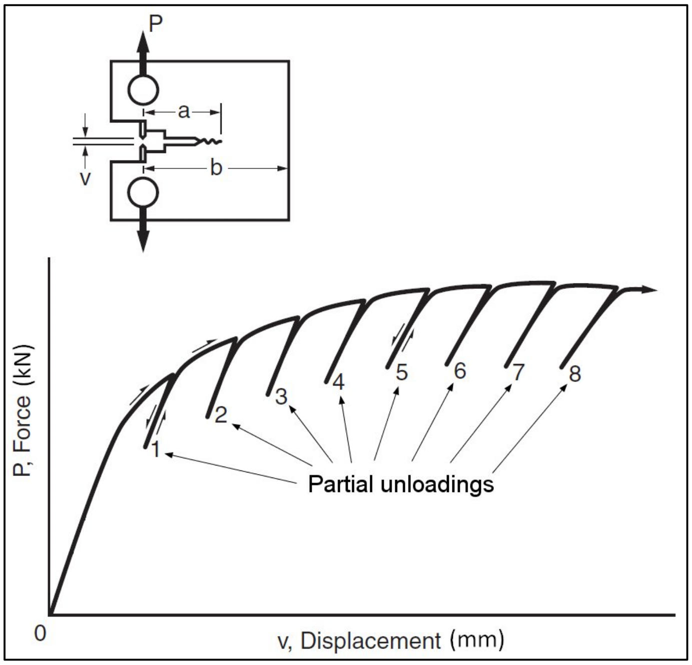

Figure 1-8 Typical force-displacement curve in J_{Ic} single specimen test method.
Taken from Dowling (2013, p.395 [44])

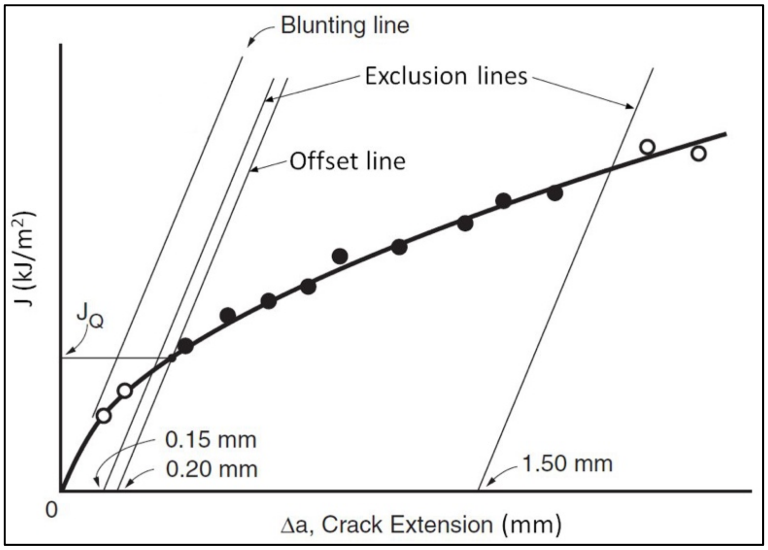

Figure 1-9 Typical J-R curve traced using measured J values in J_{Ic} single specimen test method
Adapted from Dowling (2013, p.397 [44])

The candidate value of fracture toughness J_Q is then determined at 0.2 mm crack extension at the intersection of offset line and the J-R curve. The J_Q is considered as the plane strain fracture toughness J_{Ic} of the material if both fatigue crack and J_{Ic}-crack extension fronts are straight, and the following size requirements are satisfied:

$$B,(W-a_0)\rangle 10\left(\frac{J_Q}{\sigma_Y}\right) \tag{1.12}$$

where, B is the thickness and W is the width of the J_{Ic} sample, and a_0 is the initial crack length.

The J-R curve (dJ/da) also provides important information about the resistance of the material against J_{Ic} crack growth, and can be considered as a material property [7]. The higher is the dJ/da value after initiation, the higher is the material crack growth resistance. A larger crack tip plastic zone requires the crack extension driving force (J) to be increased for further crack extension, leading to a rising J-R curve. In the case of rising J-R curves, the J_{Ic}-crack is highly stable and the risk of unstable crack propagation is zero during the test. In the case of less ductile materials, the crack tip plastic zone is relatively small compared to the sample dimensions, and flat J-R curves are developed as the crack extension driving force (J) and the plastic zone ahead of the J_{Ic}-crack reaches a steady state condition. Further crack extensions occur at the same J value and the stability of the J_{Ic}-crack is low and unstable crack propagation is highly risky. Performing a direct K_{Ic} test can be a good alternative to obtain a valid fracture toughness value in such situations.

To quantify the slope of the J-R curve, another criterion is also defined as “tearing modulus” [7]:

$$T = \frac{E}{\sigma_y^2}\frac{dJ}{da} \tag{1.13}$$

where, E is the Young’s modulus, and σ_y is the yield stress. This dimensionless criterion is proportional to the inverse square of yield strength.

To date, there is no complete database for mechanical properties of supermartensitic stainless steels and their welds in the literature, especially in the cases of fracture toughness J_{Ic} of the weld metal deposited by flux-cored arc welding (FCAW) process. In addition, there is even less information about fracture behavior of the heat affected zone (HAZ). Accordingly, performing fracture toughness tests in the HAZ along with that of the base and weld metals is of the great importance. Additionally, there is no comprehensive research on the effect of the microstructural features including distribution and size of inclusions on the mechanical properties of these materials.

1.4 Impact of the microstructural features on tension and stable/unstable crack growth properties

1.4.1 Matrix

The martensitic matrix is the most important microstructural feature contributing in high mechanical properties of supermartensitic stainless steels. Due to a carbon content lower than 0.6 wt.% [45], the martensite in these steels is of the lath type. One reason for the superior mechanical properties of the lath martensite is the very small size of its substructure, contributing in grain boundary strengthening mechanism [37]. The substructure hierarchy of the lath martensite is schematically shown in Figure 1-10. During martensitic transformation, each of the prior austenite grains divides into several packets. Each packet is composed of the blocks of the same habit plane (i.e. the plane on which martensite crystals form in austenite [46]), and each block is formed from laths of the same crystallographic orientation (variant) [47]. The laths are single crystals of martensite having widths of just several hundreds of nanometers [48]. The smaller the size of prior austenite grains, packets, and blocks, the higher is the martensite yield strength [49, 50]. In fact, the size of packets and blocks in the lath martensite is influenced by the prior austenite grain size, and smaller grains results in smaller packets and blocks [49]. On the other hand, studies made by Stonesifer and Armstrong showed that smaller prior austenite grains are resulted in higher fracture toughness K_{Ic} [51].

In addition to the grain boundary strengthening mechanism, solution hardening due to carbon is another mechanism contributing in the strength of martensite as martensite is a supersaturated solution of carbon atoms. It has been shown that the martensite yield strength (σ_y) is related to the square root of carbon content [50]:

$$\sigma_y(MPa) = 413 + 1.72 \times 10^3 (wt.\%C)^{0.5} \tag{1.14}$$

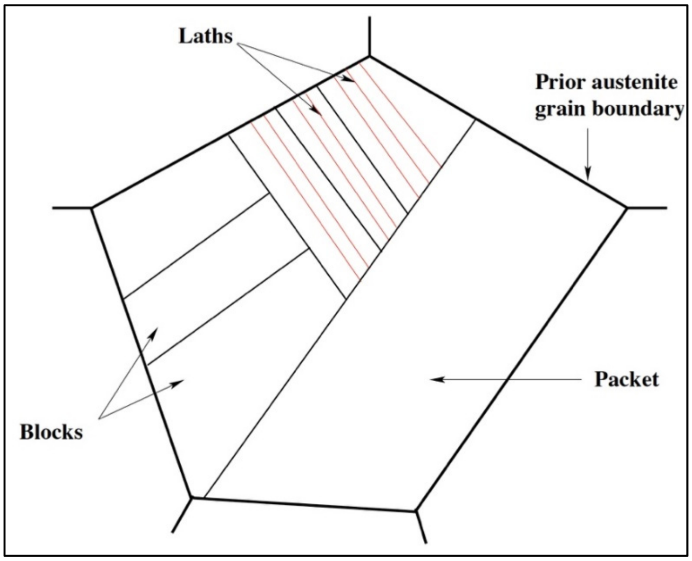

Figure 1-10 Schematic representation of the lath martensite hierarchies, contributing in grain boundary strengthening mechanism.
Taken from Carrouge (2002, p.16 [1])

Furthermore, the high dislocation density also contributes in the high strength of martensite as martensitic transformation generates a dislocation density of higher than 10^{10} dislocations per cm^2 which is as high as that in a heavily deformed steel [37, 38].

1.4.2 Delta ferrite

At the beginning, delta ferrite was known to have deleterious effects on the mechanical properties of chromium martensitic stainless steels, especially on fracture toughness and impact absorbed energy [12, 52, 53]. However, in 1998, Schäfer showed that the delta ferrite itself enhance the ductility and toughness since it is softer than the martensitic surrounding matrix [54]. By contrast, both yield and tensile strengths are decreased in the presence of delta ferrite. Therefore, there should be another reason for detrimental impacts of this phase on the mechanical properties of supermartensitic stainless steels. Schäfer showed that these are the large carbides forming during heat treatment at the delta ferrite boundaries which decrease the mechanical properties such as ductility and Charpy impact energy. These carbides are mainly of the type $M_{23}C_6$ (M is a mix of mainly Cr with some portions of Fe and Mo), acting as the sites of crack initiation. Fracture of these precipitations also facilitates the crack propagation during rupture [30, 55].

1.4.3 TRIP effect of austenite

In some alloys such as supermartensitic 13% Cr-4% Ni stainless steels, the austenite is thermally stable at room temperature, and even at cryogenic temperatures; however, it is mechanically unstable, transforming into martensite under plastic deformation by a so called “transformation-induced plasticity effect (TRIP)” [5, 12, 37]. In the case of supermartensitic 13% Cr-4% Ni stainless steels, TRIP effect has positive effects on the mechanical properties increasing the ductility and toughness [14, 56, 57]. The increase in the ductility is due to the fact that the strain hardening is retarded by the TRIP of austenite [58]. In the case of fatigue and fracture toughness testing, it can be said that the crack tip strain energy promotes TRIP, absorbing the energy required for creating two new surfaces. The TRIP effect can also blunt and arrest the crack during crack propagation. In addition, the formation of martensite results in compressive stresses as the specific volume of austenite is about 3% lower than that of martensite, resulting to stress relaxation at the crack tip [15].

Furthermore, it was shown that this is the timing of the TRIP effect that determines the efficiency of this phenomenon [37]. This is related to the mechanical stability of retained austenite. In the case of a very low stable retained austenite, the TRIP effect occurs long before necking, and the resultant fresh martensite decreases the ductility. In a similar way, crack propagation is accelerated through the less ductile fresh martensite, and the crack propagation resistance of the material will be decreased. Therefore, it can be concluded that optimum results will be obtained when the TRIP effect is occurred just before (very close to) necking, and very close to the crack tip during tension testing, and crack propagation, respectively.

1.4.4 Non-metallic inclusions

Flaws such as non-metallic inclusions are existing in microscopic scale. In almost all cases, fracture initiates from inclusions in engineering materials as these second-phase particles magnify the local stress. The role of inclusions on fracture micromechanics differs between cleavage and ductile rupture. For cleavage fracture, the role of inclusions is only confined to the initiation stage, and overall breakdown of the component occurs by unstable crack propagation right after fracture is nucleated [59]. However, in the case of ductile rupture the entire fracture micromechanics is controlled by inclusions.

Cleavage rupture occurs in body-centered cubic (BCC) metals. In the case of supermartensitic 13% Cr-4% Ni martensitic stainless steels, cleavage rupture is dominant at temperatures below about -80 °C [60]. Once fracture initiated on one or several inclusions, the material undergoes very small (negligible) deformations during cleavage rupture as unstable crack propagation occurs along crystallographic {100} planes. Micromechanics of cleavage are shown in Figure 1-11. As shown in Figure 1-11 (a), cleavage is transgranular having a multifaceted appearance in a microscopic scale since crack changes its direction in order for propagating through the most favorably oriented crystallographic plane within each grain. On a macroscopic scale, cleavage fracture surface is smooth and shiny because the cleavage facets are flat [7, 8]. The formation of river patterns is a typical characteristic of cleavage and they can be clearly identified on fracture surfaces. As shown in Figure 1-11 (b), these so-called rivers form when the original crack propagates on parallel crystallographic planes within a grain [8]. One of the reasons for the formation of these river patterns is that the original crack reaches a twist boundary within a grain [7, 8].

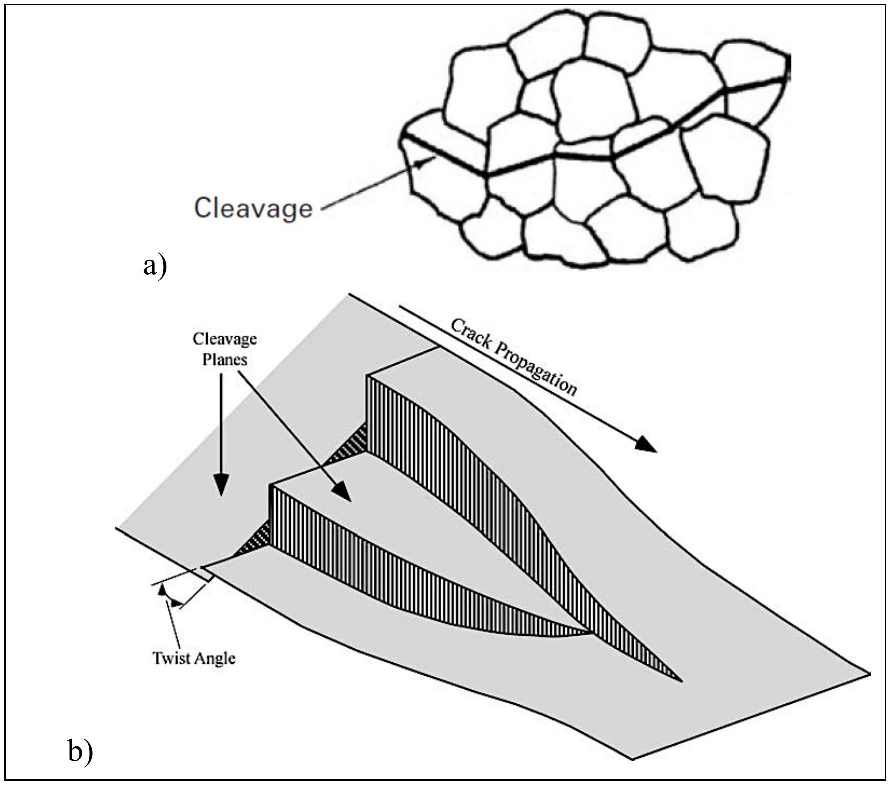

Figure 1-11 Micromechanics of cleavage rupture: (a) transgranular crack propagation path (Taken from Meyers and Chawla 2009, p.481 [38]), and (b) formation of river patterns within a grain (Taken from Anderson 2005, p.236 [7])

On the other hand, in the case of ductile rupture in which the fracture occurs by the coalescence of micro-voids, the role of inclusions is of great importance from the beginning to the end of rupture. This fracture mechanism called Micro-Void Coalescence (MVC) has three stages: nucleation, growth, and coalescence [7, 8, 37]. Ductile fracture micromechanics taking place at a crack tip is schematically shown in Figure 1-12. The crack tip stress triaxiality increases the stress to a level that is required for fracture initiation. The crack tip plastic zone results in crack blunting and micro-voids form on inclusions, growing under loading (Figure 1-12 (b)). Finally, coalescence occurs at the crack tip as shown in Figure 1-12 (c). The micro-void nucleation is the most critical stage, controlling the growth and hence the coalescence of micro-voids [61]: The higher is the inclusion density, the more micro-void nucleation sites are available, reducing the growth stage. As a result, a quasi-immediate coalescence will be occurred without having undergone large deformations during the growth stage. On the other hand, higher inclusion spacing (lower inclusion density) results in a more important micro-void growth stage [16, 17, 62, 63]. Therefore, it can be concluded that in a given material, higher inclusion spacing results in higher deformation during growth stage, and hence during ductile rupture [64]. Therefore, as the major part of the fracture energy is absorbed during the micro-void growth stage, for a given inclusion volume fraction higher inclusion spacing results in a higher ductility and a higher fracture toughness J_{Ic}/K_{Ic} value [63-65].

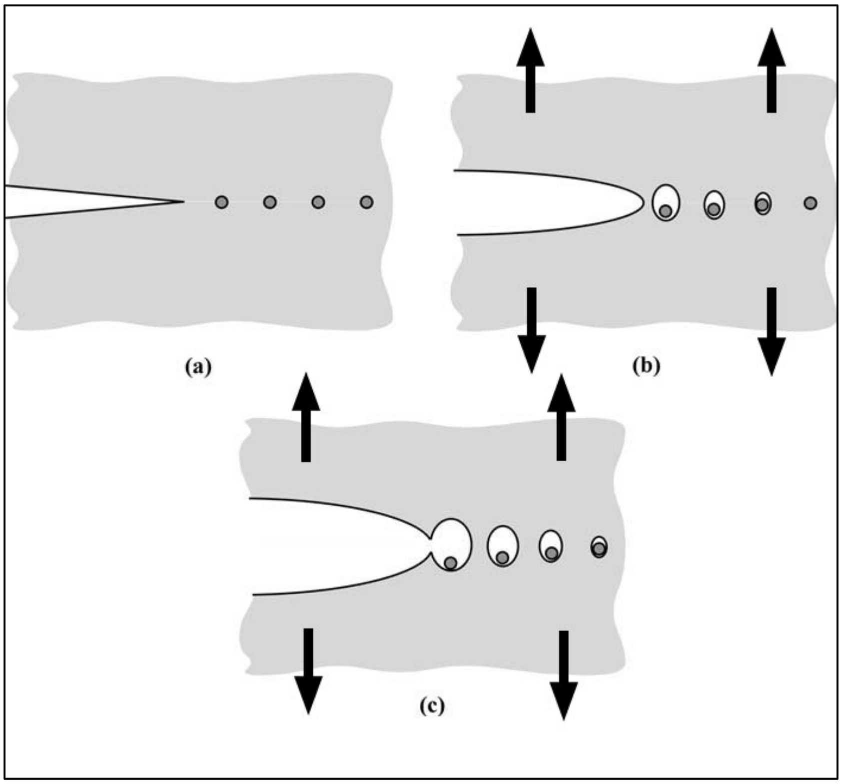

Figure 1-12 Schematic representation of crack growth by MVC mechanism. Adapted from Anderson (2005, p.232 [7])

Moreover, the inclusion size plays an important role at the onset of rupture. Studies showed that larger inclusions promote micro-voids at lower applied stresses and strains [66, 67]. In addition, fracture of inclusions is another mechanism lowering the required nucleation stresses and strains [7]. The inclusion characteristics affect both tension and fracture toughness properties in the same way; however, the region at which micro-void coalescence occurs is different between tension and J_{Ic}/K_{Ic} samples: In tension testing, the coalescence stage takes place at the center of the sample where stress triaxiality reaches its maximum value, whereas it occurs at the crack tip for a J_{Ic}/K_{Ic} sample, as shown in Figure 1-12.

To propose a model capable of describing ductile rupture, Rice and Tracey [68] considered the growth of a single spherical void in a perfectly plastic matrix that received significant attentions:

$$\frac{dR}{R} = \alpha \exp\left(\frac{3}{2}\frac{\sigma_m}{\sigma_y}\right) d\varepsilon_p \tag{1.15}$$

where, α is the growth rate constant, R is the void radius, σ_m is the mean stress, σ_y is the yield stress of the material, and $d\varepsilon_p$ is the increment of equivalent plastic strain for dR increase in the void radius. The model was modified by Escatha and Devaux [69] replacing the yield stress σ_y by the von Mises equivalent stress σ_{eq}. Therefore, as the stress triaxiality S_T is considered as equal to the σ_m/σ_{eq} ratio, it can be found that the modified model proposes an exponential relationship for the micro-void growth at a given stress triaxiality ratio. Huang [70] found that the constant of the Rice and Tracey model highly underestimates the micro-void growth in elastic-plastic materials, and then he proposes higher values for low ($1/3 \leq S_T \leq 1$) and high ($S_T \geq 1$) stress triaxiality ratios (section 2.1).

The Rice and Tracey model has achieved many successes in describing void growth in metallic materials to date. In particular, the fracture strain can be also estimated by considering the void radius at the moment of final rupture as the fracture criterion. The initial inclusion radius can be considered as the initial void radius R_i, as mostly always micro-voids are nucleated on the second-phase particles. Assuming that the coalescence stage takes place by the impingement of these nucleated micro-voids, half the average inclusion spacing can be considered as the final void radius R_f. It is well known that micro-void nucleation mainly occurs after necking [46], and hence the growth stage starts once necking is occurred until final rupture where these nucleated micro-voids coalesce. Under these hypotheses, the strain undergoing during micro-void initiation is ignored in the model of Rice and Tracey, and the fracture strain after necking can be estimated by integrating the equation (1.8) from R_i to R_f values:

$$\int_{R_i}^{R_f} \frac{dR}{R} = \alpha \int_{0}^{\varepsilon'_n} \exp\left(\frac{3}{2} S_T\right) d\varepsilon_p \tag{1.16}$$

where, ε'_n is the estimated fracture strain after necking (see section 2.3.2.3 for the complete integrated form of the modified model). Practically, it can be said that the ε'_n strain can be considered as fracture strain of engineering alloys with reasonable approximation as very small strains are undergone before necking, i.e., during micro-void nucleation stage, compared to the strains occur after necking.

In the case in which initially nucleated micro-voids are largely spaced, the final coalescence takes place by the formation of very small so-called “void sheets” due to strain localization in shear bands [66, 71]. A side-view of the void sheets formation between two nucleated micro-voids that are largely spaced is shown in Figure 1-13. Void sheeting is known to decrease the ductility as it stops the growth of the initially nucleated micro-voids, resulting in an immediate coalescence [64, 66].

Finally, it should be mentioned that supermartensitic stainless steels fracture in ductile manner at least for the temperatures of higher than -20 °C [1]. Therefore, as a hydroelectric runner operates in water where the minimum temperature does not fall below 0 °C and these alloys fracture in ductile manner, the mechanical characterization will be performed at ambient temperature in this study.

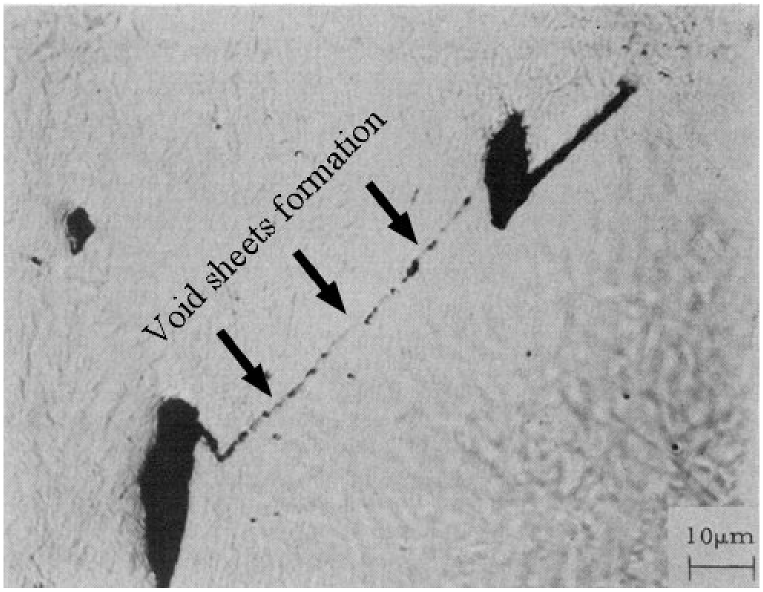

Figure 1-13 Micro-void coalescence occurred by void sheeting during tension test (side view), showing that void sheets are formed due to the relatively large spacing between two larger nucleated micro-voids. Taken from Cox and Low (1974 [66])

1.5 Conclusions

13% Cr-4% Ni martensitic stainless steels are used to manufacture hydroelectric runners, possessing superior mechanical properties e.g. a good combination of strength-ductility. Both manufacture and repair processes are usually made by FCAW process which resulted in a high-quality weld metal. However, on a microscopic scale, non-metallic inclusions and/or micro-cracks are mostly always exist in a welded component. These discontinuities act as stress raisers in the microstructure, promoting crack initiation/propagation under loading. That is why it is essential to define a single-parameter fracture criterion to characterize the crack tip stress field, defining the conditions in which crack propagation occurs. K and J controlled ruptures have already been described in the literature under LEFM and EPFM approaches, respectively. Based on these Fracture Mechanics approaches reviewed in this chapter, fracture initiation in supermartensitic stainless steels can be characterized using fracture toughness J_{Ic}; however, there is no complete database containing stable crack growth properties of base and weld metals of this category of stainless steels. Additionally, the literature showed that it is needed to consider the HAZ separately in terms of crack growth resistance as it is subjected to high thermal cycles resulting in microstructural discontinuities and high residual stresses. Once again, there is no literature on crack growth behavior of the HAZ in the welded joints of these steels.

The superior mechanical properties of these materials emanate from their complex microstructure. The microstructure and its most important features affecting the mechanical behavior were critically reviewed in this chapter. On the other hand, the literature showed that the base and weld metals of this category of stainless steels fracture in a ductile manner at least for the temperatures of higher than -20 °C at which inclusions play the major role. Then, the role of non-metallic inclusions during rupture was also reviewed in detail and the modified model of Rice and Tracey describing ductile rupture as a relationship between micro-void growth and S_T ratio was introduced. However, despite there being a large literature on the microstructure and inclusion behavior during rupture in general, the relationship among the microstructural features, inclusion characteristics, and mechanical properties (especially stable crack growth) are not well established for these steels.

The main purpose of this article-based thesis is to characterize fracture behavior of the base and weld metals, as well as the HAZ of 13% Cr-4% Ni martensitic stainless steels, describing microstructure-mechanical property relationships. In order to achieve this purpose, a weld metal block was deposited using FCAW process, tension and J_{Ic} tests were performed, and fracture surfaces were examined by SEM. Austenite contents and inclusion characteristics were measured from the microstructure of the base and weld metals. A model-based approach was also used to reveal ductile rupture micromechanical processes. The results obtained in this thesis were reported through three articles:

- ✓ Article 1: Various ductile fracture micromechanical processes were found among the base and weld metals using the modified model of Rice and Tracey. Some correlations between austenite content, inclusion characteristics, fracture micromechanics, and fracture strain were found. It was shown that different inclusion distributions in the microstructure results in different fracture micromechanical processes and that the fracture strain can be estimated using the size and half spacing of inclusions. Void growth-S_T relationships were demonstrated. For the base metals, rupture was defined as a relationship between micro-void growth amount and S_T ratio due to the large spacing between inclusions. However, in the case of the weld metals in which inclusion spacing is very small and rupture is controlled by micro-void nucleation stage, the matrix mechanical properties play an important role during ductile rupture.

- ✓ Article 2: This paper provided an opportunity to document how the mechanical properties of the matrix influences the fracture behavior of material in which rupture is controlled by the nucleation of micro-voids. The effect of low temperature intercritical heat-treatment on the ductile fracture behaviors of the weld metal were characterized. For the first time in the literature for this type of weld metal, J-R curves were developed for both conditions, and valid fracture toughness J_{Ic} values are extracted. Documenting the evolution of instantaneous strain hardening against true strain have shown how heat treatment improves the fracture behavior of the material. It was found that both, tempered martensite and TRansformation-Induced Plasticity (TRIP) of austenite retard void nucleation during straining.

- ✓ Article 3: J_{Ic} crack propagation behavior in the welded joint component materials of this category of stainless steels was thoroughly studied, and for the first time in the literature, the fracture toughness of the Heat-Affected Zone (HAZ) was obtained for both as-welded and heat-treated conditions. Unlike base and weld metals for which the J_{Ic} values were extracted from the J-R curves, one-point fracture toughness J_{Ic} values were calculated in the case of the HAZ (in accordance with ASTM E1820-18ae1 [43]) due to the occurrence of unstable crack propagation. The fracture toughness J_{Ic} of the HAZ was higher than that of the weld metal, whatever the heat treatment conditions. It shows that the weakest region in terms of crack propagation resistance in the welded joint of these materials is the weld metal. The post-weld heat treatment changed significantly the fracture behavior of the HAZ improving the fracture toughness J_{Ic}

value by a factor of 2.7 as the fracture mode transformed from a mix of dimpled rupture and cleavage into a totally dimpled rupture. The J_{Ic} value of the heat-treated HAZ reaches as high as that of the substrate steel (CA6NM).

CHAPTER 2

ARTICLE 1: ON THE DUCTILE RUPTURE OF 13% CR-4% NI MARTENSITIC STAINLESS STEELS

Fayaz Foroozmehr[1], Philippe Bocher[1]

[1]École de Technologie Supérieure (ÉTS), Montréal, Québec, Canada H3C 1K3

This chapter has been published as an article in the journal of “International Journal of Fracture”, April 2020, Volume 224, No. 1, pp. 67-82.

Abstract

Ductile rupture of 13% Cr-4% Ni martensitic stainless steels was examined during tension testing in order to better understand the role of second phase particles in these materials. SEM fracture surface examinations revealed that micro-voids were initiated from inclusions, and these inclusions were characterized from metallographic polished sections. Effect of stress triaxiality on the growth and impingement of the micro-voids were examined using a modified model of Rice and Tracey. In the case of the cast and wrought versions, the true fracture strains predicted for the measured stress triaxiality values were in a good agreement with the measured ones. For the weld metals, only the contribution of the micro-void growth cannot explain the experimental results, and it shows that the matrix properties such as austenite content and hardness of martensite play a significant contribution. The magnitude of the final stress triaxiality ratio measured after rupture was also related to the inclusion characteristics.

Keywords: Stress triaxiality; Void growth; Fracture strain

2.1 Introduction

13% Cr-4% Ni martensitic stainless steels possess high mechanical properties in terms of strength and toughness used to manufacture of hydraulic turbine runners [3-5, 11, 31, 72, 73].

These hydroelectric runner components are usually assembled using flux-cored arc welding (FCAW) process. This is a high-quality welding process; however, the existence of defects such as inclusions or small cracks in a welded structure is inevitable, which can result in crack propagation during service. The unstable crack propagation of these alloys have been reported to always take place in a ductile manner, except the ones occurring at very low temperatures (-75 °C or lower) [60]. A way to better understand and predict the deformation behavior before rupture of this category of stainless steels is to correlate metallographic examination with their mechanical behavior.

Ductile rupture happens by nucleation and growth, and finally coalescence of micro-voids [67, 74]. The mechanism involved is entitled “micro-void coalescence (MVC)”. Second phase particles and inclusions are the principal source of micro-void nucleation [7]. The growth of micro-voids is known to absorb the major part of the energy in ductile rupture [64]. However, if only a small number of nucleation sites are available, important micro-voids growth will take place. If, on the other hand, it occurs in large numbers, a premature coalescence will take place and the growth stage could be neglected [61]. Accordingly, the growth stage depends on the micro-void initiation sites density, and it can be said that ductile rupture is controlled by the nucleation of micro-voids [61]. In addition to the surface density of inclusions, the size, spacing, and volume fraction of these non-metallic particles is of great importance in ductile rupture [60].

Effects of the microstructural features, and especially the inclusion characteristics, on fracture of some steel alloys during ductile rupture were extensively examined in [16-19, 60]. It was shown that the non-metallic inclusions play the major role at the onset of rupture, and both the elongation at fracture or true fracture strain (ε_r) and the fracture toughness increase by increasing the spacing of inclusions. The size of inclusions is also of great importance as the larger is the inclusion size, the lower is the required nucleation stress and strain. In addition, the nature of the inclusions plays a role, as inclusions more resistant against rupture, and against micro-void formation result in higher fracture toughness. In addition, the austenite in 13% Cr-4 % Ni martensitic stainless steels is mechanically unstable, improving the mechanical properties. This mechanically unstable austenite transforms into martensite under loading, increasing significantly the ductility [2, 12, 27, 56]. Zhang et al [14] showed that in 13% Cr-4% Ni martensitic stainless steels this transformation-induced plasticity (TRIP) effect continues until final rupture. Due to the volumetric expansion occurring during martensite formation, some compressive strains are produced, and may decelerate the nucleation and growth of micro-voids.

The growth of an isolated void with a cylindrical shape in a perfectly plastic matrix was modeled by McClintock [75]. Considering the growth of a spherical single void Rice and Tracey [68] proposed a more realistic model still based on a perfectly plastic matrix:

$$\frac{dR}{R} = 0.283 \exp\left(\frac{3}{2}\frac{\sigma_m}{\sigma_y}\right) d\varepsilon_p \tag{2.1}$$

where R is the void radius, σ_m is the mean stress, σ_y is the yield stress of the material, and $d\varepsilon_p$ is the increment of equivalent plastic strain. Escatha and Devaux [69] modified the model by replacing the yield stress (σ_y) by the von Mises equivalent stress (σ_{eq}). The ratio σ_m/σ_{eq} in the equation being equal to the stress triaxiality factor S_T, Huang [70] modified the growth rate of the single void with respect to the stress triaxiality (S_T) as follows:

$$\frac{dR}{R} = 0.427 (S_T)^{0.25} \exp\left(\frac{3}{2} S_T\right) d\varepsilon_p \qquad \text{for } 1/3 \le S_T \le 1 \tag{2.2}$$

and

$$\frac{dR}{R} = 0.427 \exp\left(\frac{3}{2} S_T\right) d\varepsilon_p \qquad \text{for } S_T \ge 1 \tag{2.3}$$

This model proposes an exponential relationship between the growth rate of the void and the stress triaxiality. In fact, the material in the necked region is highly stressed and should contract, while being surrounded by lower stressed material [7, 37, 76]. This resistance of the material against contraction is called “constraint” [77], resulting to a triaxial stress state by producing radial and transversal stresses [7, 37, 76].

Using such an approach, the main purpose of this study is to examine the fracture behavior of 13% Cr-4% Ni martensitic stainless steels, focusing on the microstructural features and the stress triaxiality. Accordingly, the modified Rice and Tracey model by Huang is used. After a brief presentation of the materials (chemical composition and heat treatment), the experimental procedures used in this study is presented. Metallographic examinations including inclusion characterization analyses, tension tests, fractographic examinations, and XRD analyses are used to document the inclusion characteristics, the actual fracture surfaces of broken tension samples, and the austenite contents of the materials. The stress triaxialities calculated from the geometry of the necking region, are used to calculate the equivalent fracture strains (ε) based on the inclusion characteristics measured on the metallographic polished sections and the radius measurements made on the fracture surfaces. The results are then compared with the experimental data.

2.2 Materials and experimental procedures

Three different 13% Cr-4% Ni alloys were studied: one cast (CA6NM), one wrought (415), and one weld metal (410NiMo), as provided in (Table 2-1). The expression “base metals” will be used to refer both CA6NM and 415 steels in order to differentiate these materials from the deposited weld metal. The base metals were tested in the tempered condition. The cast steel was austenitized at 1050 °C and tempered at 610 °C; the wrought one was austenitized at 1000 °C and tempered at 600 °C. Both steels were quenched in air. The weld metal block was deposited by flux-cored arc welding process (FCAW), and was tested in both, as-welded and heat-treated conditions (600 °C for two hours). As seen in Table 2-1, the studied materials had similar chemical compositions, and were in the category of 13% Cr-4% Ni martensitic stainless steels.

Table 2-1 Chemical compositions of the tested materials (wt%). Measurements were performed using inductively coupled plasma-emission atomic spectrometry (C and S were measured by combustion)

Designation	Cr	Ni	Mo	C	Mn	P	S	Si
CA6NM steel	12.79	3.49	0.55	0.016	0.50	0.019	0.007	0.26
415 steel	13.021	3.91	0.56	0.028	0.73	0.022	0.002	0.34
410NiMo weld metal	12.1	4.67	0.61	0.027	0.04	0.01	0.0093	0.48

Metallographic sections of the base and weld metals were polished to a mirror appearance using sand papers and diamond suspensions. The mirror polished surfaces were then examined by optical microscopy to study the defects such as porosity and inclusions existed in the microstructure of the tested materials. Five optical micrographs were taken randomly from all over the polished surfaces of each of the materials. In comparison to the base metals for which a low-level 50X magnification was used, a much larger magnification of 500X was needed for the characterization of the weld metal due to the small size of the inclusions. As a result, the examined surface was much smaller in the case of the weld metal; a total surface of 14 mm^2 versus 0.15 mm^2 was examined, respectively. The measured area fraction of inclusions were converted into the volume fraction of inclusions since the area fraction of the phase of interest measured on a section is equal to its volume fraction [78]. In this study, the inclusion volume fractions were measured using an automatic image analyzer software (ImageJ) [78].

The surface densities of defects (N_A) were measured for each image, and then reported for a square centimeter. The equivalent circle radii of the measured defects were calculated and an average value was reported as the initial defect radius (R_0) for each of the materials. The defect spacing was calculated by the equation $S=1.78R_0(V_v)^{-1/3}$, where V_v is the defect volume fraction, $R_0=(\pi/4)H(R)$, and $H(R)$ is the harmonic mean of the measured defects radii [16].

To reveal the microstructures, the mirror polished surfaces were then etched using modified Fry’s solution (150 mL distilled water, 1 g $CuCl_2$, 50 mL HNO_3, and 50 mL HCL) in a similar way reported in [5, 60].

Three tension tests per material/condition were carried out in accordance with ASTM E8/E8M [79] using a strain rate of $2.5 \times 10^{-4}\ s^{-1}$ at room temperature. The area section of the samples was about 20 mm^2 as smooth round bar specimens with a diameter of 5 mm were used. Up to necking, the stress triaxiality (S_T) is equal to 1/3 at the center of a round bar tension specimen. At the onset of necking, the stress triaxiality (S_T) increases continuously due to the increasing of the constraint [71]. The stress triaxiality was calculated at the center of the necked region from the broken tension samples using Bridgman's relation [80]:

$$S_T = \frac{1}{3} + \ln\left(1 + \frac{r_0}{2\mathbb{R}}\right) \tag{2.4}$$

where r_0 is the radius of the necked region and $\mathbb{R}$ is the radius of curvature of necking at the moment of final rupture. These parameters were measured precisely on the images taken from the necked regions of the broken samples, using an image analyzer software "Image J".

The metallographic polished sections as well as the fracture surfaces were examined by scanning electron microscopy (SEM). At least 155 SEM micrographs were examined for each of the base and the weld metals. Inclusion radii were measured on the fracture surfaces of the tested materials. As automatic measurements were not possible in this case, inclusions were measured one by one manually using high magnifications to perform precise measurements. Note that the size of broken inclusions was ignored and only the intact ones were only considered for fracture surface measurements, introducing eventually an artifact. Therefore, in the condition in which a considerable number of large inclusions had been already fractured upon rupture, it is expected that the inclusion radius measured on the fracture surface is smaller than the actual ones.

As these materials can have austenite after tempering, the contents of this phase were measured by X-ray diffraction (XRD) using the Rietveld method [81]. A Bruker D8 Advance diffractometer equipped with a copper tube and a nickel filter was used. Diffraction patterns were obtained in the range $40° < 2\theta < 140°$ with a step size of 0.05° [5]. The samples were cut by an automatic cut-off machine using 0.5 mm thick saw blades with a cut speed of 0.05 mm/s to minimize austenite transformation to martensite during the cutting process. Cut surfaces were ground by 1200 grit sand papers and etched in a 30% HCl + 30% HNO_3 + 40% H_2O

solution for 10 minutes, then etched in HCl for 30 seconds. Three samples were prepared from each material to measure the initial austenite content.

2.3 Results

2.3.1 Inclusion characteristics

Examples of the analyzed optical micrographs taken from the metallographic polished sections of the studied materials are shown in Figures 2-1 (a) to (c). The observed surfaces are perpendicular to the tension axis for the wrought steel (415) and the weld metal (410NiMo). The metallographic and tension samples were taken randomly in the case of the cast steel (CA6NM), whereas for the weld metal the tension direction was perpendicular to the welding direction. The measured particles were inclusions in all the three micrographs as verified by SEM. The lowest possible magnification was used for the base and weld metals in order to characterize the largest inclusions in each of the materials since the largest inclusions play the major role in ductile rupture.

The inclusion characteristics (surface density N_A, volume fraction V_v, radius R_0, and half of spacing S/2 of inclusions) of the base and weld metals measured from the optical micrographs are compiled in Table 2-2. Inclusions were not of similar size ranges in the microstructure of the base metals, and both very small and very large inclusions were found in the microstructures of CA6NM and 415 steels. In other words, no single normal distributions were found for these materials. On the contrary, the standard deviations of the half of inclusion spacing S/2 values are low for each of the tested materials, showing that the inclusion spacing is normally distributed in each case. The effect of inclusions of different size ranges were considered to shed light on the ductile fracture of the base metals. To this purpose, the average size of the small and large inclusions was reported and the median radius ($R_{0median}$) was used as a discriminating parameter. In the case of CA6NM steel, the median radius was equal to 3.73 μm, and for 415 steel it was of 2.73 μm. Note that the average value of the inclusions smaller or equal to the $R_{0median}$ will be referred as R_{0S}, and that of the ones larger than $R_{0median}$

as R_{0L}, in this study. On the other hand, the distribution of inclusions in the weld metal could be fit with a normal distribution and the mean inclusion radius is a good representative for all inclusions in this case.

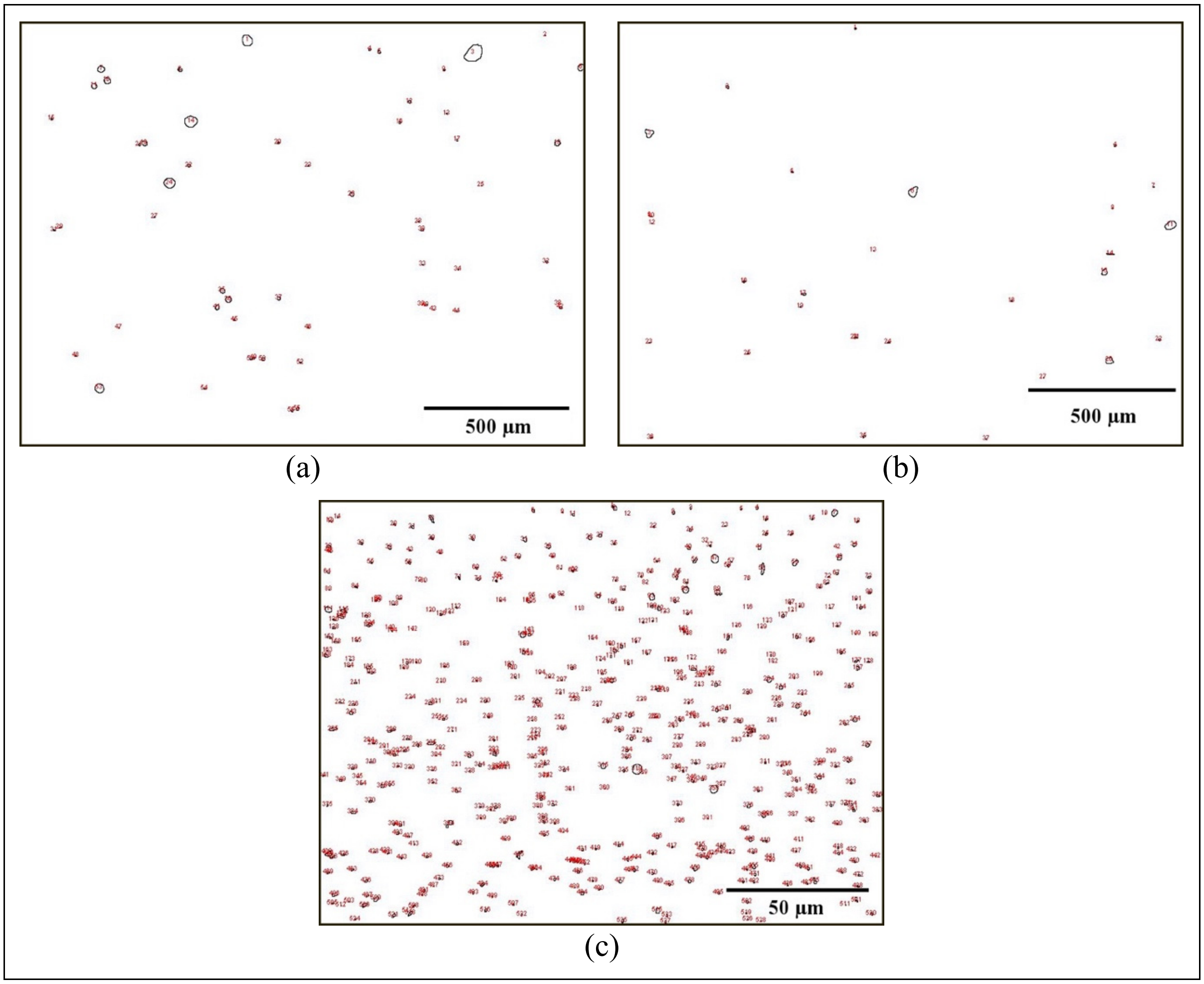

(a) (b)

(c)

Figure 2-1 Examples of processed images analyzed by automatic quantitative metallography: (a) CA6NM steel, (b) 415 steel, and (c) 410NiMo weld metal. The numbered circles are detected inclusions whose surfaces were measured on mirror polished surfaces

Even of the significant error intervals, the characteristics of the cast material show systematically higher values than 415, except for inclusion spacing, for which equal values were obtained. Inclusions are at least five times smaller in the weld metal than those in the base metals. Similarly, the spacing of inclusions is at least 19 times smaller in the weld metal resulting in a surface density of all inclusions (N_A) about 800 times higher than in the base metals. The inclusion volume fraction (V_v) was also more than 5 times higher.

Table 2-2 Inclusion characteristics measured on the metallographic polished sections. R_{0S} represents $R_0 \leq R_{0median}$; R_{0L} represents $R_0 > R_{0median}$

Material	Measured inclusions	N_A (No./cm^2)	V_v (%)	Mean R_0 (µm)	Mean S/2 (µm)
CA6NM steel	R_0 (All)	1627 ± 368	0.22 ± 0.12	4.99 ± 4.31	18.53 ± 2.86
	R_{0S}[a]	873 ± 232	0.02 ± 0.01	2.63 ± 0.79	28.27 ± 2.50
	R_{0L}[a]	754 ± 176	0.20 ± 0.11	7.73 ± 5.05	35.88 ± 3.35
415 steel	R_0 (All)	1211 ± 242	0.09 ± 0.02	3.59 ± 3.21	18.02 ± 1.84
	R_{0S}[b]	695 ± 208	0.01 ± 0	1.91 ± 0.52	28.78 ± 3.06
	R_{0L}[b]	516 ± 180	0.08 ± 0.02	5.69 ± 3.96	35.02 ± 2.22
410NiMo weld metal	R_0 (All)	$(1.29 \pm 0.25) \times 10^6$	1.10 ± 0.14	0.38 ± 0.24	0.94 ± 0.05

[a]- $R_{0median}$ is equal to 3.73 µm for CA6NM steel. [b]- $R_{0median}$ is equal to 2.73 µm for 415 steel.

Inclusion size distributions of the metallographic polished sections are shown Figure 2-2. In the case of the weld metal (410NiMo), almost all inclusions (more than 98%) measured on the metallographic polished sections are smaller than one micrometer in radius and the inclusion sizes cannot be ranked in a meaningful way. However, for the base metals (CA6NM and 415) it can be said that the median radius $R_{0median}$ classifies the results in two major size ranges i.e., R_{0S} and R_{0L} (as described in Table 2-2).

The microstructures of the tested materials are shown in Figures 2-3 (a) to (e). The microstructures are mostly composed of lath martensite, but the stringers of delta ferrite can also be found in the microstructure of CA6NM and the weld metals for both as-welded and heat-treated conditions. The presence of delta ferrite is due to the concentration of some ferrite-promoting elements (especially Cr) as reported in [2, 27]. The stringers of delta ferrite are shown by the black arrows in the microstructure of CA6NM (Figure 2-3 (a)) and in that of as-welded material (Figure 2-3 (d)). In the case of the weld metal, the stringers of delta ferrite are narrow and trapped in the former Widmanstätten austenite boundaries. This type of the delta ferrite is typical of such welded microstructures as reported in [1] and [73]. Very fine inclusions in black closely dispersed in the microstructure are also seen. The microstructure of the tempered martensite shown in Figure 2-3 (e) displays a stronger contrast than that of fresh martensite (Figure 2-3 (c)). The austenite islets cannot be observed in these micrographs, requiring much higher magnifications. It is the concentration of austenite-promoting elements (especially Ni) in austenite during intercritical heat treatment that stabilizes this phase at room temperature [2, 27].

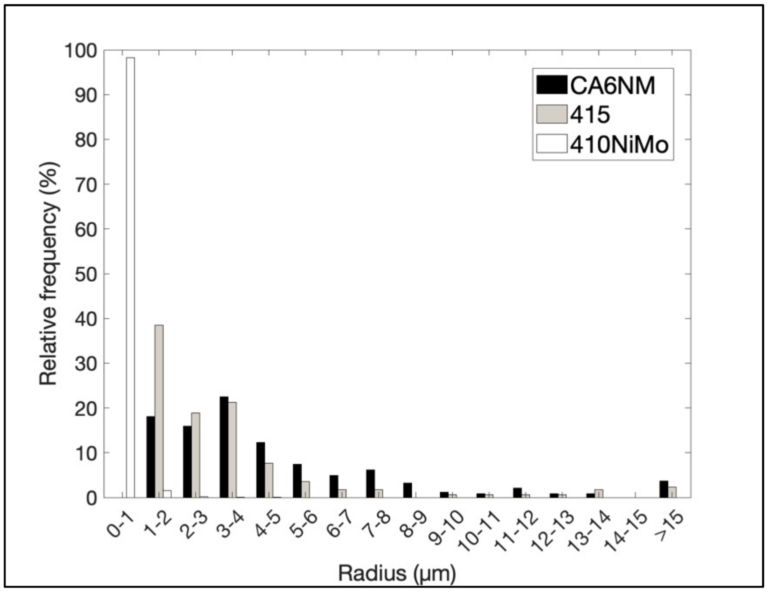

Figure 2-2 Inclusion size distributions measured on metallographic polished sections

2.3.2 Ductile rupture

2.3.2.1 Measured deformations during tension testing

The engineering stress-strain curves of the tested materials were converted to the true ones until the onset of necking, as shown in Figure 2-4. The yield (σ_y) and ultimate tension strengths (σ_{UTS}), true strain before necking (ε_{bn}), the true fracture strain (ε_r), the fracture strain after necking (ε_n) (which is the difference of ε_r minus ε_{bn}), and the austenite contents (γ_0) of the tested materials are provided in Table 2-3. The ε_{bn}, ε_r, and ε_n values were calculated using the following equations [76]:

$$\varepsilon_{bn} = \ln\,(1+e) \qquad (2.5)$$

where “e” is the engineering strain, and:

$$\varepsilon_r = 2\ \ln\left(\frac{D_0}{D}\right) \tag{2.6}$$

where D is the final radius, and D_0 is the initial radius of the tension specimen, and:

$$\varepsilon_n = \varepsilon_r - \varepsilon_{bn} \tag{2.7}$$

As provided in Table 2-3, the weld metals undergo higher yield and ultimate tension strengths than the base metals, but experience lower ductility. On the other hand, the CA6NM steel is the least resistant, but reaches high rupture strain. The heat-treatment at 600 °C for two hours has improved the ε_n deformation, maintaining approximately the same yield strength (the difference between the yield strength of these two metallurgical states is only about 2%). For both base metals similar amounts of deformation took place before necking (ε_{bn}). The heat-treated weld metal underwent 75% higher deformation before necking than the as-welded one. In the case of the true fracture strains (ε_r), 415 steel underwent the largest one. Its ε_r deformation was 23% higher than the CA6NM steel, and 38% higher than the weld metals.

As the base metals underwent equal ε_{bn} deformations (Table 2-3), it can be said that differences in the ε_r and ε_n deformations between CA6NM and 415 steels are mainly due to their damaging process after necking, i.e., their different inclusion characteristics (Table 2-2 and Table 2-4). On the other hand, the differences between the as-welded and heat-treated weld metals can be related to their differences in term of martensite and the austenite contents since they have similar inclusion characteristics. Therefore, the softer tempered martensite of the heat-treated material together with four times higher austenite content introducing TRIP effect resulted in higher ε_{bn} and ε_r values.

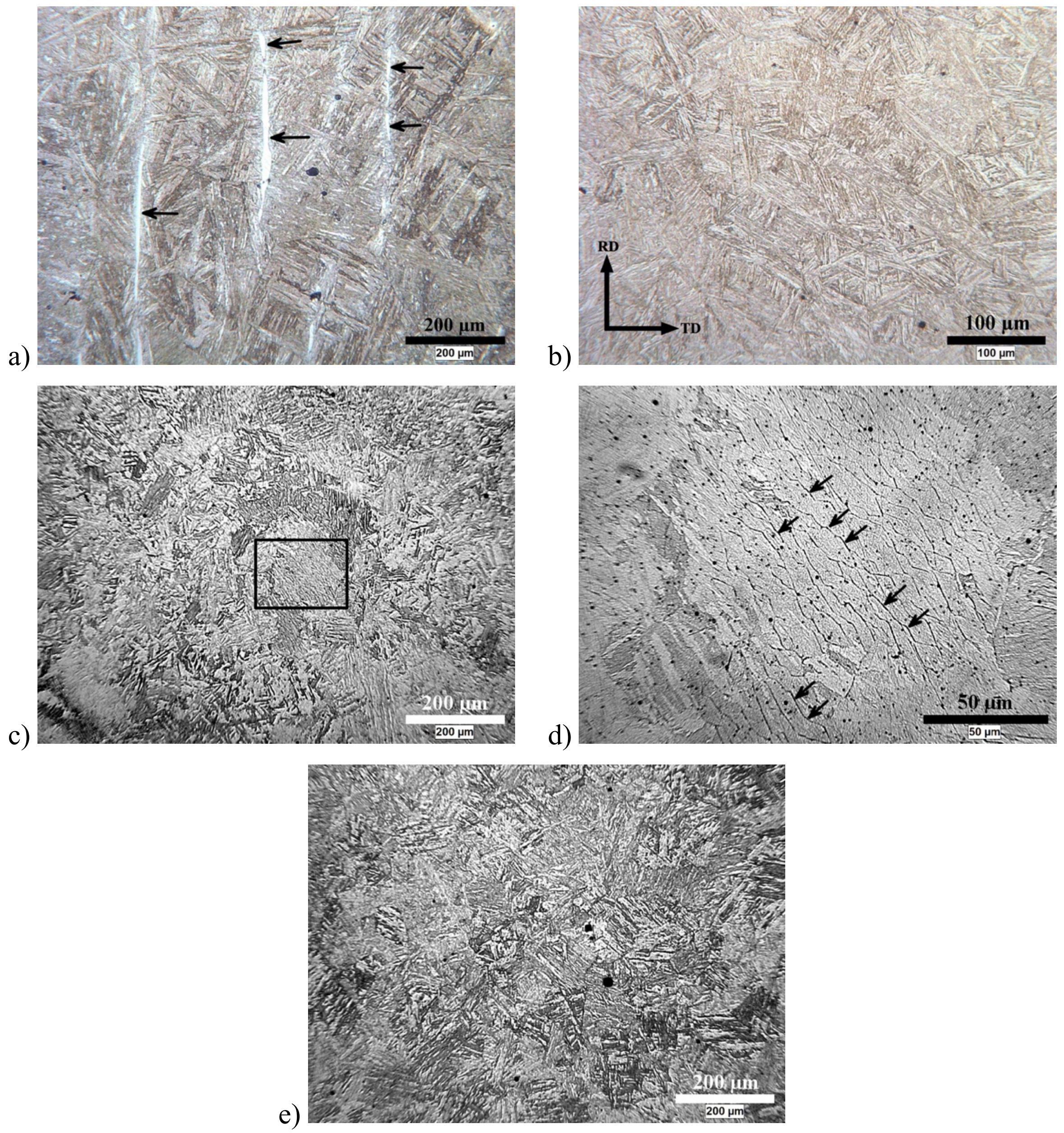

Figure 2-3 Optical Microstructures of the tested materials: (a) CA6NM, (b) 415, (c) 410NiMo-AW, (d) enlargement of the outlined area by the black rectangle in (c), and (e) 410NiMo-HT. The black notched arrows in (a) and (d) show the stringers of delta ferrite. In (b), RD and TD represent the Rolling Direction and Transverse Direction, respectively

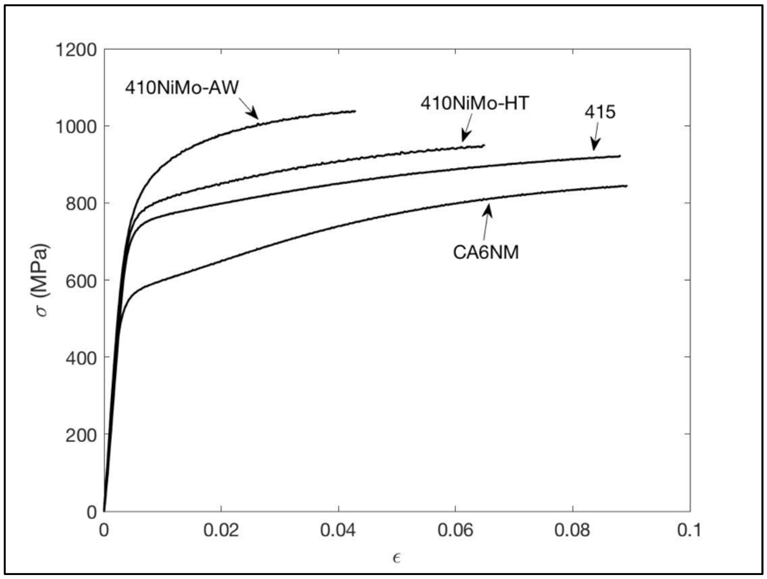

Figure 2-4 Typical σ-ε curves of the tested materials. Only one curve per material is shown; however, three tests were performed on each material

Table 2-3 Tension properties as well as austenite contents of the tested materials

Designation	σ_y (MPa)	σ_{UTS} (MPa)	ε_{bn}[a]	ε_r	ε_n	γ_0 (%)[b]
CA6NM steel	575 ± 13.2	769 ± 7.4	0.09	0.99 ± 0.11	0.90	19.1 ± 6.4
415 steel	725 ± 0	843 ± 3.7	0.09	1.22 ± 0.06	1.13	19.5 ± 2.2
410NiMo-AW	783 ± 5.8	1007 ± 10.3	0.04	0.64 ± 0.04	0.60	2.4 ± 1.0
410NiMo-HT	765 ± 5	895 ± 4	0.07	0.75 ± 0.08	0.68	10.0 ± 0.6

[a]- Equal ε_{bn} deformations were obtained for each of the tests performed on each material.
[b]-Austenite percentages.

2.3.2.2 Fracture surfaces

Fracture surface examinations using SEM showed that fracture occurred by the mechanism of micro-void coalescence (MVC) for all metals, but the contribution of inclusions to rupture was significantly different from one metal to the next. Large inclusions were found in large number on the fracture surfaces of CA6NM steel, while small ones were reported for 415 steel. On the other hand, almost all inclusions observed on the fracture surfaces of the weld material, both as-welded and heat-treated conditions, were of the same size and the occurrence of larger inclusions was negligible. The nature of inclusions were also examined using Energy Dispersive X-ray (EDX) spectroscopy as reported in the previous work [60]. In addition, it should be noted that no evidence of the presence of delta ferrite or large chromium carbides that may be formed in this phase [54] were found on the fracture surfaces. Therefore, it can be concluded that the trace of delta ferrite does not affect the fracture of these alloys.

Typical examples of fracture surfaces are shown in Figure 2-5. Large inclusions of more than 5 µm in radius are indicated by black arrows in the CA6NM fracture surface in Figure 2-5 (a). In addition, numerous inclusions were found broken in the fracture surface of CA6NM steel. These large/broken inclusions are the basis of premature micro-void formations since lower strains are needed than those required from smaller/intact inclusions to initiate micro-voids [7, 66, 67]. As shown by the outline filled black ellipse in Figure 2-5 (a), premature micro-voids led to the formation of very large dimples (a final radius up to 55 µm at the moment of rupture). An example of a large dimple formed by a large fractured inclusion on CA6NM fracture surface is displayed in Figure 2-5 (b).

In the case of 415 steel, the fracture appearance looks more complicated than that of CA6NM steel. As seen in Figure 2-5 (c), the fracture surface is rougher and many small voids are found. Figure 2-5 (d) is a higher magnification micrograph of the black rectangle shown in Figure 2-5 (c), showing some of the initially nucleated micro-voids by the black arrows. The very small voids found in this figure are making angles of about 40° with loading axis (shown by the black arrows) and correspond to what was called “void sheets” [66, 82, 83]. The formation of these void sheets results in a considerable number of secondary cracks. If at the early stage of necking micro-voids are initiated on larger inclusions as lower deformations are required, the final rupture is controlled by void sheeting between these large micro-voids. They form when the constraint reaches a critical value in shear bands. These initial micro-voids are similar to the ones formed in CA6NM; however, the growth of the micro-voids is interrupted by the formation of the void sheets in this case as there are only few available micro-void nucleation sites of this type in the material. In addition, the nucleation sites of the micro-voids are also different in CA6NM and 415 steels as micro-voids were formed on small/intact inclusions in 415. Therefore, since there are not enough inclusions to initiate micro-voids homogeneously in the material, void sheets are formed at high stress/strain levels as the constraint get increased by necking. The mean radius of the initially nucleated micro-voids at the moment of void sheeting R_{vs} is equal to 6.36 µm ± 2.03 µm for 35 micro-voids on 415 steel fracture surfaces. As the density of micro-voids varies from one location to another, secondary cracks are generated to connect the region with higher density of formed micro-voids, completing the final coalescence.

On the other hand, in the as-welded material (410NiMo-AW) the inclusions and the corresponded dimples are approximately of similar sizes as can be seen in Figure 2-5 (e). Some inclusions are shown by the black arrows in this micrograph. The fracture appearance of the heat-treated material was very similar as that of the as-welded one.

Table 2-4 provides the mean value of the inclusion radius measured from the fracture surfaces of each of the tested materials. In the case of the base metals, relatively large standard deviations show that the inclusion sizes measured on fracture surfaces cannot be properly described by normal distributions. However, comparing these average values with inclusion sizes measured on the metallographic polished sections (Table 2-2) can adequately demonstrate the micromechanical processes involved in each case: the inclusions larger than the median radius $R_{0median}$ initiate micro-voids in CA6NM, while this is the case of smaller ones in 415 steel. Inclusions found on the fracture surfaces are at least four times larger for the base metals compared to the weld metals. In addition, the mean inclusion radius of CA6NM steel was about 3.5 times larger than that of 415 steel. Inclusions had a similar size for both as-welded and heat-treated materials. The stress triaxialities at the center of the necked region measured from broken tension samples (using equation (2.4)) was also added to this table. The stress triaxialities were higher for the base metals.

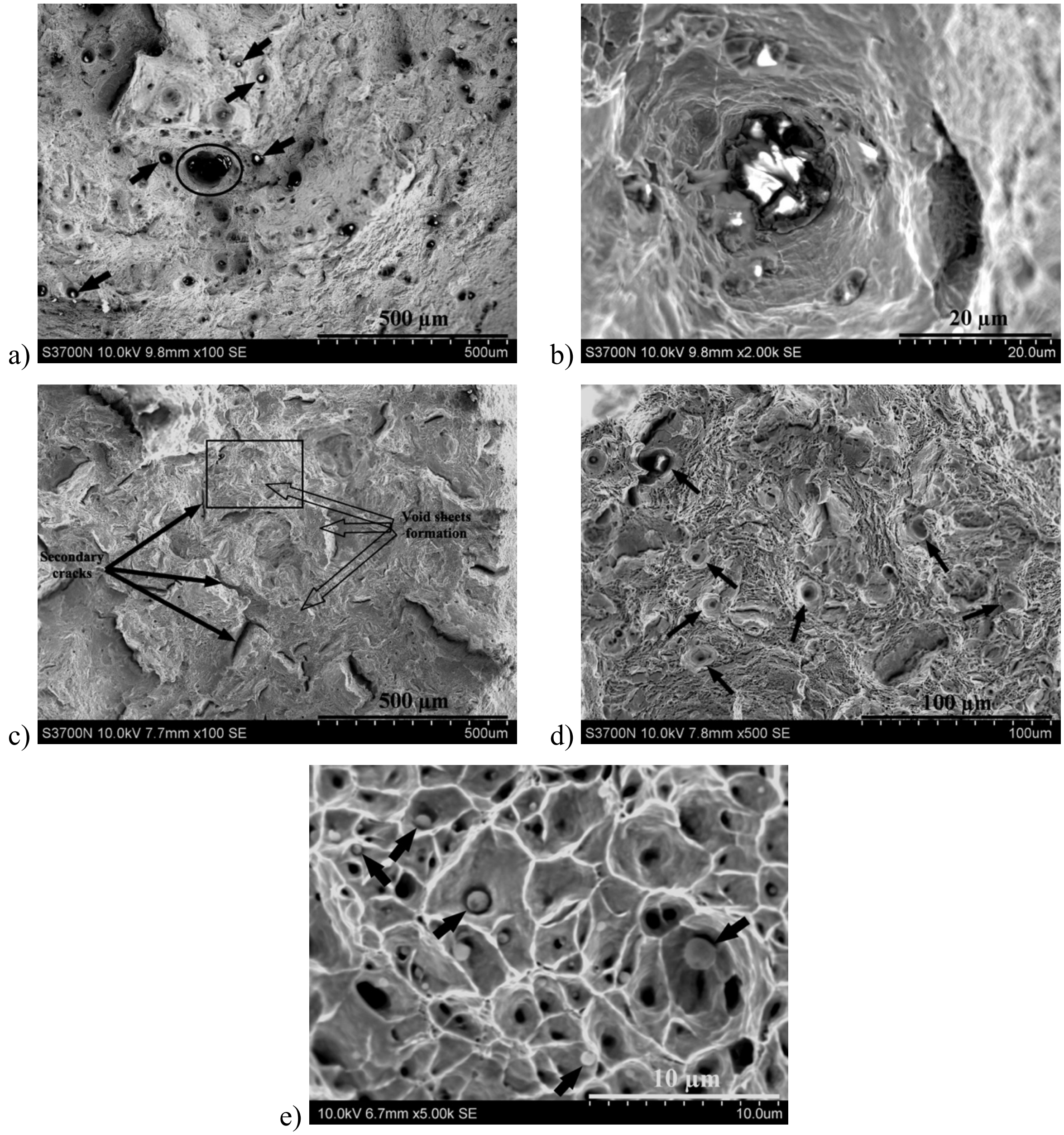

Figure 2-5 Examples of SEM micrograph of the tested materials: CA6NM at (a) 100X, and (b) 2000X magnifications, (c) 415 steel at 100X magnification, (d) the region shown by the black rectangle in (c), and (e) 410NiMo-AW at 5000X magnification. In (a) some inclusions larger than 5 µm in radius are shown by the black arrows, and a very large dimple of 55 µm in radius formed before total breakdown of specimen is shown by the outline filled black ellipse. In (c) the filled arrows show some secondary cracks, and some facets formed by void sheeting are shown by the outline filled arrows. In (d) some initially nucleated micro-voids are shown by the black arrows. In (e) some inclusions are also shown by the black arrows. Note that loading axis is perpendicular to all the fracture surfaces shown in this figure

Table 2-4 Mean inclusions radii measured on tension fracture surfaces and stress triaxialities at the center of the necked region obtained from broken tension specimens

Material	R_0' (μm)	S_T
CA6NM steel	6.23 ± 4.15	0.71 ± 0.02
415 steel	1.8 ± 1.12	0.77 ± 0.04
410NiMo-AW	0.43 ± 0.24	0.64 ± 0.04
410NiMo-HT	0.43 ± 0.14	0.66 ± 0.05

In order to shed light on the inclusion contribution to rupture, the inclusion radius measured after rupture R_0' (Table 2-4) is compared with the ones measured on the metallographic polished section of the material (Table 2-2). In the case of CA6NM steel, the R_0' is close to the R_{0L} (Table 2-2) indicating that large inclusions played the major role in the rupture of this alloy. On the other hand, in 415 steel the R_0' is very close to the average radius of small inclusions suggesting that it is the local inclusion density that controlled the fracture mechanism, and the contribution of large inclusions is negligible.

In the welded materials, the difference between the mean radius of inclusions measured on the metallographic polished section and that measured on the fracture surfaces is negligible. This is true for both as-welded and heat-treated conditions. Accordingly, it can be said that all inclusions observed on the metallographic polished section of the weld metal had the same chance to initiate micro-voids if necking happens in that region.

2.3.2.3 Fracture strain estimation

After necking, the smooth tension sample can be considered as a notched bar with a small radius equivalent to the necked region r_0 and the radius of curvature of necking $\mathbb{R}$. In fact, the variation in the stress triaxiality from the onset of necking until final rupture was not considered in the model of Rice and Tracey, and it was considered constant during necking [84]. As necking is due to mechanical instability, and that void nucleation and growth take place at the last stage of fracture (way after necking, when the stress triaxiality S_T reaches high values), it was assumed that the growth and coalescence of the initially nucleated micro-voids occur rapidly just before rupture. The necked region radius r_0 and the curvature radius of necking $\mathbb{R}$ are thus assumed constant during crack nucleation and propagation. With that hypothesis, rupture takes place under constant stress triaxilaity ratio S_T. Both final rupture and interaction between voids were not considered in the model of Rice and Tracey (equation (2.1)). To remedy these problems, the final void radius at the moment of rupture was considered as fracture criterion in the integrated form of the modified Rice and Tracey model (equation (2.8)). That is to say, the interaction between voids is also considered. Accordingly, the fracture strain after necking (ε_n) can be estimated by integrating equation (2.2) as a function of the void radius (R) for a constant S_T. The value of the calculated fracture strain after necking ε'_n is then equal to:

$$\varepsilon'_n = 2.342 S_T^{(-1/4)} \ln\left(\frac{R_f}{R_i}\right) \exp\left(-\frac{3}{2} S_T\right) \qquad (2.8)$$

where ε'_n is the equivalent fracture strain, S_T is the stress triaxiality during necking, R_i and R_f are the initial and final void radius, respectively (the equation (2.3) was ignored as the measured and calculated stress triaxiality values are lower than one in this study). As final rupture takes place by the impingement of the micro-voids, only the behavior of an isolated void ($\ln(R_f/R_i)$) can be considered to estimate the equivalent fracture strain, and the plastic deformation that is required for the nucleation of micro-voids once necking has taken place is neglected. The obtained values can then be compared with the experimental results given by ε_n values provided in Table 2-3.

According to the equation (2.8), the initial and final radius of the voids are very important in dimpled rupture and different fracture strains can be considered based on the inclusion characteristics provided from the metallographic polished sections (Table 2-2), or the average inclusion radius measured on the fracture surfaces (Table 2-4).

Based on the fracture surface observations (section 2.3.2.2), the inclusions contributing the micro-void coalescence (MVC) are different from one material to the next: Inclusions larger and smaller than the median radius played the major role in the rupture of CA6NM and 415 steels, respectively, and all inclusions contributed to rupture for both weld metals conditions.

As a consequence, the R_{0L} and R_{0S} values (Table 2-2) are considered as the initial void radius R_i in CA6NM and 415, respectively. Again, based on the fractographic considerations, the final void radius in the MVC mechanism was estimated as the average value of the spacing of larger inclusions (R_{0L}) in CA6NM, and that of the smaller ones (R_{0S}) in 415.

The estimated ε_n values are reported in Table 2-5 for the S_T values obtained from broken tension samples (Table 2-4). Higher deformations than the measured ones are obtained. These values are 50% and 89% higher for CA6NM and 415 steels, respectively. It is most likely that the final radius of the micro-voids (R_f) was overestimated by considering that only large or small inclusions play a role in the MVC mechanism in CA6NM and 415 steels, respectively.

Table 2-5 Predicted ε'_n deformations of the base metals based on the inclusions larger and smaller than the $R_{0median}$ value in CA6NM, and 415, respectively, measured on the metallographic polished sections

Material	S_T	R_i (μm)	R_f (μm)	ε'_n	ε_n	Relative difference (%)
CA6NM steel	0.71	7.73	35.85	1.35	0.9	+ 50
415 steel	0.77	1.91	28.78	2.14	1.13	+ 89

As the coalescence is occurring by impingement of the micro-voids formed on both small and large inclusions, a more realistic estimation can be obtained by considering the inclusion radius measured on the fracture surfaces R'_0 as the initial micro-void radius for both steels (Table 2-4). The final void radius R_f in CA6NM is to consider half of spacing of all inclusions S/2 (Table 2-2). This hypothesis comes from the observation that fracture surfaces of CA6NM steel are composed of both small and large dimples (Figure 2-5 (a)). The growth of the micro-voids initially nucleated on large inclusions is limited by the onset of micro-voids from small inclusions in the ligaments when stress and constraint increase. In the case of 415, the actual radius measured on 415 fracture surfaces (see section 2.3.2.2) and equivalent to the R_{vs} at which void sheets take place is considered as R_f. The ε'_n values calculated based on these assumptions are reported in Table 2-6. The results show better prediction of the ε_n deformations, especially for CA6NM as with these asssumptions, micro-voids were nucleated on both large and small inclusions and not only on the large ones. In the case of 415, replacing the R_f value by the measured R_{vs} results in an underestimation of the ε_n deformation. This underestimation suggests that the formation of void sheets stops the growth of micro-voids, and the deformation resulting from void sheeting (ε_{vs}) is negligible. Accordingly, comparing the ε'_n deformations predicted in Table 2-5 and Table 2-6 for 415, it is possible to state that the failure in this alloy takes place by the impingement of the micro-voids formed on smaller inclusions. It can be said also that the formation of void sheets results in a decrease of ε_n deformation as it dramatically accelerates the damage.

Table 2-6 Predicted ε'_n deformations of the base metals based on the inclusion size measurements on the fracture surfaces R'_0 as the initial void radius R_0, as well as half of spacing of all inclusions in CA6NM and the R_{vs} value in 415 as the final void radius R_f

Material	S_T	R'_0 (μm)	R_f (μm)	ε'_n	ε_n	Relative difference (%)
CA6NM steel	0.71	6.23	18.53	0.96	0.9	+ 7
415 steel	0.77	1.8	6.36	0.99	1.13	- 12

For the weld metals, all inclusions were in the similar size range, and additionally all of them contributed to rupture. Therefore, the measured inclusion radius from fracture surface R'_0 (Table 2-4) and half of the mean spacing of all inclusions S/2 (Table 2-2) is considered as R_0 and R_f values, respectively. Predicted ε'_n deformations of the weld metals are provided in Table 2-7. The predicted ε'_n deformation can be qualified as overestimated but acceptable for the heat-treated material, whereas the error is quite significant for the as-welded condition. The heat treatment has a negligible effect on the yield strength of the weld metal (Table 2-3). The characteristics of the inclusions being the same for these metallurgical conditions and the measured stress triaxialities were similar, equation (2.8) predicts that the ε'_n deformation of the heat-treated material is about 4% lower than that of the as-welded one, but the measured ε_n is 13% higher for this metallurgical condition compared to that of the as-welded one. It shows that microstructural features other than the void radius i.e., the austenite transforming into martensite by TRIP and the softer tempered martensitic matrix play a role in ductile fracture behavior of the weld metal.

Table 2-7 Predicted ε'_n deformations of the weld metals based on the R'_0 and the mean value of half of spacing of all inclusions measured on the metallographic polished sections

Material	S_T	R'_0 (μm)	R_f (μm)	ε'_n	ε_n	Relative difference (%)
410NiMo-AW	0.64	0.43	0.94	0.79	0.60	32
410NiMo-HT	0.66	0.43	0.94	0.76	0.68	12

It is interesting to look at the effect of the different void radii defined in this paper on the resultant stress triaxialities as based on the modified Rice and Tracey model. Equation (2.8) was used to calculate the stress triaxiality values using the R_i and R_f values defined in Table 2-5 and Table 2-6 for the base metals, and those defined in Table 2-7 for the weld metals using the measured ε_n deformations. Table 2-8 reports the resulted S_T values. For each of the base metals, two series of results are reported: the first row is attributed to the R_{0L} in the case of CA6NM and R_{0S} for 415. The second row provides the information obtained from fracture surface observations for both these steels. By contrast, the same critical micro-void growth rate was considered for both as-welded and heat-treated conditions.

Table 2-8 Calculated stress triaxialities for different initial radius R_i and final radius R_f of micro-voids defined in Table 2-5, Table 2-6, and Table 2-7, and measured ε_n deformations

Material	R_i (μm)	R_f (μm)	ε_n	Calculated S_T	Measured S_T	Relative Difference (%)
CA6NM steel	7.73	35.83	0.90	0.93	0.71	+ 31
	6.23	18.53		0.74		+ 4
415 steel	1.91	28.78	1.13	1.13	0.77	+ 47
	1.8	6.36		0.70		- 9
410NiMo-AW	0.43	0.94	0.60	0.78	0.64	+ 22
410NiMo-HT	0.43	0.94	0.68	0.72	0.66	+ 9

When using R_{0L} and R_{0S} as the microstructural characteristics, the S_T values obtained are highly overestimated suggesting that the final micro-void radii were overestimated, resulting in much higher constraints and stress triaxiality values at rupture. However, as the growth of initially nucleated micro-voids were limited by micro-void initiation on small inclusions in CA6NM and void sheeting in 415, R_f values was redefined as the S/2 (half of spacing of all inclusions reported in Table 2-2) for CA6NM and R_{vs} (actual radius of the micro-voids at the moment of void sheeting) in 415 steel. This led to better S_T predictions. In other words, these fracture micromechanical processes were activated when the constraint and stress triaxiality reach their critical values, promoting final rupture.

For the as-welded material, the difference between the calculated and measured stress triaxialities is significant (22%), but this difference decreased significantly in the heat-treated material with only 9% higher than the measured one. As the critical micro-void growth is the same between both as-welded and heat-treated conditions (Table 2-7), it can be concluded that some microstructural features other than the initial and final radius of the micro-voids influence the material behavior during necking.

2.4 Discussion

The available data set gives the opportunity to study the effect of the matrix microstructural features i.e., the austenite and martensite on fracture behavior of the alloys. The microstructures of the tested materials have different amounts of austenite, resulting in the possibility for some TRIP to take place until final rupture for the alloys containing the larger amounts. During TRIP, austenite transforms into martensite under loading, enhancing strain hardening even at late stage of deformation. This effect is known to delay void growth and increase the ductility of the alloy [14, 15]. In addition, the volume change associated with the transformation of austenite to martensite also retard the nucleation of micro-voids by producing compressive stresses, and thus requiring higher ε_{bn} deformations for final rupture [14, 15]. Therefore, the higher austenite contents of the CA6NM and 415 alloys (Table 2-3) enable the base metals to undergo higher ε_{bn} and ε_n deformations. The austenite content of the heat-treated weld material does not play a significant role in the MVC mechanism because the number of void nucleation site is very high compared to the number of austenite islets.

For the base metals, one can assume that both steels have similar TRIP properties as they have undergone similar heat treatments, and the austenite content is approximately the same (19% as provided in Table 2-3). The martensitic matrix in the 415 steel has a higher strength than the CA6NM due to high carbon content, but it can be assumed that the TRIP effect would result in equal increase in their deformation behaviors as both steels undergo the same deformation before necking ($\varepsilon_{bn} = 0.09$). After necking, they underwent different deformation paths (Table 2-3) and their critical void growths (R_f/R_i) are of different natures (Table 2-4). The difference between their fracture strains is related to their different inclusion characteristics, which lead to different fracture micromechanical processes. In the case of the weld metal, the metastable austenite contents are different between the as-welded and heat-treated conditions (Table 2-3) and efficient TRIP can occur only in the heat-treated condition. This behavior explains the larger ε_n deformation after necking as TRIP in this condition is active until final rupture [14].

Comparing the true strains after necking ε_n provided in Table 2-3 shows that 415 steel is the most ductile material, having an ε_n deformation of about 1.13, at least 26% and 66% larger than those of CA6NM and the weld metals, respectively. These different ε_n deformations can be explained by their various inclusion characteristics and metastable austenite contents, resulting in different abilities for void growth once mechanical instability has initiated necking. The void growth amounts taking place during necking, provided by $\ln(R_f/R_i)$, are equal to 1.26, 1.09, and 0.78 for 415, CA6NM, and the weld metals, respectively. These values show a correlation between the void growth and the true strains after necking: the larger void growth, the larger ε_n. Similarly, larger stress triaxiality values are found for larger ε_n (Table 2-4), i.e., larger stress triaxiality ratios are required for rupture to be occurred.

The presence of metastable austenite can also play a role in the damage mechanism, but in the case of 415 and CA6NM steels they have similar austenite content (Table 2-3) and it can be concluded that the 26% higher ε_n deformation of 415 steel compared to CA6NM is mostly due to 16% higher ability to growth void before failure.

Inversely, both 410NiMo-AW and 410NiMo-HT materials underwent the same amount of void growth (Table 2-2), but the metastable austenite content found in the heat-treated material together with the softer tempered martensite has the ability to increase by 13% the deformation after necking ε_n.

The differences in necking strains of the various steels are explained based on the experimental results and physical arguments. Even if the integrated form of the modified model of Rice and Tracey (equation (2.8)) presents some limitations as one needs to assume that void nucleation and coalescence take place at the end of the necking process and that the triaxiality state does not change, this model allows determining the total amount of the void growth taking place at the final rupture using the natural logarithm of the R_f/R_i ratio. This simplified approach may not represent adequately the complexity of the mechanisms happening after necking, but it has the advantage to differentiate the amounts of void growth in the tested materials and discriminate the related fracture micromechanics during necking as discussed below.

While conventional impingement of the initiated micro-voids was observed in both materials, void sheets were also observed in 415 steel. The consequence of void sheet formation is a lower constraint at rupture. The void sheets formed as an alternative way to adapt to the constraint as micro-void formation on the smaller inclusions would require much higher constraints. In fact, some regions of the microstructure present a low density of small inclusions (Figure 2-5 (c)). In other words, void sheeting resulted in a lower stress triaxiality than the expected one (by about 40%) if the final radius of the initially nucleated micro-voids is decreased by at least 75% compared to the expected value. The case of CA6NM steel is less straightforward if only large inclusions (R_{0L}) are considered to play a role in rupture. A 31% higher stress triaxiality value was obtained according to the modified model of Rice and Tracey. However, while the S_T value increases after necking, the nucleation process activates small inclusions, reducing by about 50% the final radius of the cavities (R_f). An R_f value equal to half of the mean spacing of all inclusions resulted in a precise S_T (Table 2-8) prediction, showing that small inclusions do contribute to rupture.

The weld metals ruptured at nearly the same low triaxiality values (Table 2-8). The predicted S_T values are overestimated for both cases, but the prediction error is lower for the heat-treated material (9% vs 22%). The lower S_T prediction error for the heat-treated material may be due to efficient TRIP and the softer matrix as discussed earlier, but it could also be due to some limitations in the Rice and Tracey model, even in its modified form. Helbert and coworkers [85] have showed that ductile rupture can hardly be expressed by the Rice and Tracey model when the nucleation of micro-voids occurs in very large numbers under a low stress triaxiality and low plastic deformation. This is because nucleation of micro-voids plays a major role than growth: only the growth stage of one void cannot capture the actual failure process. This limitation would be even more dramatic for the as-welded material due to its low ductility. Therefore, it is possible that the fracture behavior of the weld metal cannot be expressed by the S_T-void growth rate relationship defined in the modified model of Rice and Tracey. In the case of the base metals, the nucleation sites (inclusions) were much less numerous (the inclusion spacing is about 20 times higher than in the weld materials) resulting in a significant micro-void growth for each void, justifying the ability for the modified Rice and Tracey model to describe their fracture behavior.

Finally, it is interesting to shed light on the stress triaxiality ratios S_T measured on broken tension samples. Among the three heat-treated materials, the highest S_T value was produced in 415 steel for which the critical micro-void growth rate is the highest one (despite void sheets formation at a later stage of the fracture process). The impingement of the nucleated micro-voids occurred at a lower S_T ratio in the CA6NM steel because the critical micro-void growth is 16% lower, resulting in a lower ε_n. Finally, the weld metals have similar low S_T values, not affected by the different matrix properties. Accordingly, the lower S_T value of the heat-treated weld metal compared to the base metals was not due to its lower austenite content (being half that in the base metals) or higher martensite strength, but rather by its high, small size inclusion density. Therefore, the magnitude of the stress triaxiality ratio due to necking is related to the inclusion features rather than the matrix properties. It shows that in order to develop a model describing precisely ductile fracture behavior of the material, the inclusion characteristics and especially the size and spacing of inclusions should be also considered. In addition, the inclusion spacing in the weld metal is so small that the growth of the micro-voids is negligible and rupture is most likely controlled by their nucleation rates rather than growth, resulting in low final stress triaxiality values and small ε_n deformations.

2.5 Conclusions

The quantitative metallography done in this work measuring the volume fraction, size, and spacing of inclusions, gave the possibility to discriminate the fracture micromechanical processes of various 13% Cr-4% Ni martensitic stainless steels. Some correlations between material's microstructure, austenite content, failure features, and measured true fracture strains were explored using the modified Rice and Tracey model.

The conventional MVC mechanism was found as the main fracture mechanism after necking. The microstructural feature affecting the micromechanical processes during ductile rupture is the inclusion characteristics, and to some extent the matrix ductile behavior. The size and spacing of inclusions control the amount of void growth during necking. The measured stress triaxiality ratios using broken tension samples also showed that a higher void growth requires a higher stress triaxiality ratio.

In addition, various micromechanical scenarios were found in the studied metals. In the case of a rolled 415 steel, the MVC mechanism was interrupted by the formation of void sheets. Considering the radius of the initially nucleated micro-voids at the moment of void sheeting resulted in a better estimation of the deformation after necking. It was demonstrated that the formation of the void sheets in this steel inhibits the predicted true fracture strain to be attained by stopping the void growth and decreasing the constraint. The large inclusions found in the cast version (CA6NM) of this steel were found to be the ones to initiate damage, but final rupture occurs thanks to the activation of much smaller inclusions. The very large number of potential micro-void nucleation sites found in weld metals limited the possibility for void growth and resulted in lower stress triaxiality ratio at rupture. This drastically reduced the strains after necking.

In the situation of the welded metals, the relationship between void growth and stress triaxiality ratio defined in the Rice and Tracey model is not efficient at describing the fracture behavior. Another element that is not taken in the Rice and Tracey model was considered when comparing the behavior of the as-welded and heat-treated metals: the effect of the matrix mechanical property. It was found that when applying an intercritical tempering heat treatment, the same amount of void growth took place, while larger true fracture strain was found in the softer matrix material. Even if the improvement is not significant (of the order to 13%) it shows that this parameter should be considered in further improvement of the Rice and Tracey model.

Acknowledgments

Financial supports of Natural Science and Engineering Research Council of Canada (NSERC), Hydro-Québec, and Alstom Power Hydro are gratefully acknowledged. SEM, XRD and Rietveld analyses were performed at the Institut de Recherche d'Hydro-Québec (IREQ). The tension tests were carried out at École Polytechnique de Montréal under supervision of Mr. Yves Verreman. The authors of this paper would also like to thank Mrs. Manon Provencher, Mr. Étienne Dallaire, Mr. Alexandre Lapointe, technologists at IREQ, and Mrs. Josée Laviolette, technologist at École Polytechnique de Montréal for their valuable experimental assistance. Finally, we would like to express our warm thanks to Mr. Mathieu Paquin for the manufacture of the weld metal block of exceptional quality.

Compliance with ethical standards

Conflict of interest The authors declare that they have no conflict of interest.

CHAPTER 3

ARTICLE 2: EFFECT OF LOW TEMPERATURE INTERCRITICAL HEAT-TREATMENT ON STABLE CRACK GROWTH BEHAVIOR IN 13% CR-4% NI MARTENSITIC STAINLESS STEEL MULTIPASS WELDMENTS

Fayaz Foroozmehr[1], Philippe Bocher[1]

[1]École de Technologie Supérieure (ÉTS), Montréal, Québec, Canada H3C 1K3

This chapter has been published as an article in the journal of "Engineering Fracture Mechanics", October 2020, Volume 240, Article number: 107360.

Abstract

Tension and fracture toughness J_{Ic} tests were performed on both as-welded and heat-treated conditions. The softer tempered martensitic matrix and the transformation-induced plasticity (TRIP) of reformed austenite improved significantly the strain hardening behavior of the heat-treated material. These matrix characteristics were found to retard micro-void nucleation during straining. The onset of necking, the elongation at fracture, and the fracture toughness J_{Ic} were improved by 55%, 28% and 90%, respectively. These results provide an opportunity to document how the matrix mechanical properties influence the fracture behavior of material which rupture is controlled by the nucleation of micro-voids.

Keywords: Flux-cored arc welding process; Martensite; Microstructural features; Ductile rupture; J-Resistance curve

Nomenclature

a_0	initial crack length
D	inclusion diameter
E	Young’s modulus
e	engineering strain
e_f	elongation at fracture
e_u	uniform elongation at necking
H(D)	harmonic mean value of inclusion diameters
J	J-integral value for a given crack growth
J-R curve	J-Resistance curve
J_{Ic}	initiation J value under plane strain condition
J_Q	fracture toughness J_{Ic} candidate value
K	stress intensity factor
K_{Ic}	plane strain stress intensity factor
n	strain hardening coefficient
N_A	surface density of inclusions
n_i	instantaneous strain hardening coefficient
P	engineering stress
S	inclusion spacing
S_T	stress Triaxiality ratio
T	tearing modulus
V_v	volume fraction of inclusions
W	sample width
Δa	crack extension
ΔK	stress intensity factor amplitude
ε	true strain
ν	Poisson ratio
σ	true stress
0.2% σ_y	0.2% offset yield strength
σ_y	yield strength

σ_{UTS}	tensile strength

Acronyms

AWS	American Welding Society
CT	Compact Tension specimen
EDX	Energy Dispersive X-ray
EPFM	Elastic-Plastic Fracture Mechanics
FCAW	Flux-Cored Arc Welding process
LEFM	Linear-Elastic Fracture Mechanics
LPD	Load-Point Displacement
LWSS	Locally Weighted Scatterplot Smoothing
MVC	Micro-Void Coalescence
SEM	Scanning Electron Microscopy
TRIP	Transformation-Induced Plasticity
XRD	X-Ray Diffraction

3.1 Introduction

Due to the good resistance against corrosion and cavitation erosion, as well as the high mechanical properties of 13% Cr-4% Ni martensitic stainless steels, these steels are widely used to manufacture hydroelectric runners [2, 4, 5, 12, 86]. The manufacturing and repairing of the turbine runners are usually made by Flux-Cored Arc Welding (FCAW) process due to the high quality of the resultant weld metal. However, high contents of inclusions are found in the resulting microstructure as a result of deoxidizing elements added to the flux material. These inclusions being stress concentrators can initiate rupture at high stress locations [7, 37], and play a critical role on the onset of crack propagation. Therefore, the resistance against crack initiation is a matter of concern for these welded turbine runners.

The resistance against catastrophic crack initiation from a pre-existing defect can be described by Linear-Elastic Fracture Mechanics (LEFM) if the plastic zone produced at the crack tip remains small enough compared to sample dimensions (small-scale yielding condition). In this condition, rupture is described uniquely by the "stress intensity factor" K for an elastic singularity [7]. In plane strain condition, a K_{Ic} value can be considered as a material property as it is size-independent; however, small-scale yielding conditions requires large samples and testing equipment of large capacity for tough materials, i.e., materials resulting in large-scale yielding condition. For example, K_{Ic} testing of the cast version of 13% Cr-4 % Ni martensitic stainless steels requires a 500 mm thick sample and 10 MN tensile equipment [60]. Therefore, the resistance against crack initiation of such materials can be determined using small samples only using the J integral method which is valid even if the plastic zone is extended [7]. Similar to K in LEFM, J characterizes the crack tip stress conditions in Elastic-Plastic Fracture Mechanics (EPFM) [40, 41]. The critical value of J at the onset of stable crack growth is called fracture toughness J_{Ic} when plane strain conditions are obtained. These conditions can be satisfied using much smaller sample in EPFM. The J_{Ic} value can also be considered as a material property similar to the fracture toughness K_{Ic} in LEFM [7, 8].

The microstructure of these alloys can be quite complicated. The liquid solidifies as delta ferrite and transforms into austenite, then into martensite under most industrial cooling conditions. Because of the very low carbon content in these alloys, the as-quenched microstructure consists of soft martensite [2]. Despite the addition of Ni, some delta ferrite traces can still be found in the microstructure of these alloys as the result of regions enriched in Cr forming at grain boundaries at the final stage of solidification [2, 27]. On the other hand, austenite can be generated between martensite laths after proper tempering at intermediate temperatures [5, 12, 13, 87]. In the case of low tempering temperatures (typically bellow 610 °C), the reformed austenite is stable even at cryogenic temperatures, whereas austenite formed at higher tempering temperatures will retransform into fresh martensite during cooling [2, 12]. One of the most important advantages of reformed austenite is the possibility to have TRansformation-Induced Plasticity (TRIP) during loading, increasing the ductility and toughness of the produced alloys [14, 15]. In tension testing, the increase in the ductility is due to the enhanced strain hardening thanks to TRIP. The TRIP also plays a role during crack propagation as the crack tip fracture energy is absorbed by this transformation, resulting in an increase in fracture toughness [15]. The formation of martensite is associated with compressive stresses as the specific volume of austenite is about 3% lower than that of martensite, contributing in higher crack propagation resistance [15].

In the case of ductile rupture, inclusion characteristics play a major role during the nucleation, growth, and coalescence stages of the cracks that lead to material rupture. The stress triaxiality at the necking region or at the crack tip provides the conditions required for nucleation and growth of micro-voids. Micro-voids initiate from the regions with the highest stress triaxiality ratios as the nature of the local stress facilitates matrix/defect debonding [7]. The nucleated micro-voids grow to sustain the imposed deformation, and their impingement results in the coalescence stage. Final rupture follows the coalescence stage as shear lips form at the surface if plane stress conditions prevail on the sample surface. Both ductility and fracture toughness are influenced by inclusion characteristics in the same manner; the only difference is that the crack coalescence takes place at the center in a tension sample, whereas it occurs at the crack tip in the case of fracture toughness J_{Ic}/K_{Ic} sample [7]. It was established that the higher is the inclusion density, the more micro-void nucleation sites can be activated, and the coalescence occurs without excessive growth [64]. Indeed, smaller inclusion spacing results in a premature impingement of the nucleated micro-voids before higher plastic deformations occur at the crack tip. By contrast, higher inclusion spacing (lower inclusion density) results in the need for significant micro-void growth, and the Micro-Void Coalescence (MVC) mechanism controls the rupture process [61]. As the major part of the fracture energy is absorbed during the growth of micro-voids, higher inclusion spacing results in higher fracture toughness [63-65]. The inclusion size influences the required stress/strain for initiating micro-voids with an inverse relationship [64-66]. If the influences of the content, density, size, and spacing of inclusions have been well reported and established in the literature, the effect of the surrounding matrix is less documented.

More specifically, the fracture behavior of cast and wrought versions of 13% Cr-4% Ni martensitic stainless steels have been examined during tension, J_{Ic}, and Charpy impact tests in a previous work [60], showing that the smaller inclusion size of the wrought version of the alloy was the main reason for its superior mechanical properties. A ductile fracture model was also used to determine the fracture micromechanical processes involved in tension testing of these materials with the addition of weld versions of these materials [88]. However, based on the authors' knowledge, the effect of low temperature intercritical heat-treatment on fracture behavior of the weld metal of this category of stainless steels has not been examined to date during J_{Ic} stable crack growth. In the present study, both as-welded and heat-treated conditions of this category of stainless steels were produced using FCAW process and J_{Ic}-stable crack growth tests were run. Fracture behaviors were examined during tension and fracture toughness J_{Ic} tests, and the effect of heat-treatment (leading to the presence of metastable reformed austenite) and inclusions were investigated. The J-Resistance (J-R) curves were precisely developed and discussed. The microstructures were examined, the inclusion characteristics and the austenite contents were measured, and the fracture surfaces were studied.

3.2 Materials and experimental procedures

3.2.1 Materials

A weld metal block of the dimensions of 450 × 250 × 60 mm of 13% Cr-4% Ni martensitic stainless steels was deposited using a semi-automatic flux-cored arc welding (FCAW) process on a 450 × 250 × 50 mm steel substrate of similar composition (CA6NM), as shown in Figure 3-1. AWS E410NiMo filler metal was used and the welding process was performed in flat position. The welding parameters are given in Table 3-1. Slag removal was performed after each new welding pass, and a time interval of about 10 minutes between passes was considered to keep an inter-pass temperature of 200 °C. The welded block was separated from substrate, and the weld beads at the weld/substrate interface were removed. The produced material was tested in both as-welded and heat-treated conditions. The heat treatment was performed at 600 °C for 2 hrs in order to generate a significant amount of reformed austenite. In this paper, the terms 410NiMo-AW, and 410NiMo-HT are used to refer the weld metal in as-welded and heat-treated conditions, respectively.

The chemical composition of the weld metal is provided in Table 3-2. Measurements were carried out by plasma-emission atomic spectrometry (C and S were measured by combustion, and N and O were measured by inert gas fusion). The composition requirements according to AWS A5.22/A5.22M [89] are also added to Table 3-2 for comparison. All the values are verified by standard requirements; however, a considerable amount of nitrogen is found (49 ppm), suggesting that the welding pool hadn't been protected enough from the air by shielding gases. Furthermore, the oxygen content of the deposited material is very high (720 ppm), and can be found in inclusions found in the microstructure of the welded material. O can be generated by the decomposition of carbon dioxide or metallic oxides in the flux material and those in the slag [21]. Aluminum, silicon, titanium, and zirconium had been added to the flux material in order to form oxides and nitrides, reducing the oxygen and nitrogen content of the liquid [21]. That is why high amounts of oxides (non-metallic inclusions) are systematically found into the microstructure of the weld metal.

3.2.2 Microstructural characterization

The weld metal was examined before etching by an optical microscope and after etching using a laser confocal microscope (LEXT OLS4100) to analyze the inclusion characteristics and the microstructure of the weld metal, respectively. To this purpose, samples were ground and polished to a mirror appearance using sand papers and diamond suspensions. The mirror-polished samples were also examined using SEM and EDX to detect also the nature of inclusions. Both as-welded and heat-treated materials were etched using modified Fry's solution (150 mL distilled water + 1 g $CuCl_2$ + 50 mL HCl + 50 mL HNO_3) [5].

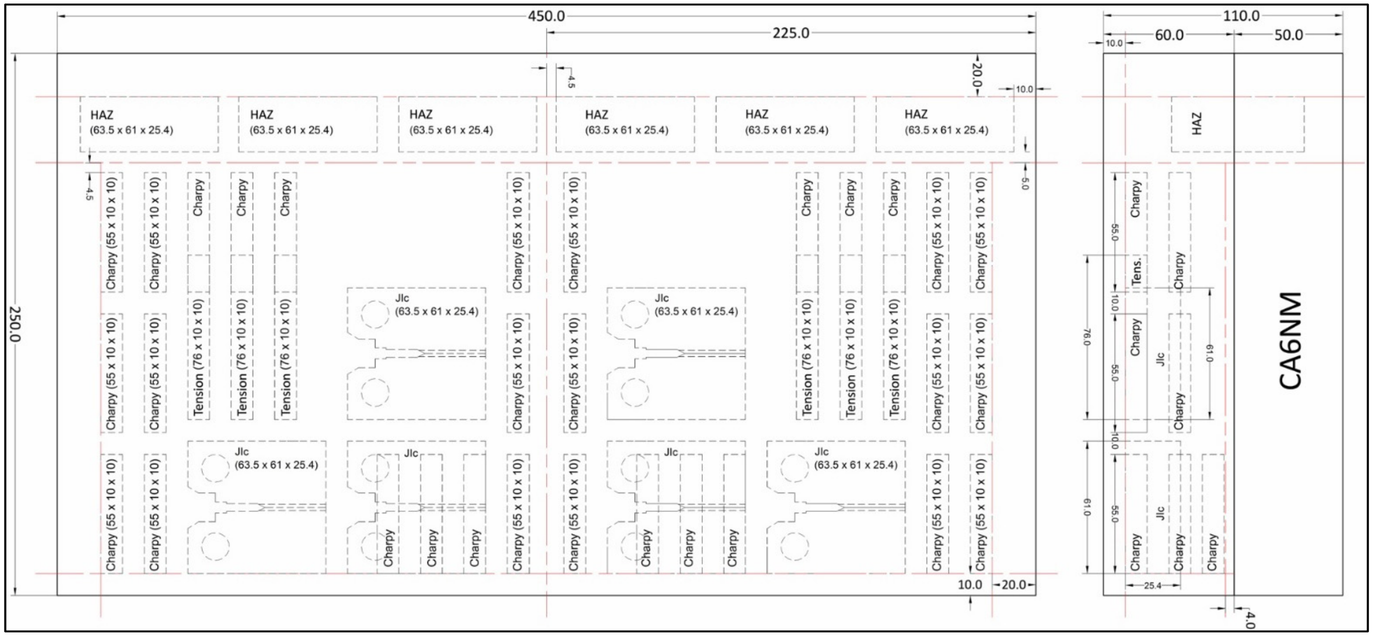

Figure 3-1 Sampling plan of the deposited material with its side view on the right; note: all dimensions are in millimeters. Three tension and J_{Ic} samples were collected for testing in each of the as-welded and heat-treated conditions. Results obtained from the small blocks determined for Charpy tests and examination of the HAZ are out-of-scope of this study and will be reported later.

Table 3-1 FCAW process parameters used in this study.

Pre-heat temperature (°C)	Inter-pass temperature (°C)	Current (A)	Voltage (V)	Torch speed (mm/s)	Deposition rate (g/s)	Heat input (J/mm)	Protection gas
180	200	218	22.5	4.5	1.125	1090	25% CO_2 + 75% Ar

Table 3-2 Chemical compositions of the studied materials (wt%).

Designation	Cr	Ni	C	Si	Mn	Mo	S	P	N	O
410NiMo steel	12.1	4.67	0.027	0.48	0.04	0.61	0.0093	0.01	0.0049	0.072
AWS (A5.22/ A5.22M)	11.0-12.5	4.0-5.0	0.06 (max)	1.0 (max)	1.0 (max)	0.4-0.7	0.03 (max)	0.04 (max)	-	-

Due to the small size of inclusions, a relatively high magnification of 500X was used. Five optical micrographs were chosen over the polished surface and surface density (N_A), volume fraction (V_v), diameter (D), and spacing (S) of inclusions were calculated using the automatic image analyzing software ImageJ. The micrographs were transformed into binary mode composing of only black and white pixels, while keeping the high resolution of each image, to perform automatic measurements with the best accuracy level. The black pixels represent inclusions, and the matrix is shown in white pixels. The number and the area of the black spots (inclusions) are then measured automatically for each micrograph; the inclusion number per image area (μm^2) considered as the surface density, the ratio of the black to white pixels calculated as the area fraction of inclusions, and the equivalent circle diameter of each inclusion was calculated to represent the inclusion diameter D. A total surface of 0.15 mm^2 was analyzed, and at least 2000 inclusions were examined. The inclusion surface density (N_A) was then calculated for a square centimeter, and the area fraction of inclusions was considered as the volume fraction as defined in ASM Handbook [78]. For the inclusion spacing S, the relationship $S=0.89D_0(V_v)^{-1/3}$ provided in [16] was used, where $D_0=(\pi/4)H(D)$, and H(D) is the harmonic mean of the inclusion diameter D.

Quantitative X-ray diffraction (XRD) by Rietveld method [81] was used to measure the austenite contents of both as-welded and heat-treated materials. Three samples were examined for each of the metallurgical conditions using a Bruker D8 Advance diffractometer equipped with a copper X-ray source and a nickel filter. Diffraction patterns were obtained in the range 40° < 2θ < 140° with a step size of 0.05° and austenite intensity peaks diffracted from (111), (200), (220), (311), (222), and (331) crystallographic planes were analyzed as detailed in [5]. An automatic cut-off machine was used to cut the samples from the weld, using 0.5 mm thick saw blades and a cut speed of 0.05 mm/s to minimize the possible risk of austenite transformation during cutting process. Samples were polished with 1200 grit sand papers, then etched in a 40% H_2O + 30% HNO_3 + 30% HCl solution and in HCl for 10 minutes and 30 seconds, respectively, in order to remove any oxide film.

3.2.3 Mechanical characterization

3.2.3.1 Tension tests

Round bar specimens with a diameter of 5 mm were used for tension tests. Three tests were performed per condition (as-welded and heat-treated) in accordance with ASTM E8/E8M [79] at room temperature using a strain rate of 2.5×10^{-4} s^{-1}. The true strain ε and the true stress σ were calculated using $\varepsilon=\ln(1+e)$ and $\sigma=S(1+e)$, where e and S are the engineering strain and engineering stress, respectively [76]. The coefficients of strain hardening n as defined with the Ludwik-Hollomon equation $\sigma=K\varepsilon^n$, where K is a constant, were calculated [38]. However, as the material behavior cannot be described with a constant n value (the ln(ε) versus ln(σ) is not linear), the strain hardening coefficient is calculated continuously from the yielding point up to the maximum load [57, 90, 91]. Practically, the strain hardened parts of the σ-ε curves were smoothed by the Locally Weighted Scatterplot Smoothing (LWSS) method using suitable polynomial functions, and instantaneous strain hardening coefficients n_i were calculated in accordance with [91]:

$$n_i(\varepsilon)=\frac{d\ln\sigma}{d\ln\varepsilon}=\frac{\varepsilon}{\sigma}\frac{d\sigma}{d\varepsilon}=\frac{\varepsilon_i(\sigma_{i+1}-\sigma_{i-1})}{\sigma_i(\varepsilon_{i+1}-\varepsilon_{i-1})} \tag{3.1}$$

These calculated n_i values were then traced versus true strains for both as-welded and heat-treated materials.

3.2.3.2 Fracture toughness J_{Ic} tests

Three fracture toughness J_{Ic} tests were performed for each condition (as-welded and heat-treated) using the single specimen test method in accordance with the guidelines described in ASTM E1820 [92]. Compact tension (CT) specimens with a thickness of 25.4 mm, and a width of 50.8 mm were used. In order to have a more uniform plane strain condition along the crack front, side-grooves corresponding to a depth of 10% of the whole thickness were machined on each side of the specimens. This prevents plane stress conditions at the sample surface and the formation of shear lips. Machining the side grooves were performed before fatigue pre-cracking to produce a straighter fatigue-crack, to remove the step_between the fatigue-crack and ductile tearing planes during J_{Ic} testing, and to decrease the sample preparation time as proposed in [93]. Accordingly, the length of the fatigue-crack was measured by elastic compliance instead of using optical microscopes [94]. Fatigue pre-cracking was performed at a constant value of ΔK of 12 MPa$\sqrt{m}$ with a stress ratio of 0.1, and a loading frequency of 20 Hz was used for both as-welded and heat-treated conditions up to an initial crack length/width (a_0/W) ratio of 0.55 (equivalent to an initial crack length of 28 mm for the CT samples used in this study).

Clip-on gages were used to record the total displacement. Elastic unloadings of 10% of the actual maximum load were used to predict the crack size by compliance. To minimize the risk of unstable crack propagation, the unloading sequences were started at a low enough "load point displacement (LPD) start point" found to be 0.2 mm, and 0.4 mm in the case of as-welded and heat-treated materials, respectively. To develop the J-R curve with a sufficient number of points, LPD increments equal to 0.03 mm, and 0.05 mm were used for the as-welded and heat-treated materials, respectively. With these conditions, about 10 loading/unloading sequences were performed to obtain the J-R curves for each of the as-welded and heat-treated conditions.

An effective crack length is defined by considering the crack tip plastic zone radius as a part of the actual crack size [37]. By considering the Crack tip Opening Displacement (COD) using the strip-yield model of Dugdale [95] and Barenblatt [96] and estimating that crack blunting occurs by the formation of a circular plastic zone at the crack tip (as proposed by Irwin [7]), the effective crack length can be defined as equivalent to half of the plastic zone size plus the initial crack size. This value is used to define the "blunting line" which is used to calculate the J value from the obtained sigma value:

$$J = 2\sigma_I \Delta a \tag{3.2}$$

where:

$$\sigma_I = \frac{\sigma_y + \sigma_{UTS}}{2} \tag{3.3}$$

and σ_y , and σ_{UTS} are respectively the yield and the ultimate strengths. Two lines parallel to the blunting line, called "exclusion lines" were drawn at 0.15 mm and 1.5 mm in order to collect the data points located in the J-dominated zone. The data points intercepted between these exclusion lines were fitted to a power law relationship:

$$J = C_1 \Delta a^{C_2} \tag{3.4}$$

to generate the J-R curve. From the intersection of 0.2 mm offset line and the J-R curve a candidate value of fracture toughness, J_Q, was obtained.

The crack fronts were marked using heat tinting and fatigue cycling process in order to verify all ASTM E1820 requirements. The heat tinting was performed at 450 °C for 2 hrs and the fatigue cycling process was run at 20 Hz with a constant ΔK value of 33 MPa√m and a stress ratio of 0.3. The crack front straightness was verified for both fatigue pre-cracking and J_{Ic}-crack extension fronts at 9 equally spaced points in accordance with ASTM E1820. These fracture toughness J_{Ic} values were transformed into the fracture toughness K_{Ic} values using the following equation [7, 8]:

$$J_{Ic} = (1-\nu^2)\frac{K_{Ic}^2}{E} \tag{3.5}$$

where ν is Poisson ratio and E is Young's modulus.

In addition to the initiation fracture toughness J_{Ic} values, another criterion defining the entire shape of the J-R curve entitled "tearing modulus T" was also provided. This criterion was calculated using the following equation [7]:

$$T = \frac{E}{\sigma_y^2}\frac{dJ}{da} \tag{3.6}$$

where dJ/da is the slope of the J-R curve calculated using the part of the curve located between the exclusion lines.

3.2.4 Fractography

Fracture surfaces and in particular inclusions were examined using SEM and EDX. More than 80 spectrums obtained from inclusions of different sizes were examined, and it was revealed that all inclusions found in the weld metal are of the same nature. Except several large inclusions, almost all inclusions were of very small size; however, as larger particles provide clearer images/EDX maps, the ones of the largest particles were shown in this study. The measurements of inclusion diameter were compared between the fracture surfaces of tension and fracture toughness J_{Ic} tests for both as-welded and heat-treated conditions. Automatic measurements were not possible in this case, and measurements were carried out manually. In order to achieve a high level of accuracy, a high-level magnification of 2000X was used and more than 100 inclusions were considered for each condition.

3.3 Results

3.3.1 Microstructure

The inclusion characteristics in the microstructure of the weld metal are shown in Table 3-3. The surface density and the volume fraction of inclusions are relatively high which are typical of welded microstructures exposed to oxygen. Large numbers of small non-metallic inclusions are found. These very fine inclusions having a diameter D less than one micrometer were homogeneously dispersed in the microstructure of the weld metal, resulting in a very small inclusion spacing S of about two micrometers. As also shown in the previous study [88], inclusions are normally distributed, and the arithmetic mean of all inclusions is a good parameter representing the inclusion size. 81% of inclusions were smaller than 1 µm in diameter, more than 17% of them have diameters between 1 µm and 2 µm, and only lower than

2% of all measured inclusions were larger than 2 μm. It is expected that these inclusion characteristics will affect the mechanical properties of the weld metal.

Table 3-3 Inclusion characteristics in the microstructure of the weld metal.

Designation	N_A (No./cm^2)	V_v (%)	D (μm)	S (μm)
410NiMo	$(1.29 \pm 0.25) \times 10^6$	1.10 ± 0.14	0.76 ± 0.02	1.89 ± 0.10

N_A, surface density; V_v, volume fraction; D, mean diameter; S, average spacing.

The microstructures of the weld metal are revealed using optical microscopy for both as-welded and heat-treated conditions in Figures 3.2 (a) to (c). The martensitic microstructure seen in these micrographs is of the lath type, but the microstructure of the tempered martensite shown in Figure 3-2 (b) displays a stronger contrast than in the as-welded condition. Both microstructures displayed in Figures 3.2 (a) and (b) are so fine that only the packets of the lath martensite can be seen. However, the martensite blocks can be detected at the much higher magnification shown in Figure 3-2 (c), while the individual laths located within these blocks cannot still be revealed. Very fine inclusions in black are closely dispersed in the microstructure. Some amounts of austenite exist in the microstructure, but higher magnifications are needed for this phase to be observed [5]. The austenite contents as measured by the diffraction technique are reported in Table 3-4, showing that the amount of austenite in the tempered martensite reaches 10%.

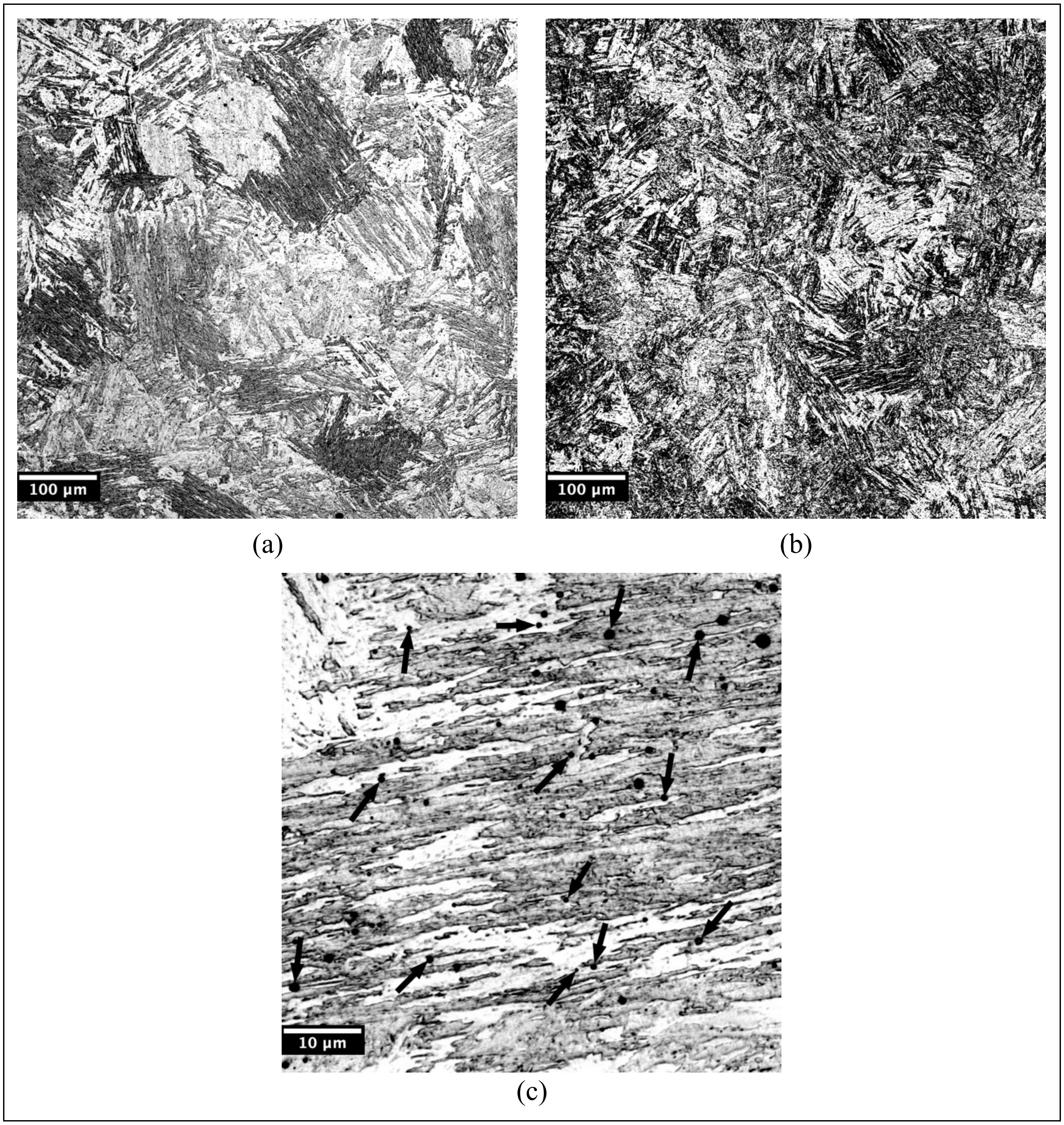

(a) (b) (c)

Figure 3-2 Microstructure of the weld metal examined using laser confocal microscopy: (a) as-welded condition, (b) heat-treated condition, and (c) martensite blocs observed in the as-welded condition at a 10 times higher magnification. Some fine inclusions in black are shown by the black arrows in (c).

Table 3-4 Austenite contents of the weld metal in as-welded and heat-treated conditions. The standard deviations were calculated (results obtained from the three measurements).

Designation	Austenite (%)
410NiMo-AW	2.4 ± 1.0
410NiMo-HT	10.0 ± 0.6

3.3.2 Tension properties

Tension curves of as-welded and heat-treated materials are shown in Figure 3-3. The tension properties of the weld metal are provided in Table 3-5 together with the standard requirements. The ultimate strength is higher than the minimum value proposed in the standard for both conditions. However, this is only the elongation at fracture of the heat-treated material that substantiated the minimum standard requirement at 15%. The as-welded material is more resistant compared to the heat-treated one, but necking happens early (at 4% compares to 7%) and it is less ductile than the heat-treated condition. As shown in Table 3-5, the ductility is significantly improved by the proposed heat treatment while high values of yield and tensile strengths are kept (Table 3-5). Both uniform elongation at necking (e_u) and elongation occurred after necking (i.e., e_u minus e_f) are improved by about 55% and 12%, respectively. These increases in the elongation of the heat-treated material is due to the sustained strain hardening in the homogeneous deformation part of the curve.

Plots of the instantaneous strain-hardening coefficient n_i against true strain ε are shown in Figure 3-4. In the case of as-welded material, the n_i value decreased continuously until it reaches a value close to the instability criterion for the onset of necking (n_i=ε_u) for which the value is around 0.04 [37]. By contrast, a symmetrical bell-shaped curve was obtained in the case of heat-treated material with a maximum of 0.10 achieved at a strain of 0.037, similar to the necking condition in the as-welded condition. For the heat-treated condition, the onset of necking corresponds also to the condition for which the instantaneous strain hardening is about the actual strain level undergone by the material (0.072 versus 0.066, respectively). These n_i-ε curves show that the low temperature intercritical heat-treatment delayed the onset of necking by increasing the strain hardening until higher strains are reached. In addition, the speed of decrease in the instantaneous strain hardening n_i is also reduced to half in the heat-treated material (from 2.0 to 1.1) as illustrated by the two linear behaviors in Figure 3-4.

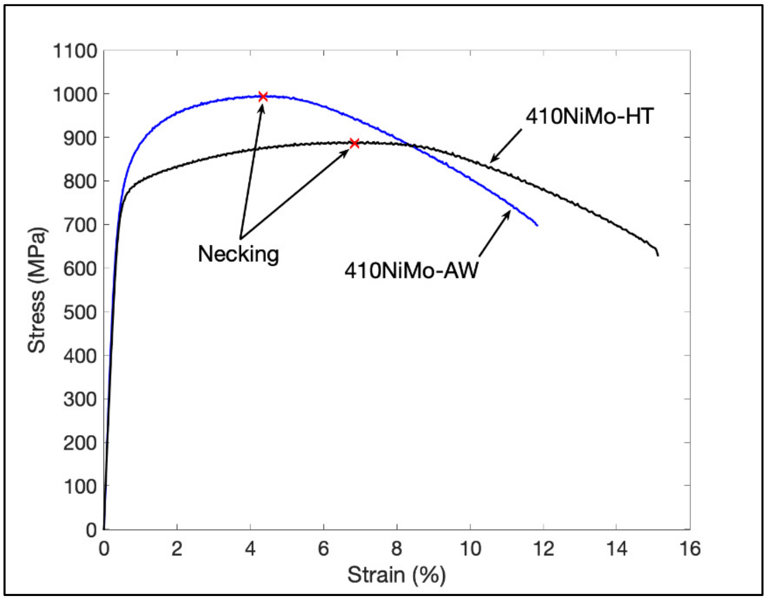

Figure 3-3 Tension curves of the weld metals.

Table 3-5 Tension properties of the weld metals.

Designation	0.2% σ_y (MPa)	σ_{UTS} (MPa)	e_u[1] (%)	e_f[2] (%)
410NiMo-AW	783 ± 5.8	1007 ± 10.3	4.4 ± 0.1	11.9 ± 0.2
410NiMo-HT	765 ± 5	895 ± 4	6.8 ± 0.3	15.2 ± 0.4
AWS A5.22/A5.22M (min)	-	760	-	15

[1]-Uniform elongation at necking. [2]-Elongation at fracture.

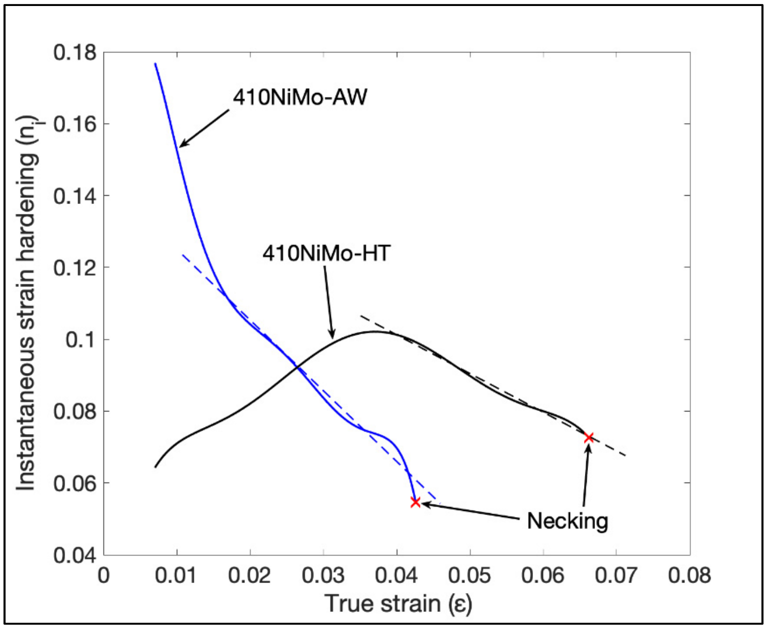

Figure 3-4 Instantaneous strain hardening coefficient with respect to true strain for the as-welded and heat-treated materials. The crosses and arrows indicate the strain at which necking take place. The two lines quantify the speed at which the strain hardening coefficients decrease before necking.

3.3.3 Fracture toughness properties

The J-R curves together with the J_Q values and their equivalent K_Q ones are shown in Figure 3-5, and Table 3-6, respectively. Blunting lines and the exclusion lines were added for convenience. As the slope of the construction lines are close between the as-welded and heat-treated conditions, the exclusion and offset lines cannot be differentiated in the graph conditions.

Ductile instability occurred for the first J_{Ic} test performed on the as-welded material (AW-1) because the first defined LPD start point (0.4 mm) was too high. As a consequence, it was not possible to draw a J-R curve due to the lack of valid points. The relatively low fracture toughness of the as-welded material resulted in a low stability of J_{Ic}-crack, justifying the selection of lower “LPD start point” and “LPD increment” for stable crack growth to be documented. The LPD start point and increment values were decreased to 0.2 mm and 0.03

mm, respectively, resulting in valid results (AW-2 and AW-3). Hence, two J-R curves were developed for this condition and 5 data points were intercepted between the exclusion lines. The resultant J-R curves substantiate the ASTM-standard requirement as at least five data points shall be intercepted between the exclusion lines [92]. The other standard requirements were also satisfied, and the J_Q values were qualified as J_{Ic} ones. As provided in Table 3-6 the fracture toughness values and the tearing modulus T are similar, showing that the tests are reproducible. As can be seen in Figure 3-5, the J values located beyond the 1.5 mm exclusion line cannot be described by the J-R curve: They are much lower than the predicted values, showing that a stable crack growth regime took place and that a constant crack driving force is needed for these conditions.

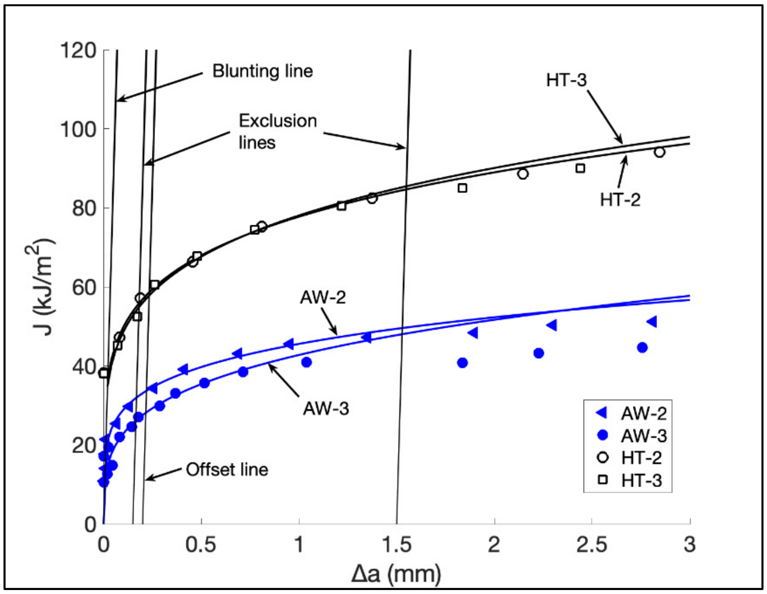

Figure 3-5 J-R curves obtained for the as-welded and heat-treated materials. The blunting line, and the exclusion lines were added for convenience.

Table 3-6 Fracture toughness J_{Ic} and the equivalent K_{Ic} values obtained in this study.

Material	Test	dJ/da (MPa)	T	J_Q (kJ/m^2)	K_Q (MPa$\sqrt{m}$)
410NiMo-AW[a]	AW-2	11	4	34	86
	AW-3	16	5	28	79
410NiMo-HT	HT-2	20	7	59	114
	HT-3	21	7	59	114

[a]- The first test (sample AW-1) qualified as rejected since unstable ductile instability occurred at the first loading/unloading sequence.

Stable crack growth occurred for the initially set LPD parameters in the case of heat-treated material revealing a much higher crack driving force. However, only three data points were intercepted between the exclusion lines (HT-1), resulting in a non-valid test according to the ASTM standard and an overestimated slope for the resultant J-R curve. The results of this first attempt were also ignored and only the J-R curves of HT-2 and HT-3 samples were shown in Figure 3-5. Stable J_{Ic}-crack growth occurred for samples HT-2, and HT-3 as shown in Figure 3-5 and four points were intercepted between the exclusion lines in each case. In fact, one data point is tangent to the 0.15 mm exclusion line in the case of HT-3, and five intercepted data points can be considered in this case. On the other hand, all the other ASTM-standard requirements have been satisfied for each of the heat-treated samples. Contrary to the as-welded material, the data points beyond the 1.5 mm exclusion line can be described by the estimated J-R curves. For these conditions, the size of the plastic zone at the J_{Ic}-crack tip keeps increasing as crack extends and higher crack driving forces (J values) are needed to grow the crack further. A condition for stable crack growth is then obtained in the heat-treated material and a large-scale yielding is taking place ahead of the crack. In fact, the major part of the stored energy in the material results in the plastic zone formation ahead the J_{Ic}-crack [7]. The J-R curves are nearly identical in the case of the samples HT-2 and HT-3, resulting in equal J_Q values. The J_Q values of the HT-2 and HT-3 curves can then be considered as the initiation fracture toughness J_{Ic} of the heat-treated material.

The plane strain fracture toughness properties and yield strengths of the weld metals are provided in Table 3-7. All provided toughness properties are higher in the case of the heat-treated material. Not only the mean value of fracture toughness J_{Ic} is increased by 90%, but also the slope of the J-R curve (dJ/da) is increased by about 50%, improving the resistance against crack growth significantly. As a result, the tearing modulus is increased too by 75%. The equivalent fracture toughness K_{Ic} values were also calculated in Table 3-7, showing that the K_{Ic} value of the heat-treated material is about 40% higher. It means that under plane strain conditions unstable crack propagation occurs for a crack length half smaller in the as-welded material.

Table 3-7 Plane strain fracture toughness values and the tension strengths of the weld metals.

Material	0.2% σ_y (MPa)	J_{Ic} (kJ/m^2)	dJ/da (MPa)	T	K_{Ic} (MPa$\sqrt{m}$)
410NiMo-AW	783	31	14	4	82
410NiMo-HT[a]	765	59	21	7	114

[a]-In the case of fracture toughness properties of the heat-treated material only the results of the samples HT-2 and HT-3 were considered.

3.3.4 Fractographic examinations

Typical fracture surfaces of the tension and J_{Ic} tests are shown in Figure 3-6. Fracture occurred by dimpled rupture in both as-welded and heat-treated conditions, and the micrographs have similar fracture appearances. Inclusion/matrix interface decohesion is the dominant mechanism for micro-void nucleation and almost all inclusions found on the fracture surfaces were intact i.e., not broken.

Table 3-8 provides the inclusion diameters measured on the fracture surfaces. The inclusion size is approximately equal for all the test conditions and are very similar than the ones measured on metallographic sections (Table 3-3 vs. Table 3-8), meaning that all inclusions have nearly the same chance to initiate micro-voids under tension or J_{Ic} tests for both as-welded and heat-treated materials. Due to the very large number of inclusions and small inter-particle spacing in the microstructure (Table 3-3), very small dimples were formed and smooth fracture surfaces were obtained. The J_{Ic} fracture surfaces are actually smoother than the tension ones as the stress triaxiality ratio S_T is uniform all over J_{Ic} fracture surfaces ($S_T \approx 2$ [7]), whereas it differs significantly from the surface into the center of the necked region in the tension sample where it reaches the maximum value ($S_T < 1$ as reported in [88]).

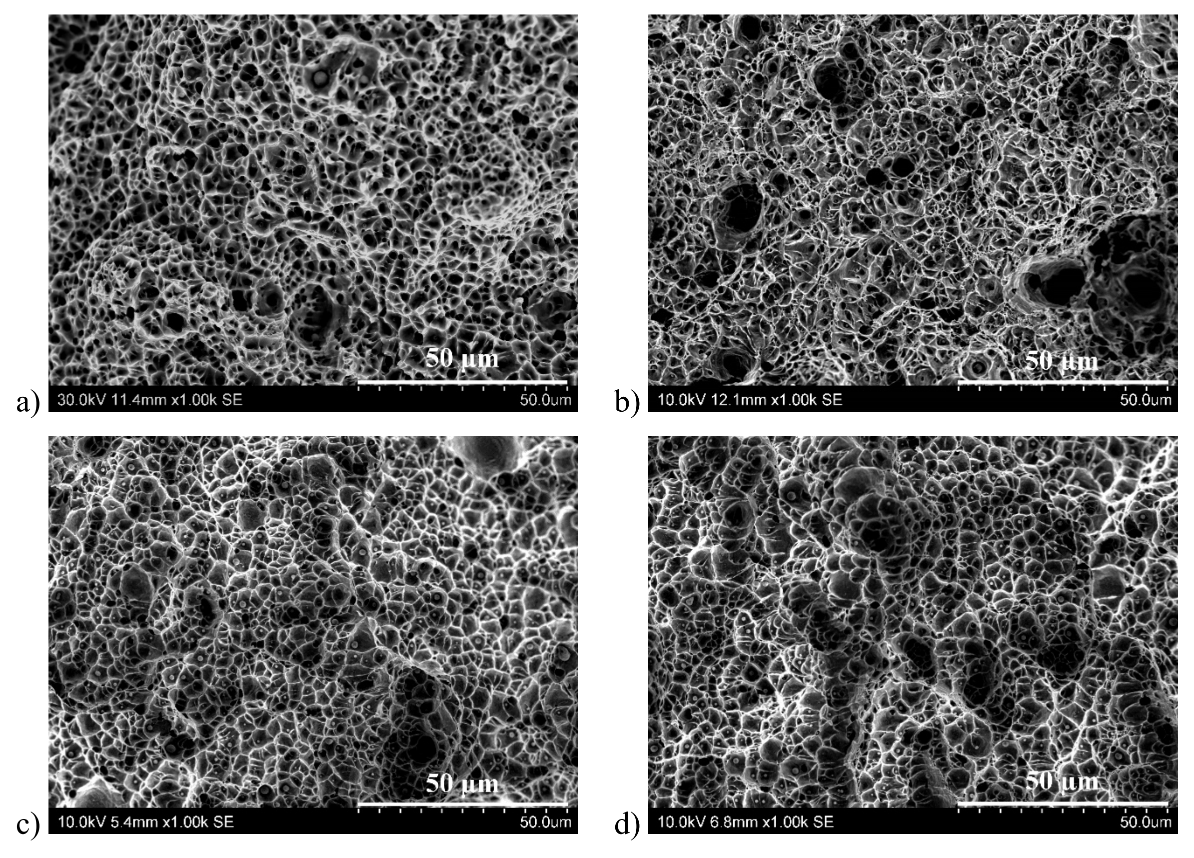

Figure 3-6 Fracture surfaces of the tension and J_{Ic} tests of the as-welded (a, c), and heat-treated (b, d) materials, respectively, showing similar ductile fracture characteristics

Table 3-8 Inclusion size measured on tension and J_{Ic} fracture surfaces.

Material	Test	Number of measured inclusions	Size (mean diameter, µm)
410NiMo-AW	Tension	35	0.86 ± 0.48
	J_{Ic}	35	0.84 ± 0.27
410NiMo-HT	Tension	35	0.86 ± 0.29
	J_{Ic}	35	0.88 ± 0.37

Inclusions found on the J_{Ic} fracture surface of the heat-treated material were analyzed using EDX chemical spectrum and revealed that it is composed of different oxides (Figure 3-7). An inclusion cut into two parts during metallographic sample preparation in Figure 3-8 reveals the complex nature of the inclusion (O, Al, Cr, Si, Ti, Zr, and Mn elements were detected but the chromium and manganese are most likely coming from the matrix).

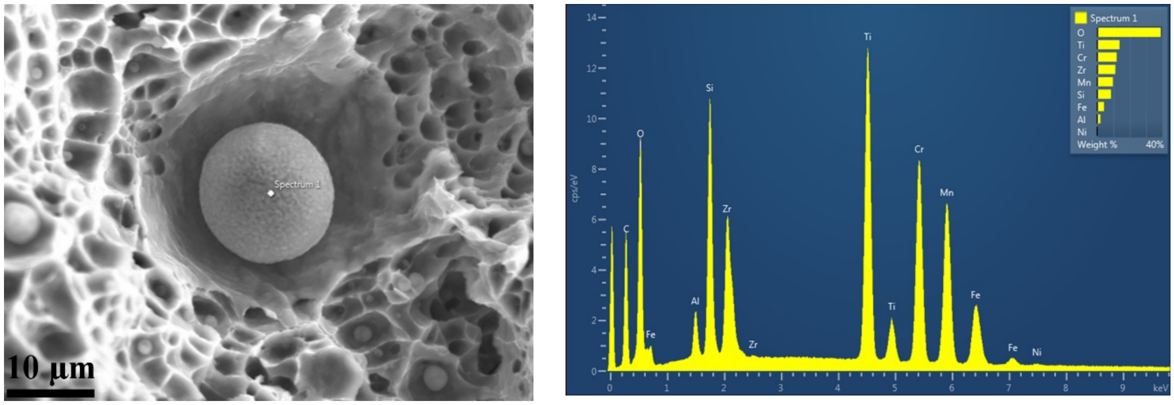

Figure 3-7 A complex inclusion observed on the J_{Ic} fracture surface of the heat-treated material with its EDX spectrum at the right, showing that it composed of several components.

3.4 Discussion

As shown in Table 3-7, heat treatment has increased significantly the fracture toughness J_{Ic} and tearing modulus T by 90% and 75%, respectively. The higher fracture toughness J_{Ic} is a result of a larger crack tip plastic zone at the onset of stable crack growth [7]. The higher tearing modulus T documents the fact that the crack tip plastic zone increased in size during stable crack growth, requesting much higher crack driving forces for stable crack extension to be occurring.

The size of the crack tip plastic zone r_y in the as-welded and heat-treated can be estimated from the Irwin formulation ($r_y=(1/3\pi)x(K_{Ic}/\sigma_y)^2$) [7, 8]. It is about 1 mm and 2.5 mm for the as-welded and heat-treated materials, respectively. In the case of as-welded material, constant J values beyond the 1.5 mm exclusion line show that the small crack tip plastic zone was not increased in size, suggesting that the small-scale yielding condition is satisfied [7, 37]. Consequently, a K_{Ic} test procedure could have been used for this material. In the case of the heat-treated material, the significant increase of the J values in the J-R curve shows that the

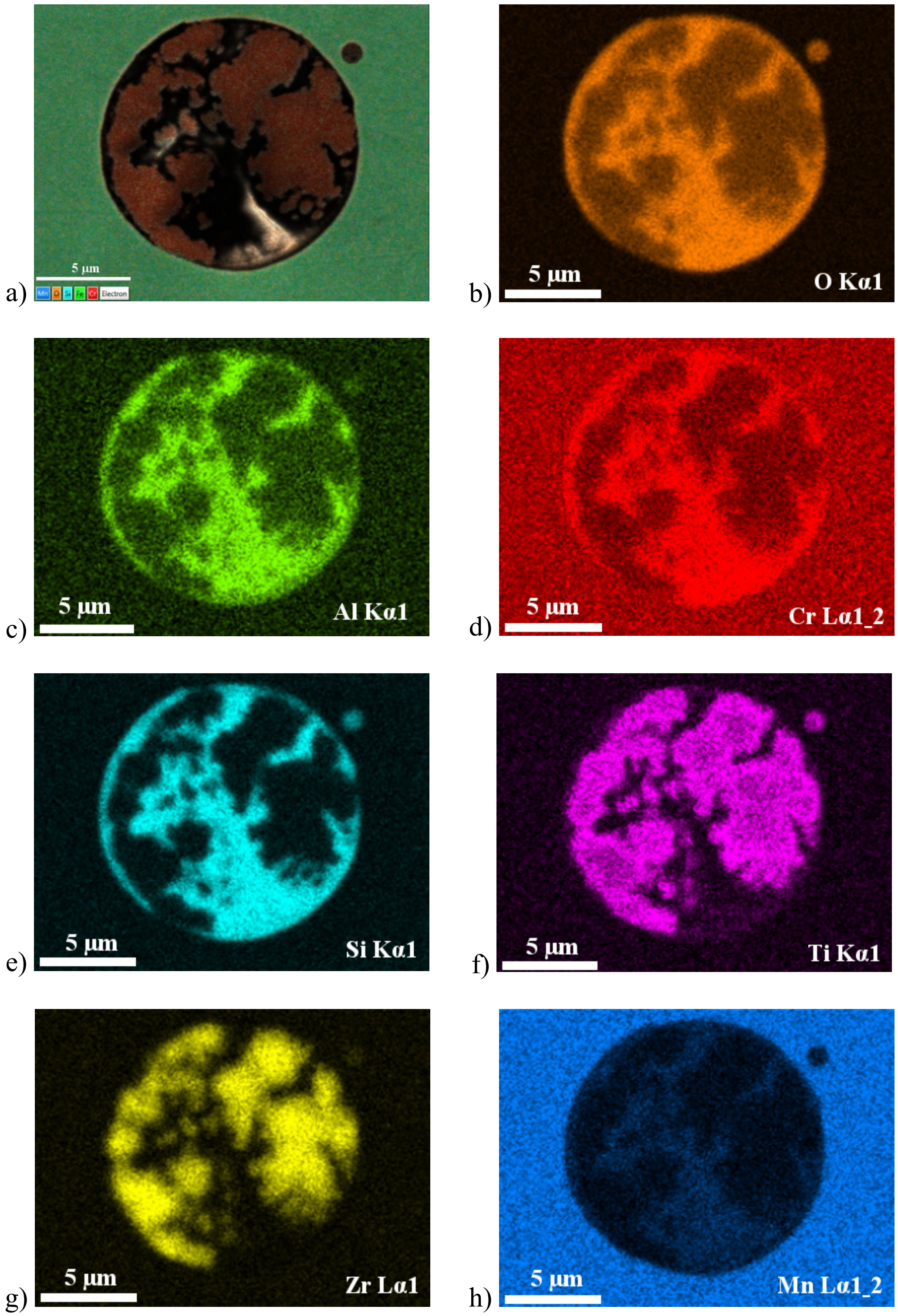

Figure 3-8 (a) EDX area analysis of a complex inclusion in the microstructure of weld metal followed by the X-ray mappings of (b) O, (c) Al, (d) Cr, (e) Si, (f) Ti, (g) Zr, and (h) Mn.

small-scale yielding approximation cannot be made, and hence much larger samples should be used for performing a K_{Ic} test directly.

In the case of as-welded material, the material is rather heterogeneous with regions having martensite at different level of tempering [73]. In the overall microstructure, a very high density of dislocations produced by the martensitic transformation (during weld metal solidification) [97] is present, preventing the generation of new dislocations at the onset of plasticity. As a consequence, a high instantaneous strain hardening is found (0.177). This exponent decreases as the deformation reorganizes the forest of dislocations [98, 99] and a saturation level is reached, allowing mechanical instability and necking to take place [100]. This condition happens when the uniform strain of the material reaches the instantaneous strain hardening value as expected by the model describing necking as an unstable mechanical instability [37].

The heat-treatment homogenizes the microstructure, reducing the global hardness of the material [14], and produces reformed austenite. The resulting work hardening at the onset of plasticity is significantly lower (1/3) than that of the as welded material, but instead of decreasing as strain increases, its value reaches a maximum at a strain equivalent to the necking strain in the as-welded condition (0.037 versus 0.043, respectively). The presence of a maximum instantaneous strain hardening reflects the concave shape of the material behavior on the stress strain curve (Figure 3-3). The speed at which the strain hardening decreases after the maximum is half the one reported for the as-welded material (compare dashed lines in Figure 3-4), improving further the ductility of the material.

The reasons for the significant improvement in the strain hardening after heat-treatment can be found in the enhanced ductility of the tempered martensitic matrix and the possibility for a TRIP effect introduced by the presence of reformed austenite. The density of dislocations in the tempered martensite is relatively low and their mobility rather high, resulting in a low initial strain hardening (controlled by self-hardening). Results found for pearlitic and/or bainitic materials showed that at the onset of plastic deformation the instantaneous strain hardening n_i progressively increases [91]. The formation of the geometrically necessary dislocations to accommodate plastic deformation between grain and phases was suggested as a possible mechanism for such increase in strain hardening at low strains [101]. The n_i reaches a maximum as a relatively high dislocation density is reached, reducing significantly the dislocation mobility [91]. The increase of the instantaneous strain hardening at low plastic strains will be further promoted thanks to TRIP, as the transformation of austenite into martensite generates additional dislocations which act as dislocation forest and contribute significantly to the increase in strain hardening [99, 102, 103]. The TRIP of austenite is known to consume a considerable part of plastic strain thanks to the volume change associated with the formation of martensite [15]. The maximum instantaneous strain hardening is typically reached when no more significant TRIP can happen and only dislocations can sustain further strain accumulation [57, 104]. From that point on, a behavior similar to the as-welded material is observed and the strain hardening decreases as the size of the dislocation cells reach a saturation level; however, the speed at which the strain hardening decreases is significantly lower (half the value) in the heat-treated material. The reasons for such behavior could be found in the fact that dislocation mobility in the heat-treated material may be significantly higher than that in the as-welded material, and the presence of islets of the newly transformed hard martensite that can pin locally the dislocations. This may result in the efficient further hardening effect even if no more TRIP is active in the material.

As the nature and distribution of inclusions are the same for both alloys, it is the behavior of the different phases present in the matrix that can explain the significant increase in fracture toughness by about a factor of 2. The more ductile tempered martensite in the heat-treated material produces a larger plastic zone ahead of the crack tip; thus, releasing the available energy in a larger volume. On the other hand, the TRIP effect retards the micro-void nucleation stage until higher deformations are reached due to the volume change associated with martensite transformation and the strain hardening effect. The generation of compressive stresses due to the formation of the martensite could also relax some of the crack tip stresses, preventing its propagation at greater distances. Furthermore, TRIP can also blunt the crack tip, as shown in [15]; which in turn deceases the local strain concentration and retards the localization of energy in the region ahead of the crack. A higher level of J_{Ic}-crack tip strain energy is therefore required to create the two new surfaces that will permit the crack to propagate further. All these micromechanical mechanisms result in the significant improvement of the J_{Ic} value; however, further optimization of the intercritical heat-treatment in terms of temperature, duration or weld composition could lead to even higher fracture toughness [13, 87]. In particular, the effect of the amounts, shape and stability of reformed austenite on the crack propagation resistance could be investigated. This will provide relevant information for industrial application as well as for academic research.

3.5 Conclusions

The beneficial effect of a heat-treatment at 600 °C for two hours on the fracture micromechanics of the 13% Cr-4% Ni martensitic stainless steels deposited by FCAW process was quantified using tension and fracture toughness J_{Ic} tests. The main conclusions are summarized as follows:

- Heat treating was an effective way to double the fracture toughness, reaching 59 kJ/m^2. Both, uniform elongation and elongation at fracture were increased by 55% and 28%, respectively, while decreasing the yield strength by only 2%.
- Ductile rupture occurred during tension and J_{Ic} testing of the weld metal for both as-welded and heat-treated materials.
- Similar micro-void characteristics were observed for all the tests in both as-welded and heat-treated conditions. Micro-voids formed in very large numbers in both cases, resulting in no significant void growth but a rapid coalescence of the nucleated micro-voids. Accordingly, the role of micro-void growth stage on the ductility and fracture toughness properties was limited by the proximity of the inclusions in the material.
- The inclusions present in the microstructure were very small with a size of less than one micrometer in diameter. These inclusions were complex oxides composed of Al, Cr, Si, Ti, and Zr, and were not affected by the heat treatment. Their density is so high and particles are basically 1.9 μm apart.
- The evolution of the instantaneous strain hardening n_i quantified the different behaviors between the as-welded and heat-treated materials: in the as-welded material the strain

hardening decreases from the onset of plastic deformation until necking, whereas it increases up to a maximum in the as-welded material. After reaching this maximum, the strain hardening decreases with half the speed it decreased in the as-welded condition. As a result, necking instability happens at 55% higher strain in the heat-treated material.

- The J-R curves and the J_{Ic} values determined for as-welded and heat-treated materials were significantly different. In the case of the as-welded material, the curves reached a plateau showing that J_{Ic}-crack growth occurred under an approximately constant crack driving force J. This has resulted in an unstable J_{Ic}-crack condition, suggesting that the fracture toughness of this material could have been measured directly by a K_{Ic} test. On the other hand, in the case of heat-treated material, J keeps increasing as crack grows. This put in evidence the higher crack propagation resistance of the heat-treated material due to its larger crack-tip plastic zone. As a consequence, the tearing modulus T increases by 75%.
- The softer tempered martensitic matrix and more importantly the occurrence of TRIP in the austenite are considered the major reasons for these mechanical property improvements. They retard the onset of mechanical instability by increasing the strain hardening as well as retarding void nucleation after necking.

Acknowledgements

Financial supports of Natural Sciences and Engineering Research Council of Canada (NSERC), Hydro-Québec, and Alstom Power Hydro are gratefully acknowledged. SEM-EDX, XRD and Rietveld analyses were performed at the Institut de Recherche d'Hydro-Québec (IREQ). The tension and J_{Ic} tests were performed at École Polytechnique de Montréal under supervision of Mr. Yves Verreman. The authors of this paper would like to thank Mr. Jianqiang Chen for his valuable contribution during J_{Ic} testing of the first sample of each of the base metals (CA6NM and 415) published previously. We would also like to thank Mr. Denis Thibault from IREQ for his support and Mr. Mathieu Paquin for the manufacture of the excellent quality weld metal block. The valuable experimental assistance of Mrs. Manon

Provencher, Mr. Étienne Dallaire, Mr. Alexandre Lapointe, technologists at IREQ, and Mrs. Josée Laviolette, technologist at École Polytechnique de Montréal are gratefully acknowledged.

Declaration of Competing Interest

The authors declare that they have no known competing financial interests or personal relationships that could have appeared to influence the work reported in this paper.

CHAPTER 4

ARTICLE 3: AN INVESTIGATION ON FRACTURE TOUGHNESS OF THE HAZ IN THE WELDED JOINTS OF 13% CR-4% NI MARTENSITIC STAINLESS STEELS

Fayaz Foroozmehr[1], Philippe Bocher[1]

[1]École de Technologie Supérieure (ÉTS), Montréal, Québec, Canada H3C 1K3

This chapter is the version submitted to the journal of "Fatigue & Fracture of Engineering Materials & Structures" on 11 June 2021 as a final revision for publication.

Abstract

Fracture behavior of the welded joints of 13% Cr-4% Ni stainless steels deposited using multipass flux-cored arc welding process was examined in both as-welded and heat-treated conditions, and J_{Ic} tests were performed. A crack starter notch was placed one millimeter far from the fusion line to evaluate the HAZ. Unstable crack propagations towards the weld metal occurred during stable tearing for both as-welded and heat-treated HAZ. Only single-point fracture toughness J_u values could be determined before fracture instability. The fracture toughness of the as-welded HAZ was about 60% lower than that of the substrate steel, but get significantly improved by heat-treatment, reaching a value even slightly higher than that of the substrate steel. The fracture mode of the stable tearing was transformed from a mix of cleavage and dimpled rupture occurring by micro-void coalescence mechanism for the as-welded condition to a totally dimpled rupture in the case of the heat-treated material.

Keywords: 13% Cr-4% Ni martensitic stainless steel; HAZ; Fusion line; Stable J_{Ic}-crack growth; Unstable crack propagation

Nomenclature

a	crack length (mm)
a_0	initial crack length (mm)
A_{pl}	crack propagation area under force-displacement curve (N.mm)
b_0	Initial ligament ($W-a_0$, mm)
B	whole thickness of the CT sample (mm)
B_N	net thickness (distance between the roots of the side grooves, mm)
D	inclusion diameter (μm)
D_0	average value of initial inclusion diameters (μm)
D_{0L}	average value of the inclusions larger than the $D_{0median}$ (μm)
$D_{0median}$	median diameter of inclusions (μm)
D_{0S}	average value of the inclusions smaller or equal to the $D_{0median}$ (μm)
E	Young’s modulus (GPa)
e_f	elongation at fracture
e_u	uniform elongation at necking
f	a function of the sample geometry (a and W)
F	Load (N)
H(D)	harmonic mean value of inclusion diameters (μm)
J	J-integral value for a given crack growth (kJ/m^2)
J-R curve	J-Resistance curve
J_{el}	elastic component of J (kJ/m^2)
J_{Ic}	initiation J value under plane strain condition (kJ/m^2)
J_{pl}	plastic component of J (kJ/m^2)
J_Q	fracture toughness J_{Ic} candidate value (kJ/m^2)
K	stress intensity factor ($MPa\sqrt{m}$)
K_{Ic}	plane strain stress intensity factor ($MPa\sqrt{m}$)
N_A	surface density of inclusions ($No./cm^2$)
S	inclusion spacing (μm)
T	tearing modulus
V_v	volume fraction of inclusions

W	Sample width (mm)
Δa	crack extension (mm)
Δa_p	physical crack extension (mm)
ΔK	stress intensity factor amplitude (MPa√m)
ν	Poisson ratio
σ_y	yield strength (MPa)
σ_{UTS}	ultimate tensile strength (MPa)

4.1 Introduction

Manufacture and repair processes of hydroelectric runners made of cast (CA6NM) or wrought (S41500) martensitic stainless steels are performed by Flux-Cored Arc Welding (FCAW) process, and filler metal (E410NiMo) of 13% Cr-4% Ni martensitic stainless is used. This category of stainless steels has a good resistance against corrosion and cavitation erosion, and a good combination of strength/ductility [5, 12, 60, 87, 88, 105]. Despite the high-quality manufacturing process, the existence of micro-scale defects such as second phase particles (mainly inclusions) and micro-cracks are inevitable in the microstructure of the welded and cast components. These discontinuities can act as detrimental stress raisers [17, 65-67]. As micro-scale flaws are present in the built structure, fracture toughness of the parts made using this procedure is important for improving the lifetime and reliability of a hydroelectric runner.

The Heat-Affected Zone (HAZ) is considered as a source of weakness in a welded joint [106-108], particularly in terms of unstable crack growth. The exposure to high thermal cycling during multipass welding, the HAZ presents significant microstructural heterogeneities and tensile residual stresses [11, 31, 109, 110]. In addition, the problem of cold cracking is also a matter of concern in the HAZ [6, 11, 31, 73, 111]. Therefore, unstable crack propagation is most likely to take place in the HAZ under high stress triaxiality ratios, affecting the reliability of the hydroelectric runner.

Ductile rupture, also called “dimpled rupture”, takes place by Micro-Void Coalescence (MVC) mechanism in which micro-voids initiate from inclusions, grow under increasing loading, and coalesce at final rupture. This fracture mechanism depends highly on the inclusion characteristics in the microstructure of the material [7, 8, 37]. The higher the inclusion density, the higher the density of nucleation sites, and the less significant will be the growth stage of micro-voids during rupture [61, 64]. In addition, the inclusion size is a matter of interest as it was shown that larger inclusions require lower stresses and strains to be detached from the matrix, initiating micro-voids [66, 67].

In this study, stable/unstable crack propagation in the base and weld metals, as well as in the HAZ of 13% Cr-4% Ni martensitic stainless steels is examined during J_{Ic} testing, and the weakest region in terms of stable/unstable crack propagation is revealed. Fracture behaviors are examined in both as-welded and heat-treated conditions as the whole hydroelectric runner undergoes a heat-treatment before the first launch (in order to improve the ductility of the martensitic matrix), but as-welded region of the runner can be used directly after reparation process. Fracture surfaces are examined using a Scanning Electron Microscope (SEM) coupled with an Energy Dispersive X-ray spectrometer (EDX) to study the fracture mechanisms involved and the nature of inclusions. The fracture characteristics i.e., mode, initiation sites, and propagation paths are determined, and the main differences in fracture behavior of the tested materials are evaluated.

4.2 Materials and experimental procedures

4.2.1 Materials

A welded joint of 13% Cr-4% Ni martensitic stainless steels composed of a 60 mm thick E410NiMo weld metal deposited by FCAW process on a 50 mm thick CA6NM substrate steel was fabricated (the overall dimensions of the welded block being 450 × 250 × 110 mm). For the first pass, the substrate steel (CA6NM) was pre-heated to 180 °C and subsequent passes were deposited at an inter-pass temperature of 200 °C. The other welding parameters and the as-welded block are shown in Table 4-1 and Figure 4-1, respectively. The weld metal and the HAZ were tested in both as-welded and heat-treated conditions. The heat treatment was performed at 600 °C for 2 hrs. In order for sample collecting and performing the heat treatment, the as-welded block was cut into smaller sections. Due to the large size of these cut sections, thermocouples were used to ensure proper application of the heat treatment. The Schematic cutting plan of the welded block is shown in Figure 4-2 (a). The CA6NM steel was tested in the as-received condition (fully tempered at 34 HRC). As CA6NM substrate steel is a cast material resulting in a martensitic structure, homogeneous properties are found and samples can be extracted from any direction in the cast plates.

Table 4-1 Welding parameters used for this study

Protection gas	Torch speed	Deposition rate	Current	Voltage	Heat input
75 % Ar+ 25% CO_2	4.5 (mm/s)	1.125 (g/s)	218 A	22.5 V	1090 (J/mm)

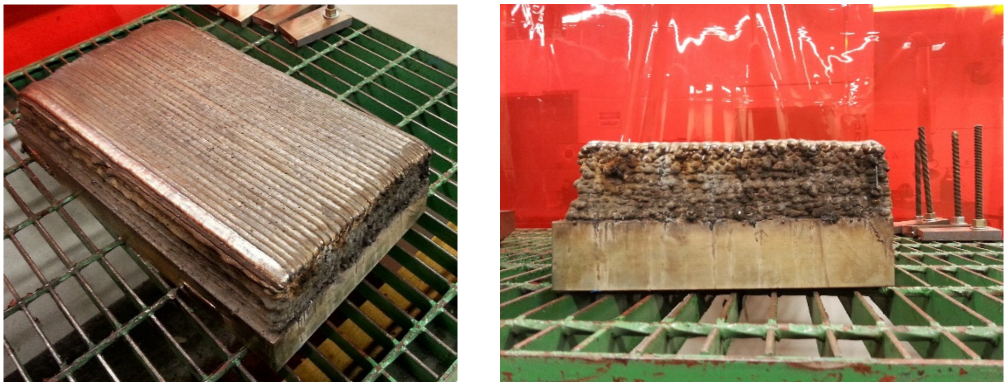
(a)
(b)

Figure 4-1 As-welded block shown from (a) global and (b) side view

The chemical compositions of the CA6NM, and the weld metal, as well as the corresponding standard requirements are provided in Table 4-2. Carbon and sulfur were measured by combustion, and the other elements were measured using plasma-emission atomic spectrometry. As can be seen in Table 4-2, all the materials used in this study are of similar chemical compositions being in the category of 13% Cr-4% Ni martensitic stainless steels. The CA6NM substrate steel is referred as the base metal in this study, and in the case of the weld metal the terms WM-AW and WM-HT, and for the HAZ the terms HAZ-AW and HAZ-HT are used to refer the as-welded and the heat-treated conditions, respectively.

Table 4-2 Chemical compositions of the tested materials (wt%)

Designation	C	Mn	P	S	Si	Cr	Ni	Mo
CA6NM	0.016	0.50	0.019	0.007	0.26	12.79	3.49	0.55
ASTM A743	0.06	1.00	0.04	0.03	1.00	11.5-14.0	3.5-4.5	0.40-1.0
	(max)	(max)	(max)	(max)	(max)			
E410NiMo	0.027	0.04	0.01	0.0093	0.48	12.1	4.67	0.61
AWS	0.06	1.0	0.04	0.03	1.0	11.0-12.5	4.0-5.0	0.4-0.7
A5.22/A5.22M	(max)	(max)	(max)	(max)	(max)			

4.2.2 Inclusion characteristics

Metallographic sections of the base and weld metals were polished using sand papers and diamond suspensions. The mirror-polished sections were examined by optical microscopy, and surface density (N_A), volume fraction (V_v), mean diameter (D), and average spacing (S) of inclusions were measured using an automatic image analyzer software ImageJ. The lowest possible magnifications were used in order to detect the largest inclusions found in the microstructure since the mechanical properties are majorly affected by large inclusions. Therefore, a low-level magnification of 50X was used in the case of the substrate steel (CA6NM); however, due to the very small size of all inclusions in the microstructure of the weld metal, a ten times higher magnification was used in this case (500X). Then, five optical micrographs, randomly taken from different regions of the metallographic sample surface, were analyzed per material. To this purpose, the optical micrographs were first transformed into binary images to make inclusions recognizable for the software. These binary images were composed of black and white pixels representing inclusions and the matrix, respectively. For best accuracy, the high resolution of the optical micrographs was maintained during binary image processing. Accordingly, the total areas of 14 mm^2 and 0.15 mm^2 were analyzed for the substrate steel and the weld metal, respectively. The inclusions were detected and enumerated automatically by the software. The area of each inclusion was measured and then the total inclusion area fraction found on each micrograph was calculated. This calculated area fraction represents the volume fraction of inclusions in the microstructure as described in ASM Handbook [78]. The number of inclusions measured for each image area was converted to square centimeter, and then reported as the inclusion surface density N_A for each image. The circle equivalent diameter of inclusions was then calculated and reported as the inclusion size D. The average inclusion spacing was calculated using the equation $S = 0.89\ D_0\ (V_v)^{-1/3}$ [16], where $D_0 = (\pi/4)\ H(D)$, and H(D) is the harmonic mean of the diameters. More details on these image analyzing processes were provided in [112].

4.2.3 Tension tests

Tension tests were carried out in accordance with ASTM E8/E8M [79] at room temperature using round bar samples with a diameter of 5 mm and a strain rate of $2.5 \times 10^{-4}\ s^{-1}$. Three tests per condition were performed for the base and weld metals.

4.2.4 Fracture toughness J_{Ic} tests

The single specimen J_{Ic} test method was used for all materials, but the procedure used to calculate and determine the J_{Ic} value was different between the substrate/weld materials and the HAZ. In the case of substrate/weld materials, it was possible to derive the J_{Ic} value from the J-R curve, and hence the J values were calculated for each partial unloading using single specimen test method formulas (detailed information on the J-R curve development was provided in the previous work [60]). To clarify, for HAZ only single-point fracture toughness values are obtained.

4.2.4.1 Base and weld metals

Fracture toughness J_{Ic} tests were performed using single specimen test method in accordance with ASTM E1820-18 [43]. 25.4-mm thick compact tension (CT) specimens with a thickness/width ratio of ½ were used, and side grooves with a depth of 10% of the whole thickness were machined on both sides of the sample. The schematic representation of the J_{Ic} specimen used in this study is shown in Figure 4-2 (b). Contrary to what is proposed in the standard [43], the side-grooving was carried out before fatigue pre-cracking in order for saving sample preparation time and producing a straighter fatigue pre-crack as demonstrated by Chen et al [93]. Fatigue pre-cracking with a stress ratio of 0.1 was carried out, and the original crack length reached up to 28 mm which corresponds to a 0.55 ratio for the original crack length/width (a_0/W) [94]. A constant ΔK value of 14 MPa√m was used for the base metal, and that of 12 MPa√m were used for the weld metals (in both as-welded and heat-treated conditions). Three J_{Ic} tests were carried out per material/condition.

The length of both original and final cracks was predicted by compliance method using elastic unloading of 10% of the actual maximum load during J_{Ic} testing, and a clip-on gage was used to measure the total displacement. Heat tinting at 450 °C for 2 hrs, and fatigue cycling were used to mark the final crack fronts. Plane strain crack straightness requirements were examined in accordance with ASTM E1820-18 [43] for both original and final crack fronts. The candidate values of the fracture toughness J_Q satisfied the standard requirements, and could be considered as the plane strain fracture toughness J_{Ic} for these materials. The fracture toughness K_{Ic} could then be calculated using the following equation:

$$J_{Ic} = (1-\nu^2)\frac{K_{Ic}^2}{E} \tag{4.1}$$

where *v* is Poisson ratio and *E* is Young's modulus [7, 8].

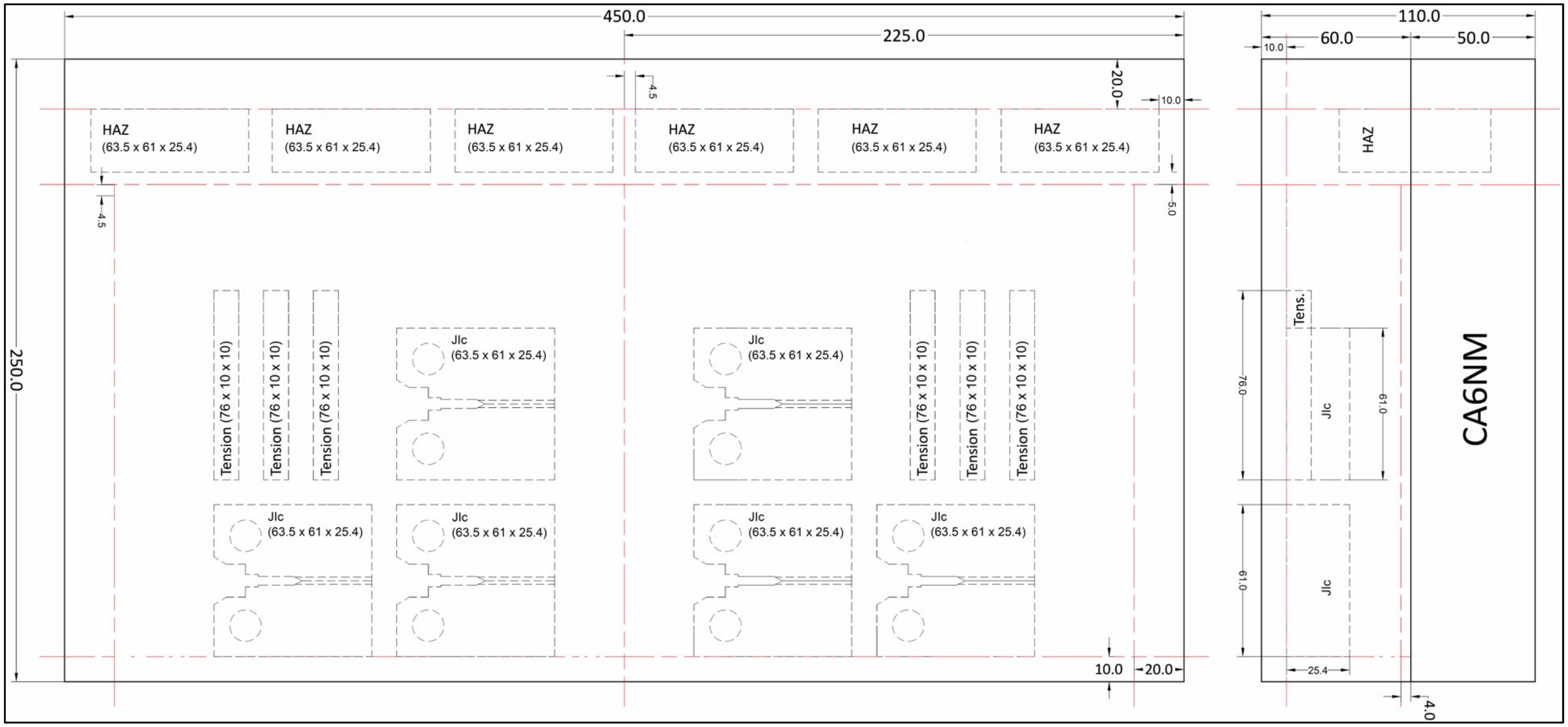
450.0
225.0
110.0
60.0
50.0
10.0
4.5
20.0
10.0
HAZ
(63.5 x 61 x 25.4)
HAZ
(63.5 x 61 x 25.4)
HAZ
(63.5 x 61 x 25.4)
HAZ
(63.5 x 61 x 25.4)
HAZ
(63.5 x 61 x 25.4)
HAZ
(63.5 x 61 x 25.4)
HAZ
4.5
5.0
250.0
Tension (76 x 10 x 10)
Tension (76 x 10 x 10)
Tension (76 x 10 x 10)
Jlc
(63.5 x 61 x 25.4)
Jlc
(63.5 x 61 x 25.4)
Tension (76 x 10 x 10)
Tension (76 x 10 x 10)
Tension (76 x 10 x 10)
Tens.
76.0
Jlc
61.0
CA6NM
Jlc
(63.5 x 61 x 25.4)
Jlc
(63.5 x 61 x 25.4)
Jlc
(63.5 x 61 x 25.4)
Jlc
(63.5 x 61 x 25.4)
61.0
Jlc
10.0
20.0
25.4
4.0

(a)

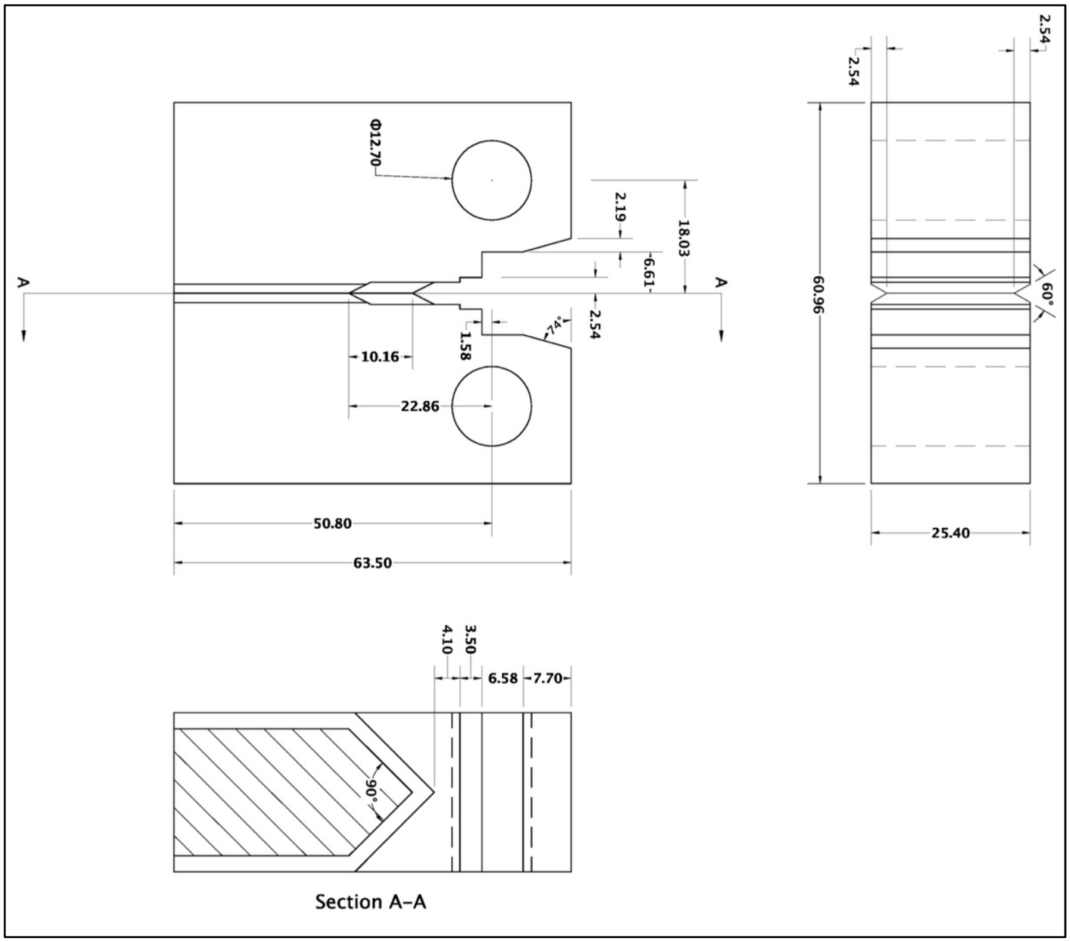

(b)

Figure 4-2 Schematic representations of (a) cutting plan of the welded block including the right-side view (dimensions in mm), and (b) the side-grooved J_{Ic} specimen (top left) together with the side (right) and section (below) view. Three CT samples per condition (as-welded and heat-treated) were collected from the weld metal and the HAZ. The red dashed lines in (a) mark the major cutting lines designed for removing the weld metal from the substrate, cutting the edge-side and surface welding beads, and divide the welded block into two parts. One of the blocks was heat treated

In order to compare the crack growth behaviors, tearing modus values were calculated using the following equation [7]:

$$T = \frac{E}{\sigma_y^2}\frac{dJ}{da} \tag{4.2}$$

The parts of the J-R curves located between the exclusion lines were used to calculate the dJ/d*a* values and the linear regression method was used.

4.2.4.2 HAZ

The same J_{Ic} test procedures as those of the weld metals were used, and five side-grooved CT specimens were tested: two specimens for the as-welded, and three other ones for the heat-treated condition. The crack starter notch was placed one millimeter away from the fusion line to observe material behavior during stable tearing in the HAZ close to the fusion line in the base material. This region was considered as the weakest region in terms of crack propagation properties based on its higher hardness (39 HRC). To determine the region of interest and location of the crack starter notch prior to the machining of the CT specimens, the welded joint surfaces were polished to a mirror appearance using sand papers and diamond suspensions, and then etched using modified Fry's solution [5] (150 mL distilled water + 1 g $CuCl_2$ + 50 mL HCl + 50 mL HNO_3) to reveal the exact location of the fusion line.

Among the J_{Ic} tests performed in the HAZ only one complete stable tearing crack extension had occurred for one of the as-welded samples, but the test result was still rejected as the standard final crack straightness requirements were not satisfied. All the other tests terminated by fracture instability (unstable crack propagation). Therefore, single-point fracture toughness values were determined for each condition at the final unloading sequence where unstable crack propagation occurred. The basic method proposed by ASTM E1820-18 [43] was used to calculate the total fracture toughness as the sum of the elastic J_{el} and plastic J_{pl} components and

$$J_{el} = (1-\nu^2)\frac{K^2}{E} \tag{4.3}$$

and,

$$K = \frac{F}{\left(BB_N W\right)^{0.5}} f\left(\frac{a}{W}\right) \tag{4.4}$$

where, F is the load, B is the whole thickness, B_N is the distance between the roots of the side grooves, f is a function of the sample geometry (a and W), and:

$$J_{pl} = \frac{\eta_{pl} A_{pl}}{B_N b_0} \tag{4.5}$$

where, $\eta_{pl} = 2 + 0.522 b_0 / W$, A_{pl} is the corresponding crack propagation area under force-displacement curve, and b_0 is the initial ligament (W-a_0).

The resulted J values were then corrected for physical crack extensions measured on the broken J_{Ic} samples Δa_p using [113]:

$$J_Q = J_{el} + \frac{J_{pl}}{1 + \frac{0.29 \Delta a_p}{b_0}} \tag{4.6}$$

The corrected J_Q values were qualified as fracture toughness J_u according to ASTM E1820-18 since significant stable tearing crack extension occurred prior to unstable crack propagation in the HAZ condition. The difference between J_{Ic} and J_u values is that J_{Ic} is a size-independent value, whereas J_u may still be sensitive to the specimen thickness [7].

4.2.5 Fractography

All fracture surfaces were examined using SEM coupled with EDX in order to determine fracture micromechanics involved in each case.

4.3 Results

4.3.1 Microstructure

The inclusion characteristics of the materials tested in this study were measured on the mirror-polished sections of the as-received materials, and examples of the processed images as well as the analyzed data are shown in Figure 4-3 and Table 4-3, respectively. The enumerated particles seen in Figure 4-3 are the inclusions that have been automatically detected by the software. For the base metal (CA6NM), the inclusion size could not be described by a normal distribution. Accordingly, the median diameter was chosen as a discriminating parameter, separating small and large inclusions. By contrast, normal distributions were found in the case of the weld metals and only the average values calculated for all inclusions were reported.

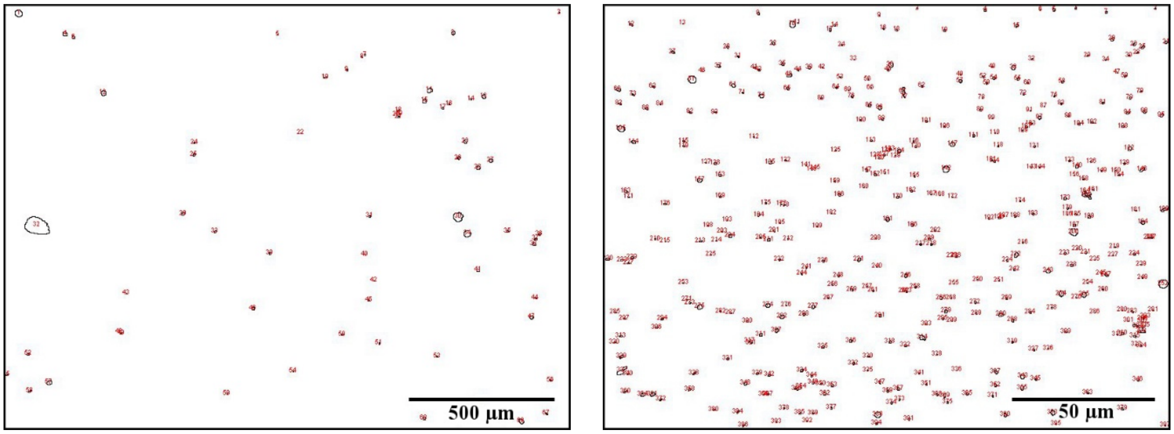

(a) (b)

Figure 4-3 Analyzed optical micrographs from (a) CA6NM and (b) E410NiMo, showing inclusions detected and enumerated automatically by the "ImageJ" software

Table 4-3 Inclusion characteristics measured on the mirror polished sections of the base and weld metals

Designation	Measured inclusions	Volume fraction (%)	Surface density (No./cm^2)	Size (Mean diameter, µm)	Spacing (µm)
CA6NM	D_0 (All)	0.22 ± 0.12	1620 ± 368	9.98 ± 8.62	37.07 ± 5.73
	D_{0S}[a]	0.02 ± 0.01	873 ± 232	5.26 ± 1.58	56.54 ± 5
	D_{0L}[b]	0.20 ± 0.11	754 ± 176	15.46 ± 5.05	71.76 ± 6.7
E410NiMo	D_0 (All)	1.10 ± 0.14	(1.29 ± 0.25) ×10^6	0.76 ± 0.02	1.89 ± 0.10

[a]-The average of dimeters of inclusions smaller than the median diameter. [b]- The average of dimeters of inclusions larger than the median diameter. The median diameter was equal to 7.46 µm.

The differences in inclusion characteristics between the base metal and the weld metal are significant, providing a large range of material characteristics. The surface density of inclusions in the weld metal is about 800 times higher than the base metal, and the inclusion volume fraction is five times higher. On the other hand, the inclusion size and the inclusion spacing are about 10 and 20 times smaller, respectively.

The typical microstructure found in the HAZ at one millimeter away from the fusion line is shown in Figure 4-4. A lath martensitic matrix with a small amount of delta ferrite can be found. This martensitic matrix is partially tempered by the welding passes made one millimeter further. The delta ferrite regions identified by white arrows are found in the microstructure. These regions de not contribute to fracture micromechanics. They are formed at temperatures higher than about 1300 °C and remain stable to room temperature due to the concentration of some ferrite-promoting elements such as Cr [2]. Delta ferrite being softer than the surrounding martensitic matrix, its presence in the microstructure didn't affect the fracture micromechanics unless large brittle chromium carbides forms in it [54], and this is not the case in the present study thanks to the low amount of C present in the alloy.

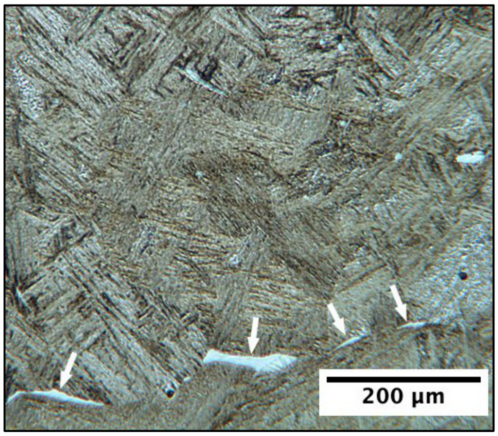

Figure 4-4 Typical microstructure of the targeted HAZ in as-welded condition. Some stringers of delta ferrite are shown by the white arrows. The weld is 1 mm below this image

4.3.2 Mechanical characterization

4.3.2.1 Tension properties

Tension properties of the tested materials are provided in Table 4-4. As can be clearly observed, the weld metals have higher strength but lower ductility than the CA6NM substrate steel. As-welded condition provides the most resistant, but the least ductile material. The ductility was significantly improved by about 30% after heat treatment, keeping high values of yield and tensile strengths. The uniform elongation of CA6NM steel is more than twice than that of WM-AW, and 40% more than that of WM-HT. In a similar way, the elongation at fracture of CA6NM is about 65% and 30% higher than those of as-welded and heat-treated materials.

Table 4-4 Tension properties of the studied materials

Designation	σ_y (MPa)	σ_{UTS} (MPa)	e_u[a] (%)	e_f[b] (%)
CA6NM steel	575 ± 13.2	769 ± 7.4	9.5 ± 0.4	19.4 ± 1.7
WM-AW	783 ± 5.8	1007 ± 10.3	4.4 ± 0.1	11.9 ± 0.2
WM-HT	765 ± 5	895 ± 4	6.8 ± 0.3	15.2 ± 0.4

[a]-Uniform elongation; [b]-Elongation at fracture

4.3.2.2 Fracture toughness properties

The load-displacement curve obtained during J_{Ic} testing of the as-welded HAZ and the first test performed on heat-treated condition (HAZ-HT1) are shown in Figures 4-5 (a) and (b), respectively. The partial unloadings shown in these figures were performed before the J_{Ic} test terminated by unstable crack propagation. In fact, these sequences are used to calculate the proper compliance (displacement/load) which can be used to estimate the crack growth (Δa) and calculate the corresponding J value. However, since after the last partial unloading sequence ductile tearing terminated by unstable crack propagation, the J value could only be calculated at the last partial unloading sequence. In this case, the term “single-point fracture toughness” is used by ASTM E1820-18 to specify that the fracture toughness value was calculated without tracing the J-Resistance curve. In accordance with the section 9.1.4 of the standard, contrary to the case in which the J_{Ic} value determined on the J-R curve, the final crack front straightness does not have to be taken into consideration in the validity of the single-point fracture toughness; only the original crack front should be straight.

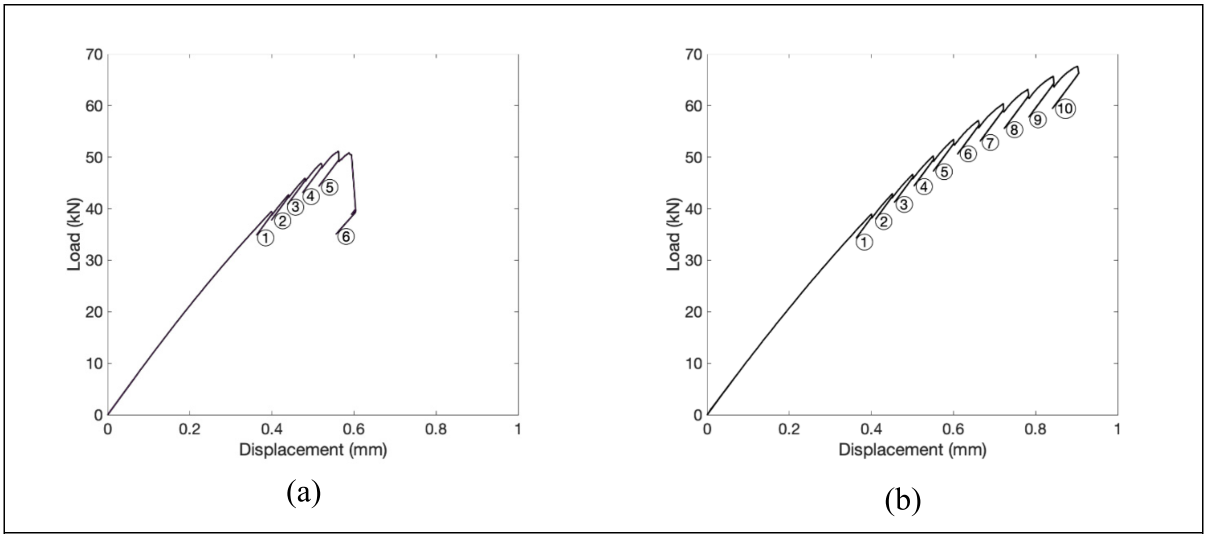

Figure 4-5 Examples of the load-displacement curves obtained during J_{Ic} tests on the HAZ in (a) as-welded and (b) heat-treated conditions. The circled numbers indicate partial unloading sequences performed during J_{Ic} tests, showing that stable tearing occurred before unstable crack propagation

For load-displacement curves of the HAZ, the crack growth values (Δa) cannot be precisely estimated by compliance method due to the curved final crack front. Therefore, the overall stable tearing crack extension (physical crack extension, Δa_p) was measured on the broken samples and the J_u value was calculated using equation (4.6).

The J values of the valid tests performed on the HAZ are reported in Table 4-5. The elastic (J_{el}) and plastic (J_{pl}) parts of the J_u value are higher for the heat-treated condition by factors at least three and two times, respectively. Larger crack tip opening displacements and higher loads are required for stable tearing crack extension (comparing Figure 4-5 (a) and Figure 4-5 (b)), resulting consequently in a larger J_{el} value as calculated using equations (4.3) and (4.4). Accordingly, a larger plastic zone is formed at the stable tearing crack front, increasing the area under the load-displacement curve (A_{pl}), and hence a higher J_{pl} value is obtained (equation (4.5)).

Table 4-5 Fracture toughness properties of the HAZ calculated at the final unloading sequence for as-welded and heat-treated conditions

Designation	J_{el} (kJ/m^2)	J_{pl} (kJ/m^2)	J_u (kJ/m^2)
HAZ-AW	37	86	122
HAZ-HT1	106	170	275
HAZ-HT2	110	202	308
HAZ-HT3	121	298	409

The J-R curves of the CA6NM substrate steel and weld metals, as well as their resultant average fracture toughness properties and the J_u values of the HAZ are provided in Figure 4-6 and Table 4-6, respectively. The shape of the J-R curves is also different between CA6NM substrate steel and weld metals; the substrate steel has a rising J-R curve and a high tearing modulus T value, whereas the J-R curves reach a plateau in the weld metals having very low T values. It shows that the crack driving force should be highly increased in the case of the substrate steel in order for stable tearing to be occurred. However, the stable tearing took place under constant crack driving forces in the weld metals, resulting in at least 7 times and 13 times lower dJ/da and tearing modulus (T) values, respectively.

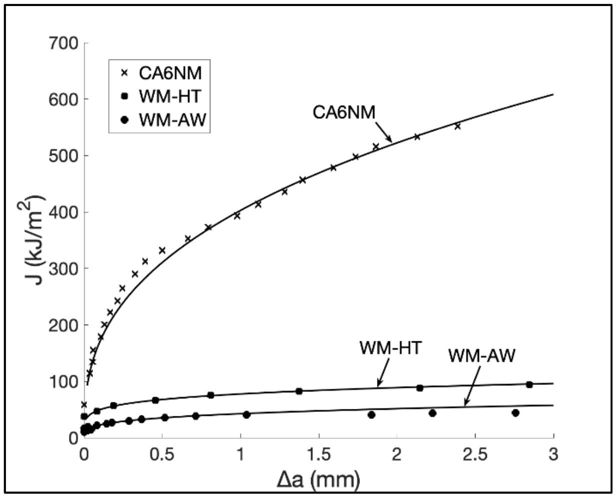

Figure 4-6 J-R curves of the base metals and weld metals

Table 4-6 Plane strain fracture toughness properties of the tested materials

Designation	dJ/da (MPa)	T	$J_{Ic}/J_u{}^{a}$ (kJ/m^2)	$K_{Ic}{}^{b}$(MPa√m)
CA6NM	153 ± 2	92 ± 1	299 ± 13	256 ± 6
HAZ-AW[c]	-	-	122[d]	-
HAZ-HT[c]	-	-	331 ± 70	-
WM-AW	14.5 ± 2	5 ± 0.7	31 ± 4	82 ± 5
WM-HT	21.6 ± 0.9	7 ± 0.3	59 ± 0	114 ± 0

[a]- J_{Ic} values were reported for the CA6NM, WM-AW, and the WM-HT, and J_u values were reported for the HAZ-AW and HAZ-HT.

[b]- Equivalent K_{Ic} values were calculated only for the J_{Ic} ones to provide comparative values.

[c]- Calculated using the single-point fracture toughness method.

[d]- Only one test out of the three gave a valid J_u in the as-welded HAZ so no standard deviation could be estimated.

4.3.3 Fractography

As mentioned in the section 4.2.4.2, stable tearing occurred before unstable crack propagation in the HAZ for both as-welded and heat-treated materials. An example of the broken J_{Ic} sample tested in the heat-treated HAZ is shown in Figure 4-7. After a small stable tearing crack extension with an average length of about 2.5 mm, unstable crack propagation occurred towards the weld metal. According to ASTM E1820-18 [43] the straightness of the final crack front is not verified since the test terminated in an unstable crack propagation mode. The only criterion is the straightness of the fatigue pre-crack, which in the present case is valid. The wavy appearance of the unstable crack propagation path proves that the fracture instability took place whether in the region of the CA6NM substrate steel that has been dissolved during the first weld pass or directly towards the weld metal itself. Determining the nature of inclusions located in the unstable crack propagation path can precisely reveal that unstable crack propagation was occurred in which one of the proposed paths.

In order for shedding light on the fracture micromechanical processes involved during J_{Ic} testing, both stable tearing and unstable crack propagation paths were examined using SEM. A typical region of the stable tearing of the tests carried out in the HAZ in as-welded and heat-treated conditions are shown in Figures 4-8 (a) and (b), respectively. For comparison purpose, the stable tearing fracture surface of CA6NM substrate steel was also added (Figure 4-8 (c)) as a reference. Some cleavage facets shown by the black arrows are observed in the as-welded HAZ (Figure 4-8 (a)), whereas only large and small dimples are observed after heat treatment (Figure 4-8 (b)). The latter features are similar to the one observed in the tempered martensitic matrix found in the CA6NM substrate steel (Figure 4-8 (c)).

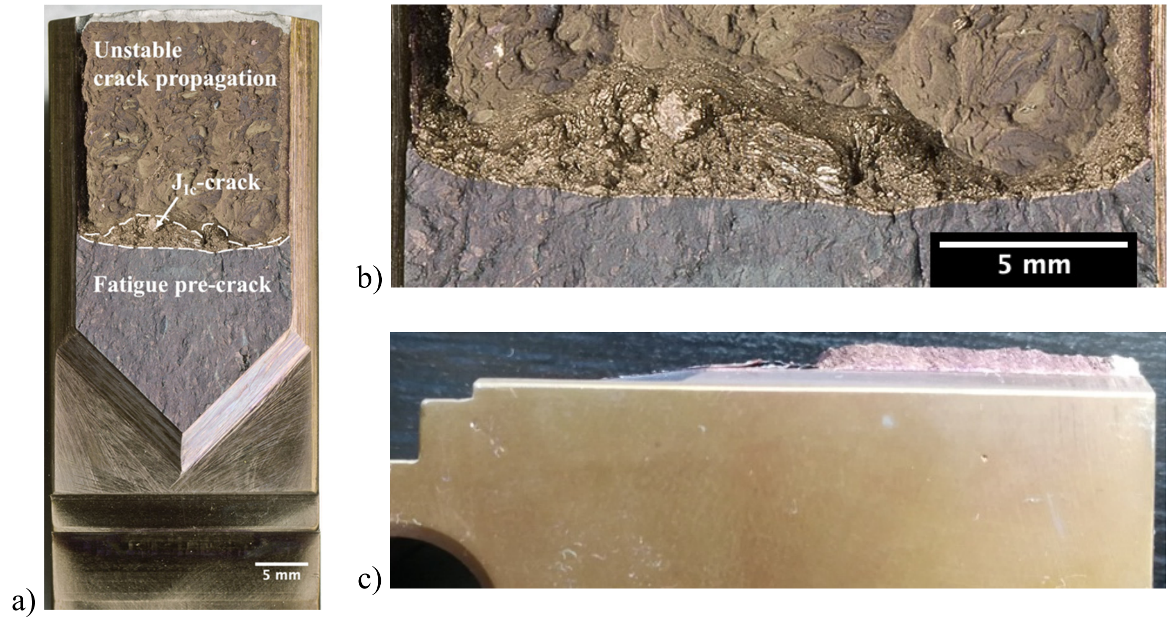

Figure 4-7 An example of a broken J_{Ic} sample tested in the heat-treated HAZ, showing a (a) global view of the fracture surface, (b) a zoom of the region representing the stable tearing, and (c) a side view of the sample

In the case of the as-welded condition in which cleavage and dimpled rupture existed together (Figure 4-8 (a)), analyzing a total area of about 2.5 mm^2 revealed that stable tearing consisted of about 50% cleavage rupture. The cleavage ruptures have a multifaceted appearance since the crack direction changes to be propagated along the most favorably oriented crystallographic planes for cleavage [7, 8]. By contrast, dimpled rupture taking place by MVC mechanism is the only fracture mechanism involved in the case of heat-treated HAZ (Figure 4-8 (b)) and CA6NM substrate steel (Figure 4-8 (c)). The ductile fracture characteristics are the same between these materials: large dimples existed together with small ones and both, rupture of inclusions and decohesion at matrix/inclusion were found to be at the onset of micro-voids formation.

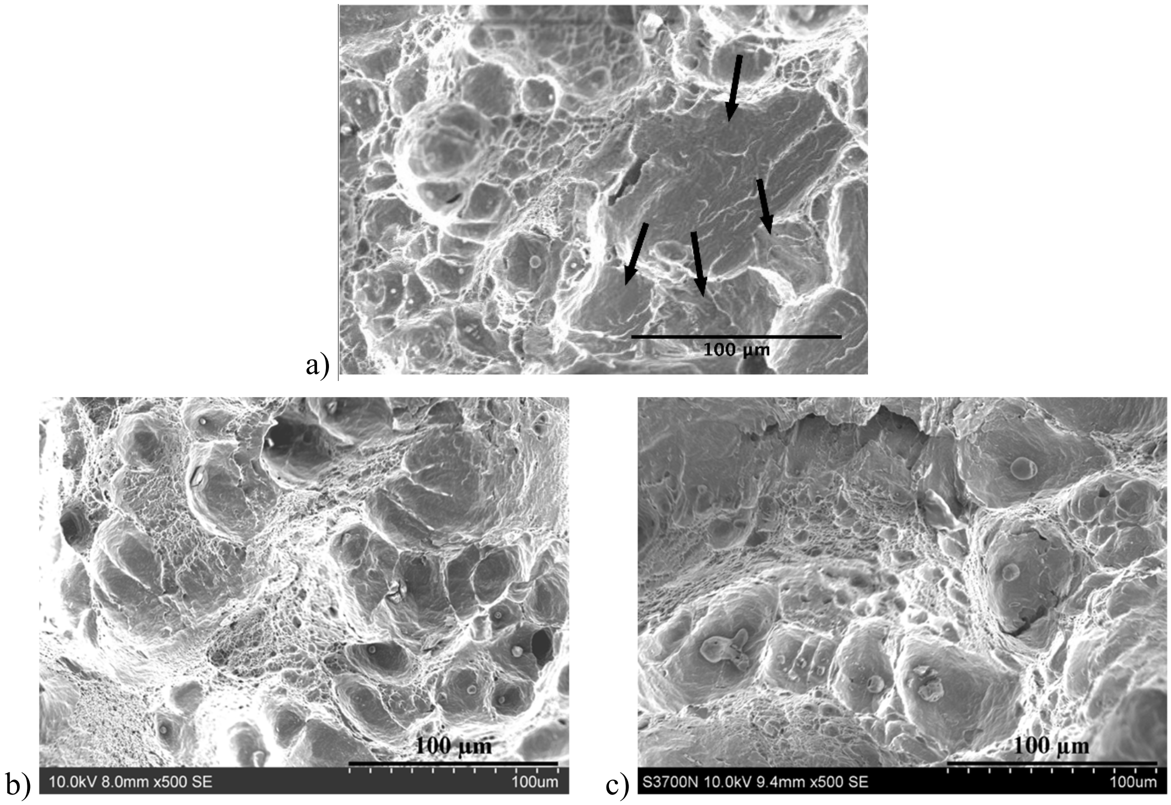

Figure 4-8 SEM micrographs of stable tearing in (a) HAZ-AW, (b) HAZ-HT, and (c) CA6NM substrate steel

The unstable crack propagation paths of the J_{Ic} tests carried out in the HAZ in both as-welded and heat-treated conditions were examined by SEM in order for determining the weakest region in terms of crack propagation resistance. Typical SEM micrographs of these unstable crack propagation paths are shown in Figures 4-9 (d) and (e) on large and small scales, respectively. Dimpled rupture is the dominant fracture mode, but some very small cleavage facets are also observed on the unstable crack propagation path in Figure 4-9 (a). These ductile fracture characteristics are totally different from the ones observed in the case of stable tearing in the heat-treated HAZ (Figure 4-8 (b)) and the CA6NM substrate steel (Figure 4-8 (c)). For comparison purpose, an SEM micrograph of a typical stable tearing region in the heat-treated weld metal can be found in Figure 4-9 (c). The fracture appearance is very similar in the unstable crack propagation path (Figure 4-9 (b)) supporting that the unstable crack propagates in the weld metal. A typical inclusion found in the unstable crack propagation path is shown in Figure 4-10 (a). Local EDX spectrum shows that this inclusion is composed of an oxide of Al, Si, Zr, Mn, Cr, and Ti, which is typical of the welded material. The inclusion detected in the substrate steel were more composed of Si, Mn, and S as shown in Figure 4-10 (b). This also confirms that the inclusions found in the unstable crack propagation path were of the same nature as those in the weld. As inclusion characteristics are not influenced by heat treatment due to their nature and origin [114], the fracture appearance of stable tearing in the weld metal was very similar between the as-welded and heat-treated conditions.

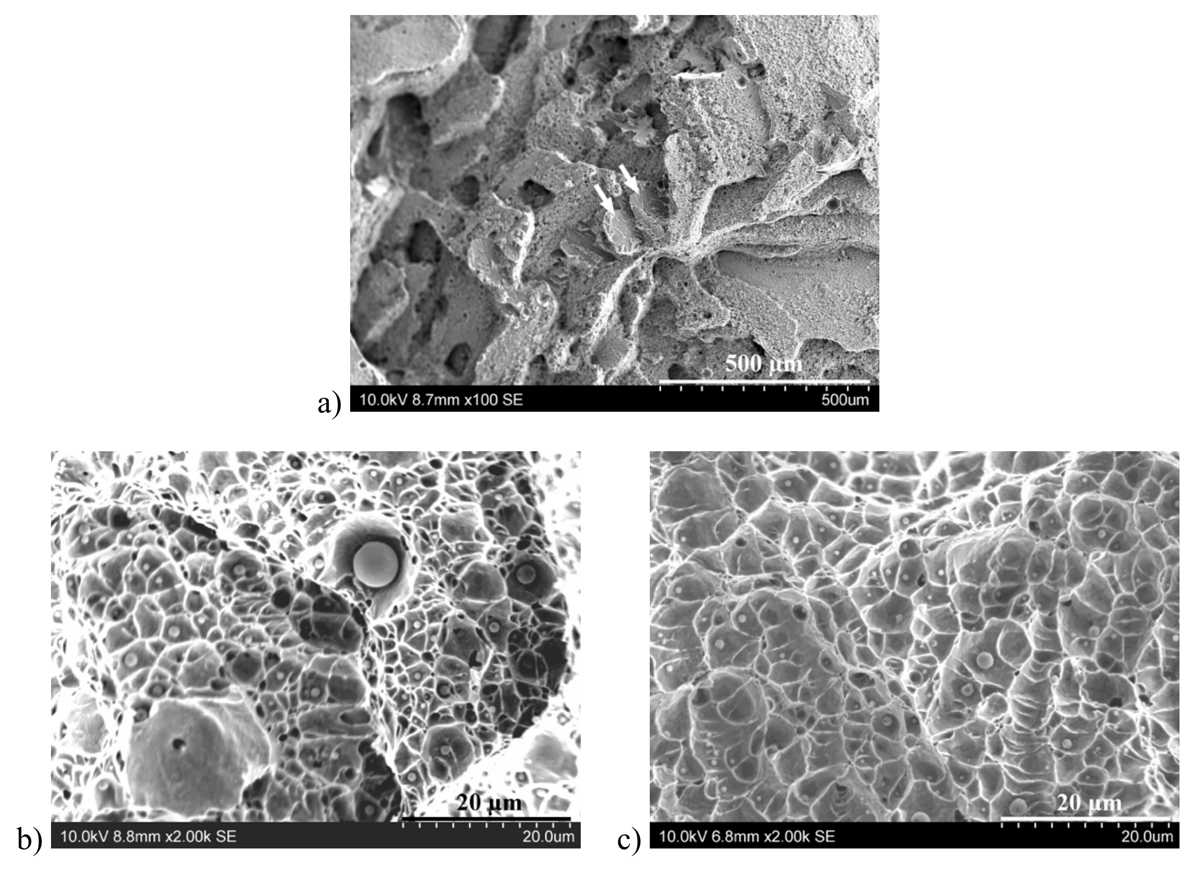

Figure 4-9 SEM micrographs of (a, b) unstable crack propagation paths in the HAZ-HT in 100X and 2000X, respectively, and (c) stable tearing in the heat-treated weld metal

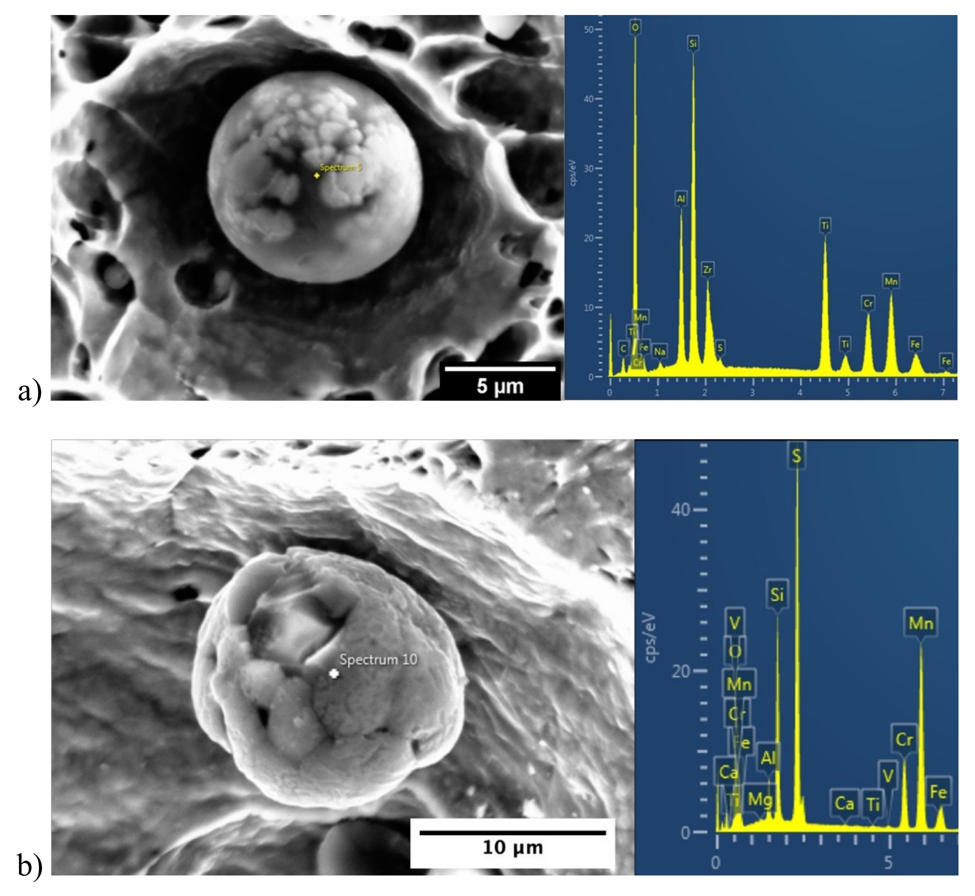

Figure 4-10 Typical inclusions found on the (a) J_{Ic} unstable crack propagation path, and (b) in the substrate fracture surface with their EDX spectrum at the right

4.4 Discussion

In the case of J_{Ic} tests performed in the HAZ, the J-R curves were not developed since unstable crack propagations occurred towards the weld metal for both as-welded and heat-treated conditions. Accordingly, only single-point fracture toughness J_u values were obtained for each tentative (ASTM E1820-18), contrary to the case of the substrate material and the weld metals for which the whole crack growth resistance curves were obtained (Figure 4-6). As provided in Table 4-6, the fracture toughness J_{Ic} of the as-welded or heat-treated weld metals is at least five times lower than that of the substrate steel. On the other hand, the fracture toughness J_u of the HAZ is significantly higher than that of the weld metals for both as-welded and heat-treated conditions. If the fracture toughness of the HAZ after heat treatment (HAZ-HT) is of the same order of magnitude than the CA6NM substrate steel, the HAZ in the as-welded condition (HAZ-AW) is intermediate between the CA6NM substrate steel and the heat-treated weld metal (WM-HT).

Furthermore, fracture micromechanics are different between the HAZ-AW, and HAZ-HT and the substrate steel: a mix of cleavage and dimpled rupture was observed in the case of HAZ-AW (Figure 4-8 (a)), whereas only dimpled rupture occurred in the HAZ-HT (Figure 4-8 (b)) and the substrate steel (Figure 4-8 (c)). In fact, as negligible plastic deformations are required for cleavage to take place, it is most likely that fracture occurred first by cleavage in some grains favorably oriented ahead of the crack tip. Then, the unfavorably oriented ligaments will deform and eventually rupture with dimpled marks. Indeed, as crack opens during stable tearing, rupture is then controlled by the failure of these ligaments, increasing the driving force for crack propagation. Interestingly, the river patterns formed due to different propagation direction within a prior austenite grain [7, 8] are also observed in Figure 4-8 (a). This may suggest that prior austenite grain size could affect the fracture toughness of the as-welded HAZ.

Dimpled rupture occurred during stable tearing in HAZ-HT and substrate steel, as well as during unstable crack propagation, but different micromechanical processes are involved: In the case of the stable tearing crack extension, dimples were first nucleated on large inclusions (Figure 4-8 (b) and Figure 4-8 (c)). Then other dimples were initiated from smaller inclusions as the strain increased in the ligaments between the initially formed dimples. More significant void growth took place in the dimples initially nucleated on large inclusions before their growth gets limited by the formation of second series of micro-voids. By contrast, in the case of unstable crack propagation, the formation of very small dimples on the very small closely spaced inclusions is at the origin of the premature coalescence of micro-voids (Figures 4-9 (a) and (b)). The term “premature coalescence” regards the fact that impingement happens between the nucleated micro-voids without significant growth. The detailed examination of the nature of inclusions showed that the unstable crack propagation was not a decohesion between the CA6NM substrate and the deposited weld metal, but rather a fracture process that took place in the weld metal itself.

The occurrence of unstable crack propagation in the HAZ can be due to the fact that the base metal (CA6NM) is a significantly ductile and tougher material compare to the weld metals. Therefore, the final crack propagates towards the weld metal as crack tip plastic zone is much smaller, and hence much lower crack driving forces are required for crack propagation. The lower inclusion spacing S in the weld metals (about 20 times lower than that in the substrate steel (Table 4-3)) results in a low critical plastic deformation during void growth stage in MVC, reducing considerably the energy required for final rupture.

The presence of cleavage rupture in the fracture surface of the as-welded HAZ (Figure 4-8 (a)) is associated with a significant drop of fracture toughness. The cleavage rupture represents more than half of the fracture surface. This results in a decrease in the plastic contribution of the energy release rate (J_{pl}) that is needed for crack propagation, reducing the J_u value. The later value was reduced by a factor of 2.6, what is coherent with the fact that cleavage rupture requires negligible deformations compare to ductile rupture, and hence only half of the material can sustain the load in front of the crack plastically. The increase in the fracture toughness J_u after heat treatment is due to the suppression of the cleavage behavior of some regions of the HAZ. However, the fracture toughness J_u of as-welded HAZ is higher than the J_{Ic} value weld metal. This can be explained by the much smaller inclusion spacing in the weld material, representing the weakest element of the weld structures.

The significant difference between the slope of the J-R curves of CA6NM and the weld metals (153 MPa for CA6NM vs. 22 MPa for WM-HT and 14 MPa for WM-AW) indicates that much lower crack driving forces are required to maintain the crack propagation in the weld metal. On the other hand, the HAZ is not the weakest region for crack propagation in the present material conditions. Even in the as-welded condition (HAZ-AW), the J_u value may be only about one-third of that of the heat-treated condition (HAZ-HT), but it is at least twice higher than the J_{Ic} value of the weld metal. Therefore, the crack propagation in a welded structure will not confine itself to the substrate HAZ and will move towards the weld as soon as the plastic region of the crack tip reaches the weld material, undergoing enough plasticity to initiate micro-voids. Crack propagation path will move from the HAZ to the weld, and because the growth contribution of these micro-voids is negligible before impingement, the fracture toughness will drop dramatically. It is the high density of small size particles in the weld material that seems detrimental, resulting in a total breakdown of the welded joint even in the heat-treated condition.

4.5 Conclusions

Plane strain fracture toughness J_{Ic} values were determined from J-R curves for the base and weld metals; however, in the case of the tests performed on the HAZ, only single-point fracture toughness J_u values were calculated at the final partial unloading sequence as unstable crack propagation occurred after significant stable tearing. The fracture toughness J_u of the as-welded HAZ is about 60% lower than the J_{Ic} value of the substrate, whereas in the heat-treated condition, it is 11% higher. The fracture toughness J_u value of the HAZ in as-welded or heat-treated condition is significantly higher than the J_{Ic} values of the weld metals, whatever the heat treatment conditions. It shows that even for the as-welded condition, the HAZ is more resistant than the weld metal in terms of fracture initiation/propagation, and this is the weld metal that is the source of weakness in the welded joints of these materials.

The fracture surface of the stable tearing in the HAZ differs between the as-welded and heat-treated conditions. For the only test performed on the as-welded condition a mix mode was observed: cleavage and dimpled rupture took place with a proportion of about 50%. In the case of the heat-treated HAZ only dimples were found. It can be concluded that the heat treatment at 600 °C for 2hrs was able to transform the fracture mode from a mix of dimpled rupture and cleavage into a totally dimpled rupture. The fracture instability occurred by dimpled rupture in both as-welded and heat-treated HAZ as unstable crack propagation direction deviates and goes to the weld material.

Acknowledgments

Financial supports of Natural Science and Engineering Research Council of Canada (NSERC), Hydro-Québec, and Alstom Power Hydro are gratefully acknowledged. SEM-EDX examinations were performed at the Institut de Recherche d'Hydro-Québec (IREQ). The tension and J_{Ic} tests were performed at École Polytechnique de Montréal under supervision of Mr. Yves Verreman. The authors of this paper would like to thank Mr. Jianqiang Chen for his valuable contribution during J_{Ic} testing of the first sample of each of the base metals (CA6NM and 415). We would also like to thank Mr. Mathieu Paquin for the manufacture of the excellent quality weld metal block. The valuable experimental assistance of Mrs. Manon Provencher, Mr. Denis Thibault, Mr. Étienne Dallaire, Mr. Alexandre Lapointe, technologists at IREQ, and Mrs. Josée Laviolette, technologist at École Polytechnique de Montréal are gratefully acknowledged.

Conflict of interest: The authors declare that they have no conflict of interest.

CHAPTER 5

DISCUSSION

The aim of this chapter is to provide an overall discussion on the results obtained throughout the scientific papers presented in chapters 2, 3, and 4 to draw an overall conclusion on fracture behavior of 13% Cr-4% Ni martensitic stainless steels.

5.1 Micro-void coalescence micromechanics

Fracture behaviors of the base and weld metals were characterized by the modified model of Rice and Tracey during tension test (article 1, chapter 2). The complexity of the inclusion distribution has been considered and used as the basis for various scenarios explaining the fracture micromechanics. For the base metals, the distributions were divided in two major size ranges i.e., R_{0S} and R_{0L} (as described in Table 2-2) based on the median value $R_{0median}$, which gave a good estimate of the typical inclusion sizes found on the regions of the fracture surface that initiated fracture. In the case of the weld metals, inclusions were normally distributed and the inclusion size average value was a good representative for all inclusions.

Actually, one of the main contributions of the first paper is to show that according to the distribution of particles present in the material, the rupture micromechanics controlling deformation after necking will differ. For the CA6NM, it was shown that large and small inclusions play a different role during the rupture: the large ones initiate the damage mechanisms, while the small ones control the final rupture of the ligament between the coalescing voids. On the contrary, the small inclusions promote rupture for 415 steel, showing that local inclusion distribution controls rupture in this material. In the case of the weld material, it is the density of particles that control the MVC mechanism and all particles are potential sites for crack nucleation.

It was shown with the aid of modified Rice and Tracey model that the deformation occurring during rupture is related to the ratio of half the average inclusion spacing R_f to the inclusion radius R_i, defining a critical void growth parameter $\ln(R_f/R_i)$. The estimated deformations were in a good agreement with the measured ones for heat-treated materials (415, CA6NM, and 410NiMo-HT), despite the fact that the results were also affected by some relatively small errors. In the case of CA6NM and 410NiMo-HT the estimated fracture strains were larger than the measured values, while a lower fracture strain was calculated for 415.

The reason why in 415 steel the estimated ε'_n deformation was 12% lower than the measured ε_n one is that the small ε_{vs} deformation (i.e. deformation occurring during void sheeting) was not considered for void growth calculation. This is due to the fact that void sheeting stops the void growth stage, promoting rupture by a quasi-immediate coalescence under lower deformations. If the half average inclusion spacing is considered as the R_f for a conventional micro-void impingement in this alloy, it can be concluded that the formation of void sheets has decreased the critical void growth ($\ln(R_f/R_i)$) by half (2.71 vs. 1.26).

Results obtained in the first article can also be used to relate the size and spacing of inclusions found in the microstructure to fracture toughness J_{Ic}/K_{Ic}. In fact, according to equation (2.8), a higher R_f/R_i ratio results in a higher void growth, and hence a higher deformation will occur during stable crack growth. That is to say, higher values of fracture toughness J_{Ic}/K_{Ic} and ε_n are expected for a higher R_i/R_f ratio. This is in a very good agreement with the experimental results reported in the third paper (chapter 4). Table 5-1 shows the relation between the R_f/R_i ratio and fracture properties (ε_n, J_{Ic}, and K_{Ic}): the higher the R_f/R_i ratio, the higher the ε_n and fracture toughness J_{Ic}/K_{Ic} values. In the case of the weld metal in which the R_f/R_i is the same between the as-welded and heat-treated conditions, the TRIP effect of austenite and the softer martensitic matrix are the reasons for the higher ε_n and J_{Ic} values in the heat-treated material as discussed in the sections 5.3 and 5.4, respectively.

Table 5-1 Relation between R_f/R_i ratio and fracture properties (ε_n, J_{Ic}, and K_{Ic})

Material	R_f/R_i	ε_n	J_{Ic} (kJ/m^2)	Equivalent K_{Ic} (MPa√m)
CA6NM	2.97	0.9	299	256
410NiMo-AW	2.18	0.6	31	82
410NiMo-HT	2.18	0.68	59	114

5.2 Stress triaxiality-void growth relationship

According to equation (2.8), higher stress triaxiality S_T ratios during ductile rupture will result in smaller fracture strain for a given amount of void growth. However, the void growth amount is different between materials having different inclusion characteristics, and in addition, it was shown in the first paper (section 2.4) that the stress triaxiality ratio is related to the inclusion characteristics rather than the matrix properties. According to equation 2.8 and as confirmed by the experimental results obtained in the second chapter (see Table 2-8), higher S_T ratios are needed for higher amounts of void growth, which resulted in higher fracture strains. In the case of 415 steel, a very significant S_T ratio was predicted (about 50% higher than the measured one) for the estimated void growth from the inclusion characteristics. However, the material underwent a much lower void growth amount at a much lower S_T ratio due to the formation of the void sheets (Table 2-8). In fact, since the material experiences small deformations during void sheeting, the formation of the void sheets is defined as a way for the material to accommodate with high S_T ratios, decreasing the void growth amount (by about 55%). Nonetheless, despite the formation of void sheets in 415 steel, this material still experiences the highest S_T ratio to sustain the highest void growth amount compared to CA6NM steel and the weld metals.

Similar to 415 steel, the S_T ratio was also significantly decreased in CA6NM steel by decreasing the void growth amount, but a different micromechanical process was involved. In the case of CA6NM steel inclusions were much more numerous in the microstructure and small inclusions initiated the micro-voids at high stress triaxiality ratios to adapt with high constraints produced in the ligaments between micro-voids that have been already nucleated on large inclusions (R_{0L} as described in the section 2.3.1). Therefore, the S_T ratio decreased by 20% as a result of the nucleation of the second series of micro-void on the small inclusions.

In the case of the weld metals, fracture micromechanics can hardly be explained by S_T-void growth relationship since rupture occurred by an immediate coalescence without significant void growth under a relatively small S_T ratio. This is indeed because rupture is controlled by the nucleation of micro-voids rather than their growth due to the very numerous inclusions found in the microstructure.

5.3 TRIP effect

The formation of considerable amounts of reformed austenite during heat treatment contributes in improving the fracture strain and J_{Ic}-crack growth properties of CA6NM, 415, and 410NiMo-HT by TRIP effect. In fact, the major part of austenite is transformed into martensite in the elastic stage as shown by the peak in the n_i-ε curve of the heat-treated weld metal, presented in the second article (Figure 3-4). In addition, as the ε_n deformation was also improved by 13% after heat treatment it can be said that the TRIP is also active after necking, what is shown by Zhang and coworkers [14]. Note that all TRIP effect comparisons are based on the assumption that the stability of austenite, which mainly depends on austenite-promoting elements (especially Ni and Mo), is approximately similar among the heat-treated materials. This is in a good agreement with what happened in practice as these materials have similar Ni and Mo contents (Table 2-1).

In fact, a higher austenite content can be resulted in a larger martensite content produced by TRIP during stable crack growth, what can produce higher compressive stresses at the crack tip retarding the nucleation of micro-voids until higher deformations occur. The higher compressive stresses can also relax more strain energy ahead the J_{Ic}-crack, and hence higher crack driving forces (J) are required for crack growth. Furthermore, the compressive stresses retard the micro-void nucleation until higher strains are reached. Therefore, as CA6NM steel has about twice austenite content that 410NiMo-HT, it can be concluded that TRIP effect of austenite is one of the reasons why CA6NM steel has a much higher fracture toughness J_{Ic} and tearing modulus T values (Figure 4-6 and Table 4-6). However, it should be noted once again that in addition to the TRIP effect of austenite, the inclusion characteristics, especially their size and spacing, and the matrix mechanical properties are the other microstructural features taking effect on the ductile crack growth (see also sections 5.1 and 5.4).

5.4 Matrix effect

The yield strength/hardness of martensite as well as the strain hardening coefficient are among the most important matrix characteristics affecting the stable crack growth and the ductility. The matrix strength/hardness majorly affect the size of J_{Ic}-crack tip plastic zone. As shown in Figure 4-6, CA6NM steel presents a rising J-R curve, resulting in a higher resistance against stable crack growth at the onset and during J_{Ic}-crack extension compared to those in the weld metals. By contrast, the resistance against stable crack growth was not significantly increased in the weld metals, particularly in the case of the as-welded material for which the J values remained constant with J_{Ic}-crack growth. This is mainly because the crack tip plastic zone in CA6NM steel is much larger than that in the 410NiMo-AW and 410NiMo-HT. For CA6NM steel, the plastic zone also increases in size during J_{Ic}-crack growth, and that is why larger crack driving forces are required to grow the J_{Ic}-crack further. One of the reasons for this phenomenon can be the fact that the formation of plastic zone results in fracture energy dissipation at the crack tip [7]. Therefore, when the fracture energy is dissipated in a larger volume due to a larger plastic zone formation, higher fracture energies should be released to create two new crack surfaces (i.e., J_{Ic}-crack growth). In fact, the rising J-R curve of CA6NM steel shows that this material has elastic-plastic behavior when a small laboratory sample is tested. In this case, only the J_{Ic} value is size-independent and can be considered as the material property “fracture toughness J_{Ic}”, whereas the J-R curve is size-dependent and its shape will be changed if larger samples are tested.

In the case of the weld metals, as discussed in the second paper (chapter 3), the flat J-R curve obtained for the as-welded material shows linear-elastic behavior as constant J values were obtained even out of the 1.5 mm exclusion line (Figure 3-5), suggesting that the plastic zone remains constant in size. Therefore, in addition to the fracture toughness J_{Ic} value, the J-R curve is also size-independent and testing larger samples will not change the shape of the J-R curve. For the heat-treated material, the crack tip plastic zone increases in size with J_{Ic}-crack growth, and higher energy should be released (J values) to grow the J_{Ic}-crack further (Figure 3-5). Therefore, it can be said that unlike as-welded material, the heat-treated material shows elastic-plastic behavior under large-scale yielding conditions for the sample size used in this study. In this case, apart from the fracture toughness J_{Ic} value measured at the onset of stable crack growth, the J-R curve is size-dependent i.e., the dJ/da will decrease if thicker samples are tested.

The parameter that can be used to compare the size dependency of the J-R curves is the tearing modulus T. In fact, for elastic-plastic behavior using thicker samples decreases the slope of the J-R curve, and even a flat J-R curve can be obtained if thick enough sample is used. A larger T value means that the increase in the size of J_{Ic}-crack tip plastic zone is taking place in a higher speed i.e., the J-R curve rises with a higher slope (dJ/da). The 13 times higher T value in CA6NM steel compared to that in the 410NiMo-HT material (Table 4-6) shows that much higher fracture energy shall be released to maintain the J_{Ic}-crack growth since much higher portion of the fracture energy is stored as a lager crack tip plastic zone is formed during crack extension. Therefore, to develop a flat J-R curve (or perform a K_{Ic} test) in the case of CA6NM, much larger samples must be used compared to the case of 410NiMo-HT. For both these materials, using thicker samples decreases the dJ/da, and flatter J-R curves will be developed. On the other hand, the higher T value in the case of CA6NM steel also shows that the J_{Ic}-crack stability is much larger than that in the weld metals, and unstable crack propagation will not occur for this sample size. The very small T value in the as-welded material shows that once crack driving force reaches the J_{Ic} value, crack growth can be maintained since the plastic zone ahead of the crack will not be increased with J_{Ic} crack growth.

Since 410NiMo-AW showed a linear-elastic behavior, the fracture toughness of this material can be determined directly by K_{Ic} testing of a small laboratory sample. It means that the size of the crack tip plastic zone in this material is small enough compared to the sample dimensions, and crack propagation occurs suddenly under a constant crack driving force, and one-point fracture toughness value can be obtained without the need for developing a resistance curve. This plastic zone size (r_y) under LEFM can be estimated by Irwin's approach: $r_y=(1/3\pi)x(K_{Ic}/\sigma_y)^2$. Interestingly, the Irwin's approach predicts a linear-elastic behavior for the as-welded material using a 25.4 mm thick sample since it is 25 times thicker than the estimated plastic zone size (of about 1 mm), what was confirmed by the flat J-R curve of this material. This is based on the experimental results showing that flat fracture under plane strain conditions is dominant when samples thicker than 25 times of r_y are tested, and hence a size-independent fracture toughness is obtained [7]. In fact, this is based on the early findings on the fracture toughness K_{Ic} test in which the formation of shear lips at sample surfaces was resulted in an increase in the apparent fracture toughness [7]. This rule of thumb results in 525 mm and 62.5 mm thick samples for CA6NM and 410NiMo-HT materials, i.e., 21 times and 2.5 times thicker samples than those used in this thesis, respectively. Therefore, in order to determine fracture toughness of these materials using small laboratory samples, J_{Ic} tests should be performed, as were done in this thesis.

5.5 Cleavage vs. dimpled rupture

Cleavage rupture was only occurred during stable J_{Ic}-crack growth in the as-welded HAZ, resulting in a significant decrease of the fracture toughness, as presented in the third article (chapter 4). However, dimpled rupture of the remaining ligaments, which formed half the fracture surface, increased the fracture toughness to a value twice than that of the heat-treated weld metal (Table 4-6). Even after heat treatment, the fracture toughness of the HAZ reached slightly higher than that of the substrate, changing the fracture mode into a totally dimpled rupture. The fracture micromechanics are very similar between the heat-treated HAZ (Figure 4-8 (b)) and the CA6NM steel (Figure 4-8 (c)) in terms of initiation sites, dimple size, and coalescence of micro-voids, showing that a simple heat treatment can eliminate the negative effects of the high thermal cycles exposed to the substrate steel.

It is important to recall that the stable J_{Ic}-crack growth was terminated by unstable crack propagation into the weld metal in both as-welded and heat-treated HAZ due to the fact that the crack tip plastic zone is much smaller in the weld metal, and hence much lower crack driving forces are required for crack propagation. These unstable crack propagations occurred by dimpled rupture in which inclusion characteristics play the major role; hence, the very small inclusion spacing in the microstructure of the weld metal is the key parameter which resulted in an immediate crack propagation, causing a premature coalescence of the nucleated micro-voids without a significant void growth. Finally, it can be concluded that the weakest region in terms of stable/unstable crack growth in the welded joints of these materials is the weld metal, rather than the HAZ.

CONCLUSIONS

This thesis provides an important database for fracture behavior of the base metal, weld metal, and the HAZ of 13% Cr-4% Ni martensitic stainless steels during tension and J_{Ic} crack growth. Relationships among fracture behavior, inclusion characteristics (especially their size and spacing), austenite contents, and matrix properties were established. The effect of post-weld heat treatment on fracture behavior was also investigated. The main conclusions are summarized below:

- ✓ Different inclusion distributions in the microstructure result in different fracture micromechanics in ductile rupture;
- ✓ The size and spacing of inclusions are among the most important characteristics playing the major role in fracture micromechanics: the higher is the ratio of the half average inclusion spacing (R_f) to the inclusion radius (R_i), the higher is the void growth;
- ✓ The void growth amount can be estimated by $\ln(R_f/R_i)$;
- ✓ A higher amount of void growth results in a larger deformation during rupture;
- ✓ In the case in which inclusions are largely spaced, fracture micromechanical processes can be defined by void growth-S_T relationship and fracture strains can be estimated using the modified Rice and Tracey model;
- ✓ Void growth-S_T relationship can hardly explain fracture micromechanics when inclusions are very numerous in the microstructure (very small inclusion spacing) since rupture is controlled by nucleation of micro-voids, rather than their growth;
- ✓ Post-weld heat treatment is a very effective way to improve the ductility and crack growth resistance as it increases the austenite content and strain hardening of the martensitic matrix without scarifying the yield strength. The TRIP of austenite contributes in increasing the strain hardening as well as retarding micro-void nucleation;
- ✓ Both initiation fracture toughness J_{Ic} and tearing modulus of the weld metal were significantly improved after heat treatment by a factor of 2 and 75%, respectively;

- ✓ The heat treatment improved fracture toughness of the HAZ (by a factor of about 3) to a J_{Ic} value slightly higher than the substrate steel, transforming the fracture mode from a mix of cleavage and dimpled rupture into a totally dimpled rupture with the same fracture appearance of the substrate material;
- ✓ The J_{Ic}-crack growth in the HAZ was terminated by unstable crack propagation in the weld metal in both as-welded and heat-treated conditions as much lower crack driving forces were needed for crack growth in the weld metal itself. The key reason for this is the very low inclusion spacing in the weld metal, contributing in an immediate coalescence without a significant void growth.

RECOMMENDATIONS

As shown in this thesis, the inclusion characteristics, the strength/hardness of martensitic matrix, and the TRIP of austenite are among the major microstructural features contributing in crack growth resistance of these materials. The substrate (CA6NM steel) showed a rising J-R curve with a very high fracture toughness J_{Ic} and tearing modulus values; however, this is the crack growth resistance of the weld metal (even after heat treatment) that should be improved in order for enhancing the reliability and lifetime of the hydroelectric runners. To this purpose, the following research topics are recommended:

- The flux composition can be modified in order for producing lower amounts of inclusions in the microstructure of the resultant weld metal while protecting the weld pool properly from the air;
- The heat treatment can be optimized in terms of duration and temperature in order to obtain a more effective combination between the stability and content of austenite;
- The effect of different contents of austenite promoting elements, particularly Ni and Mn, on the content and mechanical stability of austenite can be investigated in order to find a good content/mechanical stability of reformed austenite;
- The effect of prior austenite grain size, as well as the shape of reformed austenite can also be examined.

LIST OF BIBLIOGRAPHICAL REFERENCES

[1] D. Carrouge, "Phase transformations in welded supermartensitic stainless steels," University of Cambridge, 2002.

[2] E. Folkhard and G. Rabensteiner, *Welding metallurgy of stainless steels*. Wien ; New York: Springer-Verlag, 1988, pp. x, 279 p.

[3] P. Bilmes, C. Llorente, and J. Pérez Ipina, "Toughness and Microstructure of 13Cr4NiMo High-Strength Steel Welds," *Journal of Materials Engineering and Performance,* vol. 9, pp. 609-615, 2000.

[4] C. Das, S. Albert, A. Bhaduri, G. Srinivasan, and V. Ramasubbu, "Effect of minor change in composition on toughness of weldmetal for repair of turbine blades made of martensitic stainless steel," *Science and Technology of Welding &# 38; Joining,* vol. 13, no. 2, pp. 159-166, 2008.

[5] D. Thibault, P. Bocher, M. Thomas, J. Lanteigne, P. Hovington, and P. Robichaud, "Reformed austenite transformation during fatigue crack propagation of 13%Cr–4%Ni stainless steel," *Mater. Sci. Eng., A,* vol. 528, no. 21, pp. 6519-6526, 2011.

[6] M. Paquin, D. Thibault, P. Bocher, J.-B. Lévesque, Y. Verreman, and K. Shinozaki, "Assessment of cold cracking tests for low transformation temperature martensitic stainless steel multipass welds," *Weld. World,* vol. 59, no. 4, pp. 521-532, 2015.

[7] T. L. Anderson, *Fracture mechanics: fundamentals and applications*. CRC press, 2005.

[8] D. Broek, *Elementary engineering fracture mechanics*, 4th rev. ed. Dordrecht, The Netherlands: Martinus Nijhoff, 1986, pp. xiv, 516 p.

[9] D. Thibault, "Contribution a l'étude du comportement en fatigue des aciers inoxydables 13%Cr-4%Ni : contraintes résiduelles de soudage et transformation sous contrainte de l'austénite de réversion," Ph. D Thesis École de téchnologie superieur, Montréal, 2010.

[10] M. Sabourin, D. Thibault, D.-A. Bouffard, and M. Lévesque, "New parameters influencing hydraulic runner lifetime," *25th IAHR Symposium on Hydraulic Machinery and Systems,* 2010. Timisoara, Romania

[11] D. Thibault, P. Bocher, and M. Thomas, "Residual stress and microstructure in welds of 13% Cr–4% Ni martensitic stainless steel," *J. Mater. Process. Technol.,* vol. 209, no. 4, pp. 2195-2202, 2009.

[12] P. Bilmes, M. Solari, and C. Llorente, "Characteristics and effects of austenite resulting from tempering of 13Cr-NiMo martensitic steel weld metals," *Mater. Charact.,* vol. 46, no. 4, pp. 285-296, 2001.

[13] S. Godin, "Effet d'un enrichissement en nickel sur la stabilité mécanique de l'austénite de réversion lorsque soumise à de la fatigue oligocyclique," École de technologie supérieure, 2014.

[14] S. Zhang, P. Wang, D. Li, and Y. Li, "In situ investigation on the deformation-induced phase transformation of metastable austenite in Fe–13% Cr–4% Ni martensitic stainless steel," *Materials Science and Engineering: A,* vol. 635, pp. 129-132, 2015/05/21/ 2015.

[15] S. Antolovich, "Alloy Design for Fatigue and Fracture," in *ASM Handbook.* vol. 19, ed: ASM International, 1996, pp. 27-41.

[16] W. M. Garrison Jr, "Controlling inclusion distributions to achieve high toughness in steels," *Iron Steel Technol.,* vol. 4, no. 6, pp. 132-139, 2007.

[17] P. Choudhary and W. M. Garrison Jr, "The Effect of Inclusion Type on the Toughness of 4340 Steel," *Mater. Manuf. Processes,* vol. 25, no. 1-3, pp. 180-184, 2010.

[18] J. L. Maloney and W. M. Garrison, "The effect of sulfide type on the fracture behavior of HY180 steel," *Acta materialia,* vol. 53, no. 2, pp. 533-551, 2005.

[19] S. Maropoulos, N. Ridley, J. Kechagias, and S. Karagiannis, "Fracture toughness evaluation of a H.S.L.A. steel," *Engineering Fracture Mechanics,* vol. 71, no. 12, pp. 1695-1704, 2004.

[20] D. Broek, "The role of inclusions in ductile fracture and fracture toughness," *Engineering Fracture Mechanics,* vol. 5, no. 1, pp. 55-66, 1973.

[21] S. Kou, *Welding metallurgy*. John Wiley and Sons, 2002.

[22] R. W. Messler Jr, *Principles of welding: processes, physics, chemistry, and metallurgy*. John Wiley & Sons, 2008.

[23] T. Kannan and N. Murugan, "Effect of flux cored arc welding process parameters on duplex stainless steel clad quality," *Journal of Materials Processing Technology,* vol. 176, no. 1, pp. 230-239, 2006.

[24] B. Senthilkumar and T. Kannan, "Effect of flux cored arc welding process parameters on bead geometry in super duplex stainless steel claddings," *Measurement,* vol. 62, pp. 127-136, 2015.

[25] B. Senthilkumar, T. Kannan, and R. Madesh, "Optimization of flux-cored arc welding process parameters by using genetic algorithm," *The International Journal of Advanced Manufacturing Technology,* pp. 1-7, 2014.

[26] R. W. Messler Jr, *Principles of welding: processes, physics, chemistry, and metallurgy*. John Wiley & Sons, 1999.

[27] J. C. Lippold and D. J. Kotecki, *Welding metallurgy and weldability of stainless steels*. Hoboken, N.J.: Wiley-Interscience, 2005, pp. xvi, 357 p.

[28] G. V. Voort, G. Lucas, and E. Manilova, "Metallography and microstructures of stainless steels and maraging steels," in *ASM Handbook.* vol. 9, ed, 2004, pp. 670-700.

[29] J. Aquino, C. Della Rovere, and S. Kuri, "Intergranular corrosion susceptibility in supermartensitic stainless steel weldments," *Corrosion Science,* vol. 51, no. 10, pp. 2316-2323, 2009.

[30] D. Kotecki, "Welding of stainless steels," in *ASM Handbook.* vol. 6, ed: ASM International, 1993, pp. 677-707.

[31] D. Thibault, P. Bocher, M. Thomas, M. Gharghouri, and M. Côté, "Residual stress characterization in low transformation temperature 13%Cr–4%Ni stainless steel weld by neutron diffraction and the contour method," *Mater. Sci. Eng., A,* vol. 527, no. 23, pp. 6205-6210, 2010/09/15/ 2010.

[32] M. P. Singh, K. S. Arora, R. Kumar, D. K. Shukla, and S. Siva Prasad, "Influence of heat input on microstructure and fracture toughness property in different zones of X80 pipeline steel weldments," *Fatigue Fract. Eng. Mater. Struct.,* vol. 44, no. 1, pp. 85-100, 2021.

[33] K. Xu, G.-y. Qiao, J.-s. Wang, S.-y. Zhang, and F.-r. Xiao, "Research on the fatigue properties of sub-heat-affected zones in X80 pipe," *Fatigue Fract. Eng. Mater. Struct.,* vol. 43, no. 12, pp. 2915-2927, 2020.

[34] M. Mohammadijoo, S. Kenny, L. Collins, H. Henein, and D. G. Ivey, "Characterization of HAZ of API X70 Microalloyed Steel Welded by Cold-Wire Tandem Submerged Arc Welding," *Metall. Mater. Trans. A,* vol. 48, no. 5, pp. 2247-2259, 2017/05/01 2017.

[35] S. Chen *et al.*, "Microstructure evolution and mechanical properties of simulated HAZ in a Ni-17Mo-7Cr superalloy: effects of the welding thermal cycles," *J. Mater. Sci.,* vol. 55, no. 27, pp. 13372-13388, 2020/09/01 2020.

[36] J. Wang, Y. F. Shen, W. Y. Xue, N. Jia, and R. D. K. Misra, "The significant impact of introducing nanosize precipitates and decreased effective grain size on retention of high toughness of simulated heat affected zone (HAZ)," *Mater. Sci. Eng., A,* vol. 803, p. 140484, 2021/01/28/ 2021.

[37] R. W. Hertzberg, *Deformation and fracture mechanics of engineering materials*, 4th ed. New York ; Toronto: Wiley, 1996, pp. xxiv, 786 p.

[38] M. A. Meyers and K. K. Chawla, *Mechanical behavior of materials*, 2nd ed. Cambridge: Cambridge University Press, 2009, p. 1 texte électronique (xxx p.).

[39] J. R. Rice, "A path independent integral and the approximate analysis of strain concentration by notches and cracks," *Journal of Applied Mechanics,* pp. 379-386, 1968.

[40] J. W. Hutchinson, "Singular behaviour at the end of a tensile crack in a hardening material," *Journal of the Mechanics and Physics of Solids,* vol. 16, no. 1, pp. 13-31, 1968/01/01/ 1968.

[41] J. R. Rice and G. F. Rosengren, "Plane strain deformation near a crack tip in a power-law hardening material," *Journal of the Mechanics and Physics of Solids,* vol. 16, no. 1, pp. 1-12, 1968/01/01/ 1968.

[42] J. D. L. Ja Begley, H. Corten, Ed. *The J Integral as a Fracture Criterion Fracture Toughness: Part II.* West Conshohocken, PA: ASTM International, 1972, pp. 1-23.

[43] *Standard Test Method for Measurement of Fracture Toughness*, 2019.

[44] N. E. Dowling, *Mechanical behavior of materials : engineering methods for deformation, fracture, and fatigue*, 4th ed. Boston ; Montréal: Pearson, 2013, pp. xvii, 936 p.

[45] B. L. Bramfitt, "Effects of composition, processing, and structure on properties of irons and steels," *Materials Park, OH: ASM International, 1997.,* pp. 357-382, 1997.

[46] R. E. Reed-Hill, *Physical metallurgy principles*, 2d ed. (University series in basic engineering). New York: Van Nostrand, 1972, pp. xiii, 920 p.

[47] T. Maki, "2 - Morphology and substructure of martensite in steels," in *Phase Transformations in Steels*, vol. 2, E. Pereloma and D. V. Edmonds, Eds.: Woodhead Publishing, 2012, pp. 34-58.

[48] H. Kitahara, R. Ueji, N. Tsuji, and Y. Minamino, "Crystallographic features of lath martensite in low-carbon steel," *Acta Materialia,* vol. 54, no. 5, pp. 1279-1288, 3// 2006.

[49] S. Morito, H. Yoshida, T. Maki, and X. Huang, "Effect of block size on the strength of lath martensite in low carbon steels," *Materials Science and Engineering: A,* vol. 438-440, pp. 237-240, 2006/11/25/ 2006.

[50] G. Krauss, "Martensite in steel: strength and structure," *Materials Science and Engineering: A,* vol. 273-275, pp. 40-57, 1999/12/15/ 1999.

[51] F. R. Stonesifer and R. W. Armstrong, "The Physical Metallurgy of fracture," in *Advances in Research on the Strength and Fracture of Materials*, vol. 2A, D. M. R. Taplin, Ed.: Pergamon Press, 1977, pp. 1-6.

[52] D. Webster, "Optimization of strength and toughness in two high-strength stainless steels," *Metallurgical Transactions,* vol. 2, no. 7, pp. 1857-1862, 1971.

[53] F. Huang and D. Gelles, "Influence of specimen size and microstructure on the fracture toughness of a martensitic stainless steel," *Engineering Fracture Mechanics,* vol. 19, no. 1, pp. 1-20, 1984.

[54] L. Schäfer, "Influence of delta ferrite and dendritic carbides on the impact and tensile properties of a martensitic chromium steel," *Journal of nuclear materials,* vol. 258–263, Part 2, no. 0, pp. 1336-1339, 1998.

[55] Y. Iwabuchi and I. Kobayashi, "A study of toughness degradation in CA6NM stainless steel," *Materials Science Forum,* vol. 654-656, pp. 2515-2518, 2010.

[56] H. Qiu, L. N. Wang, J. G. Qi, H. Zuo, and K. Hiraoka, "Enhancement of fracture toughness of high-strength Cr–Ni weld metals by strain-induced martensite transformation," *Materials Science and Engineering: A,* vol. 579, no. 0, pp. 71-76, 2013.

[57] P. Wang, N. Xiao, S. Lu, D. Li, and Y. Li, "Investigation of the mechanical stability of reversed austenite in 13%Cr–4%Ni martensitic stainless steel during the uniaxial tensile test," *Materials Science and Engineering: A,* vol. 586, pp. 292-300, 2013/12/01/ 2013.

[58] J. Shi, X. Sun, M. Wang, W. Hui, H. Dong, and W. Cao, "Enhanced work-hardening behavior and mechanical properties in ultrafine-grained steels with large-fractioned metastable austenite," *Scripta Materialia,* vol. 63, no. 8, pp. 815-818, 2010/10/01/ 2010.

[59] V. Kerlins and A. Phillips, "Modes of fracture," in *ASM Handbook.* vol. 12, ed: ASM International, 1987, pp. 12-71.

[60] F. Foroozmehr, Y. Verreman, J. Chen, D. Thibault, and P. Bocher, "Effect of inclusions on fracture behavior of cast and wrought 13% Cr-4% Ni martensitic stainless steels," *Eng. Fract. Mech.,* vol. 175, pp. 262-278, 4/15/ 2017.

[61] D. Broek, "A study on ductile fracture," TU Delft, Delft University of Technology, 1971.

[62] S. Lee, L. Majno, and R. Asaro, "Correlation of microstructure and fracture toughness in two 4340 steels," *Metallurgical Transactions A,* vol. 16, no. 9, pp. 1633-1648, 1985.

[63] D. Firrao and R. Roberti, "Interrelation among microstructure, crack-tip blunting, and ductile fracture toughness in mild steels," in *Advances in fracture research* vol. 2, ed. New Delhi, India, 1984, pp. 1311-1319.

[64] F. C. Campbell, *Fatigue and fracture: understanding the basics*. ASM International, 2012.

[65] W. M. Garrison and A. L. Wojcieszynski, "A discussion of the effect of inclusion volume fraction on the toughness of steel," *Mater. Sci. Eng., A,* vol. 464, no. 1, pp. 321-329, 2007/08/25/ 2007.

[66] T. Cox and J. R. Low, "An investigation of the plastic fracture of AISI 4340 and 18 Nickel-200 grade maraging steels," *Metall. Trans.,* vol. 5, no. 6, pp. 1457-1470, 1974.

[67] J. Gurland and J. Plateau, "The mechanism of ductile rupture of metals containing inclusions," *Trans. ASM,* vol. 56, pp. pp. 442-454, 1963.

[68] J. R. Rice and D. M. Tracey, "On the ductile enlargement of voids in triaxial stress fields∗," *Journal of the Mechanics and Physics of Solids,* vol. 17, no. 3, pp. 201-217, 1969.

[69] Y. Escatha and J. Devaux, "Numerical Study of Initiation, Stable Crack Growth, and Maximum Load, with a Ductile Fracture Criterion Based on the Growth of Holes," in *Numerical Study of Initiation, Stable Crack Growth, and Maximum Load, with a Ductile Fracture Criterion Based on the Growth of Holes*, 1979.

[70] Y. Huang, "Accurate dilatation rates for spherical voids in triaxial stress fields," *Journal of Applied Mechanics,* vol. 58, no. 4, pp. 1084-1086, 1991.

[71] D. François, A. Pineau, and A. Zaoui, *Mechanical Behaviour of Materials: Volume II: Fracture Mechanics and Damage*. Springer Science & Business Media, 2012.

[72] A. Trudel, M. Lévesque, and M. Brochu, "Microstructural effects on the fatigue crack growth resistance of a stainless steel CA6NM weld," *Engineering Fracture Mechanics,* vol. 115, no. Supplement C, pp. 60-72, 2014/01/01/ 2014.

[73] M. M. Amrei, H. Monajati, D. Thibault, Y. Verreman, L. Germain, and P. Bocher, "Microstructure characterization and hardness distribution of 13Cr4Ni multipass weld metal," *Mater. Charact.,* vol. 111, no. Supplement C, pp. 128-136, 2016/01/01/ 2016.

[74] A. Pineau, "Modeling ductile to brittle fracture transition in steels—micromechanical and physical challenges," *International Journal of Fracture,* journal article vol. 150, no. 1, pp. 129-156, March 01 2008.

[75] F. A. McClintock, "A criterion for ductile fracture by the growth of holes," 1968: ASME.

[76] G. E. Dieter, *Mechanical metallurgy*, 3rd ed. (McGraw-Hill series in materials science and engineering). New York: McGraw-Hill, 1986, pp. xxiii, 751 p.

[77] W. Brocks and W. Schmitt, "The second parameter in J-R curves: constraint or triaxiality?," in *Constraint Effects in Fracture Theory and Applicatons: Second Volume*: ASTM International, 1995.

[78] ASM-Handbook, "Quantitative Characterization and Representation of Global Microstructural Geometry," in *Metallography and Microstructures*, vol. 9: ASM-International, 2004, pp. 428-447.

[79] ASTM-International, "Standard Test Methods for Tension Testing of Metallic Materials," in *E8/E8M – 09*, ed. U.S.A.: ASTM, 2009.

[80] P. W. Bridgman, *Studies in large plastic flow and fracture*. McGraw-Hill New York, 1952.

[81] R. A. Young, "Introduction to the Rietveld method," in *The Rietveld method*, R. A. Young, Ed. UK: Oxford University Press, 1993, pp. 1-38.

[82] H. Rogers, "The tensile fracture of ductile metals," *AIME trans,* vol. 218, no. 3, pp. 498-506, 1960.

[83] A. A. Benzerga and J.-B. Leblond, "Ductile Fracture by Void Growth to Coalescence," in *Advances in Applied Mechanics*, vol. Volume 44, A. Hassan and G. Erik van der, Eds.: Elsevier, 2010, pp. 169-305.

[84] Y. W. Shi, "Critical void growth for ductile rupture of steel welds," *Engineering Fracture Mechanics,* vol. 34, no. 4, pp. 901-907, 1989/01/01/ 1989.

[85] A. L. Helbert, X. Feaugas, and M. Clavel, "The influence of stress trlaxiality on the damage mechanisms in an equiaxedα/β Ti-6AI-4V alloy," *Metallurgical and Materials Transactions A,* journal article vol. 27, no. 10, pp. 3043-3058, October 01 1996.

[86] S. Godin, J. Hamel-Akré, D. Thibault, A.-M. Serventi, and P. Bocher, "Ni and Mn enrichment effects on reformed austenite: thermodynamical and low cycle fatigue stability of 13%Cr–4%Ni and 13%Cr–6%Ni stainless steels," *SN Applied Sciences,* vol. 2, no. 3, p. 382, 2020/02/11 2020.

[87] M. M. Amrei, H. Monajati, D. Thibault, Y. Verreman, and P. Bocher, "Effects of various post-weld heat treatments on austenite and carbide formation in a 13Cr4Ni steel multipass weld," *Metallogr., Microstruct., Anal.,* vol. 5, no. 1, pp. 50-61, 2016.

[88] F. Foroozmehr and P. Bocher, "On the ductile rupture of 13% Cr-4% Ni martensitic stainless steels," *International Journal of Fracture,* vol. 224, no. 1, pp. 67-82, 2020.

[89] AWS, "Specification for Stainless Steel Flux Cored and Metal Cored Welding Electrodes and Rods," in *A5.22/A5.22M*, ed. U.S.A.: AWS, 2010.

[90] P. J. Jacques, F. Delannay, and J. Ladrière, "On the influence of interactions between phases on the mechanical stability of retained austenite in transformation-induced plasticity multiphase steels," *Metallurgical and Materials Transactions A,* vol. 32, no. 11, pp. 2759-2768, 2001/11/01 2001.

[91] H. Rastegari, A. Kermanpur, and A. Najafizadeh, "Effect of initial microstructure on the work hardening behavior of plain eutectoid steel," *Materials Science and Engineering: A,* vol. 632, pp. 103-109, 2015/04/24/ 2015.

[92] ASTM-International, "Standard test method for measurement of fracture toughness," in *E1820 - 11*, ed. U.S.A.: ASTM, 2011.

[93] J. Chen, Y. Verreman, and J. Lanteigne, "On fracture toughness JIC testing of martensitic stainless steels," in *ICF13*, 2013.

[94] J. Chen, Y. Verreman, F. Foroozmehr, and J. Lanteigne, "Fracture toughness of 13Cr4NiMo high-strength steels used in hydraulic turbine runners," in *Materials Science and Technology (MS&T) 2013*, Montreal, Quebec, Canada, 2013, vol. 1, pp. 702-711.

[95] D. S. Dugdale, "Yielding of steel sheets containing slits," *Journal of the Mechanics and Physics of Solids,* vol. 8, no. 2, pp. 100-104, 1960/05/01/ 1960.

[96] G. I. Barenblatt, "The Mathematical Theory of Equilibrium Cracks in Brittle Fracture," *Advances in Applied Mechanics,* vol. 7, no. C, pp. 55-129, 1962.

[97] D. A. Porter, K. E. Easterling, and M. Y. Sherif, *Phase transformations in metals and alloys*, 3rd ed. Boca Raton, FL: CRC Press, 2009, pp. xix, 500 p.

[98] R. Rana and S. B. Singh, *Automotive Steels: Design, Metallurgy, Processing and Applications* (Automotive Steels: Design, Metallurgy, Processing and Applications). Elsevier Inc., 2016, pp. 1-469.

[99] P. J. Jacques, Q. Furnemont, S. Godet, T. Pardoen, K. T. Conlon, and F. Delannay, "Micromechanical characterisation of TRIP-assisted multiphase steels by in situ neutron diffraction," *Philosophical Magazine,* vol. 86, no. 16, pp. 2371-92, 06/01 2006.

[100] K. H. J. Buschow, R. W. Cahn, M. C. Flemings, B. Ilschner, E. J. Kramer, and S. Mahajan, "Strengthening Mechanisms in Steels," in *Encyclopedia of Materials - Science and Technology, Volumes 1-11*: Elsevier, 2001.

[101] M. F. Ashby, "The deformation of plastically non-homogeneous materials," *The Philosophical Magazine: A Journal of Theoretical Experimental and Applied Physics,* vol. 21, no. 170, pp. 399-424, 1970/02/01 1970.

[102] C. B. Finfrock, A. J. Clarke, G. A. Thomas, and K. D. Clarke, "Austenite Stability and Strain Hardening in C-Mn-Si Quenching and Partitioning Steels," *Metallurgical and Materials Transactions A,* vol. 51, no. 5, pp. 2025-2034, 2020/05/01 2020.

[103] M. C. McGrath, D. C. Van Aken, N. I. Medvedeva, and J. E. Medvedeva, "Work Hardening Behavior in Steel with Multiple TRIP Mechanisms," *Metallurgical and Materials Transactions A,* vol. 44, no. 10, pp. 4634-4643, 2013/10/01 2013.

[104] C. Wang, H. Ding, M. Cai, and B. Rolfe, "Characterization of microstructures and tensile properties of TRIP-aided steels with different matrix microstructure," *Materials Science and Engineering: A,* vol. 610, pp. 65-75, 2014/07/29/ 2014.

[105] A. Trudel, M. Sabourin, M. Lévesque, and M. Brochu, "Fatigue crack growth in the heat affected zone of a hydraulic turbine runner weld," *Int. J. Fatigue,* vol. 66, no. Supplement C, pp. 39-46, 2014/09/01/ 2014.

[106] M. Mohammadijoo, S. Kenny, L. Collins, H. Henein, and D. G. Ivey, "Characterization of HAZ of API X70 Microalloyed Steel Welded by Cold-Wire Tandem Submerged Arc Welding," *Metallurgical and Materials Transactions A,* vol. 48, no. 5, pp. 2247-2259, 2017/05/01 2017.

[107] S. Chen *et al.*, "Microstructure evolution and mechanical properties of simulated HAZ in a Ni-17Mo-7Cr superalloy: effects of the welding thermal cycles," *Journal of Materials Science,* vol. 55, no. 27, pp. 13372-13388, 2020/09/01 2020.

[108] J. Wang, Y. F. Shen, W. Y. Xue, N. Jia, and R. D. K. Misra, "The significant impact of introducing nanosize precipitates and decreased effective grain size on retention of high toughness of simulated heat affected zone (HAZ)," *Materials Science and Engineering: A,* vol. 803, p. 140484, 2021/01/28/ 2021.

[109] M. P. Singh, K. S. Arora, R. Kumar, D. K. Shukla, and S. Siva Prasad, "Influence of heat input on microstructure and fracture toughness property in different zones of X80 pipeline steel weldments," *Fatigue & Fracture of Engineering Materials & Structures,* vol. 44, no. 1, pp. 85-100, 2021.

[110] K. Xu, G.-y. Qiao, J.-s. Wang, S.-y. Zhang, and F.-r. Xiao, "Research on the fatigue properties of sub-heat-affected zones in X80 pipe," *Fatigue & Fracture of Engineering Materials & Structures,* vol. 43, no. 12, pp. 2915-2927, 2020.

[111] W. J. P. Casas, S. L. Henke, and N. Novicki, "Fracture toughness of CA6NM alloy, quenched and tempered, and of its welded joint without PWHT," *Weld. Int.,* vol. 23, no. 3, pp. 166-172, 2009.

[112] F. Foroozmehr and P. Bocher, "Effect of low temperature intercritical heat-treatment on stable crack growth behavior in 13% Cr-4% Ni martensitic stainless steel multipass weldments," *Engineering Fracture Mechanics,* vol. 240, p. 107360, 2020/12/01/ 2020.

[113] K. Wallin and A. Laukkanen, "Improved crack growth corrections for J–R-curve testing," *Engineering Fracture Mechanics,* vol. 71, no. 11, pp. 1601-1614, 2004/07/01/ 2004.

[114] F. Foroozmehr and P. Bocher, "Effect of low temperature intercritical heat-treatment on stable crack growth behavior in 13% Cr-4% Ni martensitic stainless steel multipass weldments," *Eng. Fract. Mech.,* vol. 240, p. 107360, 2020/12/01/ 2020.